DISPERSION OF MULTI-WALLED CARBON NANOTUBES AND THEIR INCORPORATION INTO LIGNIN BASED FIBRES

by

Nai-Yu Teng

B.Sc., National Taiwan University, 2009

A THESIS SUBMITTED IN PARTIAL FULFILLMENT OF
THE REQUIREMENTS FOR THE DEGREE OF

MASTER OF SCIENCE

in

The Faculty of Graduate Studies

(Forestry)

THE UNIVERSITY OF BRITISH COLUMBIA

(Vancouver)

October 2012

Abstract

Intrinsic properties such as mechanical and electrical conduction make carbon nanotubes ideal for reinforcement of polymer materials. However, the inability to achieve uniform dispersion of carbon nanotubes has always been a major obstacle for possible composite applications. In this study, softwood Kraft lignin (SKL) and fractions obtained from solvent fractionation were used and characterized by thermal analysis, gel permeation chromatography (GPC), Fourier transform infrared spectroscopy (FT-IR), ^{1}H-NMR, and ^{13}C-NMR. Characterizations showed that F_4SKL, the solubilizable fraction with the highest molecular weight, exhibits association of the lignin molecules. It was observed that a small amount of SKL or F_4SKL respectively, facilitated the dispersion of multi-walled carbon nanotubes (MWNTs) in dimethylformamide (DMF) solutions. In addition, different lignin fractions showed different ability to disperse MWNTs. The various degrees of dispersion were easily observed through Raman spectroscopy. Based on the characterization results, it was inferred that π-interactions played an important role in the effective dispersal of MWNTs. Raman spectroscopy data also revealed that greater concentrations of F_4SKL could further disperse MWNTs, consistent with the hypothesis that the high performance of F_4SKL is attributable to its ability to form more π-interactions compared to other fractions.

It was observed that dispersion of MWNTs affects the performance of the electrospinning process. Solutions containing $F_{1\text{-}3}$SKL or F_4SKL in DMF were sonicated with MWNTs and spinning solutions were then prepared by adding the sufficient amount of the respective lignin and polyethylene oxide (PEO) for electrospinning. Solutions

prepared from $F_{1\text{-}3}$SKL suspensions contained aggregated MWNTs, which led to spraying and droplet accumulation during fibre formation. By contrast the MWNT suspensions prepared with F_4SKL were well dispersed and readily electrospun into fibres. It was observed that the higher the F_4SKL concentration in the MWNTs suspension the better the electrospinning stability. Adding 10 mg of F_4SKL enabled as much as 18.6 mg of MWNTs (or 6 wt% based on fibre weight) to be dispersed and electrospun into fibres. The resulting MWNT reinforced SKL fibres were then thermostabilized and carbonized and the resulting mechanical characterized. Unfortunately, the mechanical properties of the fibres did not improve with incorporation of MWNTs. However, the electrical conductivity increased from 2.2 to 2.8 S/cm when incorporating 6wt% MWNTs, indicating a potential utilization of these lignin based carbon fibres as conductive materials.

Table of contents

List of Tables

List of Figures

List of Abbreviations

ANOVA: analysis of variance

CNC: cellulose nanocrystals

CNT: carbon nanotubes

DMF: dimethylformamide

DMSO: dimethyl sulfoxide

DSC: differential scanning calorimetry

F_1SKL: methylene chloride soluble lignin fraction from SKL

F_2SKL: n-propanol soluble lignin fraction from F_1SKL-free SKL

F_3SKL: methanol soluble lignin fraction from F_2SKL-free SKL

$F_{1\text{-}3}$SKL: methanol soluble lignin fraction from SKL

F_4SKL: methylene chloride soluble lignin fraction from F_3SKL-free SKL

FT-IR: Fourier transform infrared spectroscopy

GPC: gel permeation chromatography

KL: Kraft lignin

MALLS: multi-angle laser light scattering

MMT: Montmorillonite

MWNT: multi-walled carbon nanotubes

NMR: nuclear magnetic resonance

PAN: polyacrylonitrile

PEO: poly(ethylene oxide)

SEM: scanning electron microscopy

SKL: softwood Kraft lignin

SWNT: single-walled carbon nanotube

TEM: transmission electron microscopy

TGA: thermogravimetric analysis

THF: tetrahydrofuran

XRD: X-ray diffraction

Acknowledgements

I would like to express my gratitude and appreciation for the many people that have guided me throughout my Master's study. First, I would like to thank my supervisor, Dr. John F. Kadla for giving me the opportunity to work in this outstanding group. I would also like to thank my committee members, Dr. Frank Ko and Dr. Greg Smith who have provided helpful advice and constructive criticism, as well as my non-departmental examiner, Dr. Savvas Hatzikiriakos. This project cannot be completed successfully without the guidance and assistance from both Dr. John F. Kadla and Dr. Frank Ko.

I am also very thankful to the Department of Wood Science faculty, staff, and fellow students for their friendship and advice, particularly members and former members in the Advanced Biomaterials Group: Ian Dallmeyer, Reza Korehei, Ana Filipa Xavier, Mirjam Mai, Sudip Chowdhury, Gernot Marten, Guang-Zheng Gao, Mijung Cho, Muzaffer Karaaslan, and Zhi-Ming Xu, as well as Ying-Jie Li, and Liting Lin from Dr. Frank Ko's group. I owe many thanks especially to Ian Dallmeyer who has always been helping me in my research.

I would like to dedicate this thesis work to my family who has continuously provided me with love, patience, and support.

1 Introduction

1.1 Lignin

1.1.1 Natural lignin

Lignin is a complex three-dimensional polymer that occurs predominantly in the xylem of many plants, making up 20 – 30% of the composition of wood (*1*). As a major component of the cell wall of tracheids, vessels and fibres, lignin contributes structural support to woody stems, confers protection against pathogens, and aids in the transport of water within the tree (*2*). The structure of lignins varies depending on the plant source, i.e. hardwoods, softwoods and grasses, location within the plant, i.e. earlywood, latewood, branches and stem, and the method of isolation. The degree of polymerization in native lignin is not known, since it is fragmented during extraction, but is believed to be very high.

There are three primary precursors or monolignols that make up lignin: *p*-coumaryl alcohol, coniferyl alcohol, and sinapyl alcohol (Figure 1.1); although other minor monomers also take part in lignification to a lesser degree. These primary monolignols are commonly referred to based on their aromatic ring structures; *p*-hydroxyphenyl (H), guaiacyl (G), and syringyl (S), respectively. Structurally, the three monolignols differ from each other in the amount and the position of the methoxyl groups. The simplest monolignol, *p*-coumaryl alcohol (H) does not contain any methoxyl units on the aromatic ring, while coniferyl alcohol (G) has only one methoxyl group at the C3 position, and sinapyl alcohol (S) has two methoxyl groups, located at the C3 and C5 positions. Softwoods have a lignin that consists almost entirely of G-units with small quantities of H-units, while hardwoods generally have a mixture of G and S structures (*3*).

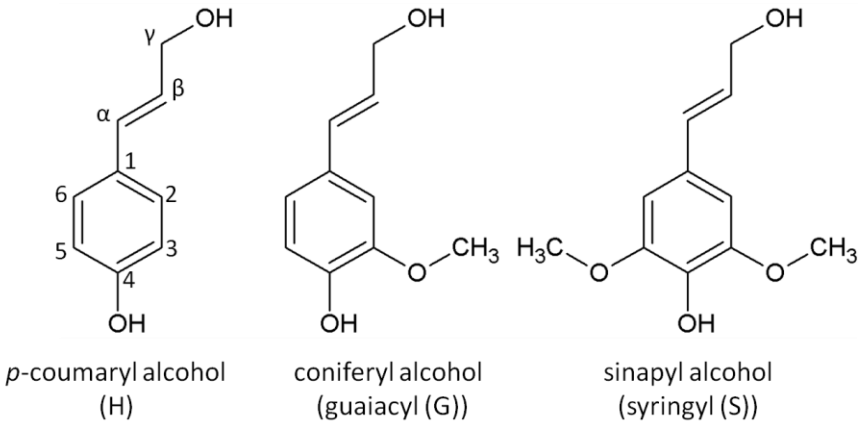

Figure 1.1 Precursors of lignin biosynthesis. Left: *p*-coumaryl alcohol. Middle: coniferyl alcohol. Right: sinapyl alcohol (*4*)

Lignification is a random dehydrogenation polymerization process (*5*) wherein phenoxy radicals are generated enzymatically followed by radical coupling of two mesomeric forms (Figure 1.2). The resulting dimeric structure then undergoes oxidation and radical formation followed by radical coupling with another phenoxy radical, repeating to form the lignin macromolecule. Based on this mechanism and the various mesomeric forms of the intermediate phenoxy radicals lignins have an irregular complex structure comprised of a variety of substructures and inter-unit linkages.

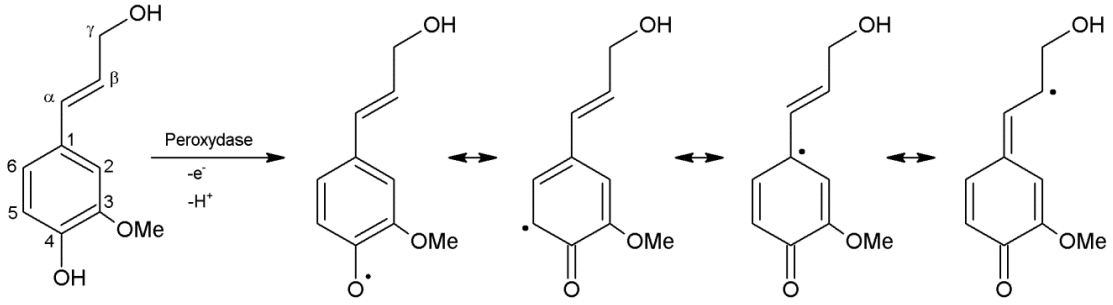

Figure 1.2 Radical mesomeric forms of coniferyl alcohol (*6*)

The most frequent inter-unit linkage formed in lignin is the β–O–4 linkage (Figure 1.3) which makes up 50% of the linkages in softwoods and 60% in hardwoods. As a result most technical industrial processes such as chemical pulping, and several analytical methods have focused on breaking these linkages as a means to separate lignin from the carbohydrate components (*5*).

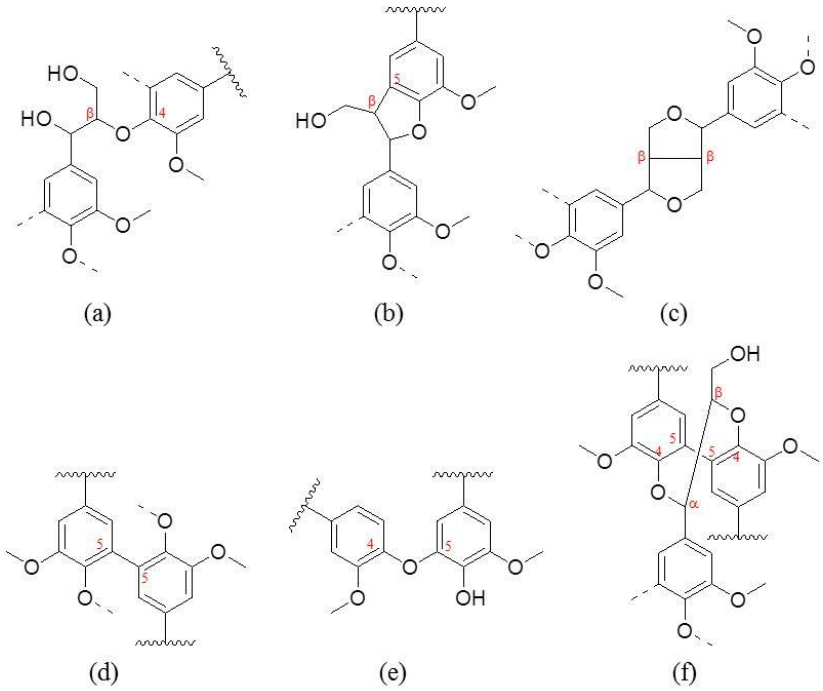

Figure 1.3 Common inter-unit linkages between phenylpropane units in lignin (*1*)

The second most abundant inter-unit linkage is the 5-5 linkage (20% in softwood and 9% in hardwoods) (Table 1.1) (*3*).Other linkages such as β–5, 4–O-5, and β–β are also formed with a lower quantity during lignification in softwood (Figure 1.3) (*3*).

Table 1.1 Proportions of different type of linkages in lignin (*3*)

Linkage type	Percent of the total linkage (%)	
	Softwood	Hardwood
β–O–4	50	60
5-5	20	9
β–5	10	6
4–O-5	6	7
β–β	3	3
Dibenzodioxocin (DBDO)	5-7	1-2

The amounts of linkages found in softwood and hardwood are different as well as the amount of functional groups. Hardwoods have higher methoxyl content of 139-188 per 100 C_6C_3 (*7*) unit while ~99 per 100 C_6C_3 unit for softwood lignin(*8*). Phenolic hydroxyl group content (14-18 per 100 C_6C_3 unit) is found lower that softwood lignin (19-26 per 100 C_6C_3 unit) (*9*). Figure 1.4 shows the model structure of native lignin found in softwood and hardwood.

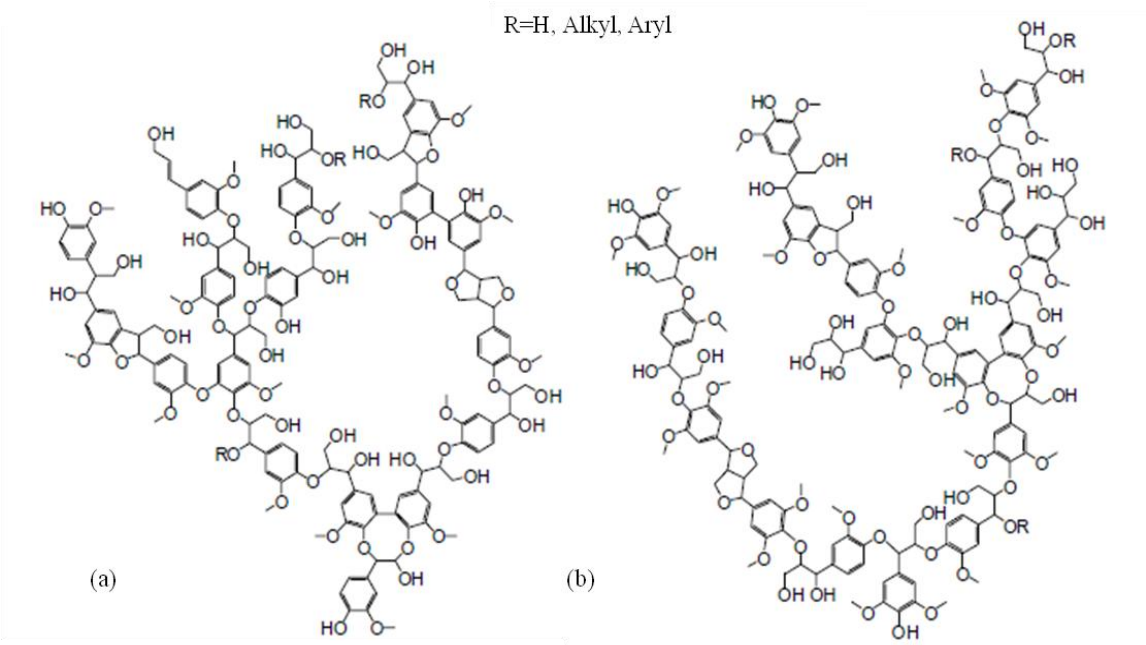

Figure 1.4 A representative structure of (a) softwood and (b) hardwood lignin (*4*)

1.1.2 Technical lignin

Lignin is typically obtained as a byproduct of pulp and papermaking, and its removal is a major processing step within the pulp and paper industry as it affects the commercial utilization of their products. The Kraft pulping process is the dominant process to achieve lignin removal (*10*). The objective of chemical pulping processes such as Kraft is to selectively remove the lignin to separate cellulosic fibres from one another to produce paper or related products. In conventional Kraft cooking, an aqueous solution of sodium hydroxide (NaOH) and sodium sulfide (Na_2S), also known as white liquor, reacts with wood chips in a large pressure vessel called a digester. The white liquor and the chips are heated to about 150-180 °C. During treatment, hydroxide and hydrosulfide anions react with lignin, causing the polymer to fragment into smaller water/alkali-soluble fragments. The lignin macromolecules undergo cleavage of ether

linkages, e.g. β–O–4 and α–O–4 holding the phenylpropane units together, accompanied with generation of free phenolic and aliphatic hydroxyl groups (Figure 1.5). The presence of these hydroxyl groups increases lignin hydrophilicity. As a result, the solubility of lignin in the cooking liquor is increased. After cooking, the black liquor, which includes degraded lignin (Kraft lignin), is separated from the pulp by washing and is concentrated to 65-80% solid content via evaporation. It is then combusted in a furnace to recover the cooking chemicals and to produce energy for the pulping process. After combustion, the black liquor can generate an inorganic smelt of sodium carbonate (Na_2CO_3) and sodium sulfide (Na_2S) which dissolves in water to form green liquor. The green liquor reacts with lime (CaO) to convert Na_2CO_3 to NaOH and regenerates back to the original white liquor (*11*).

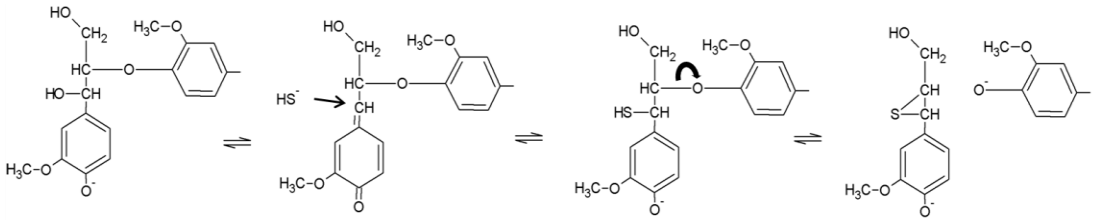

Figure 1.5 Scheme of cleavage on β–O–4 during Kraft pulping reaction

Other pulping processes are also carried out and different types of technical lignins can be obtained. They differ in molecular weight, quantity and nature of functional groups, solubility, thermal properties and thus in their field of application. Some examples are Lignosulfonates (Figure 1.6a), which can be obtained from sulfite pulping, a conventional chemical pulping process that utilizes sulfur dioxide (SO_2) at pH's ranging

from acidic to neutral to even alkaline and temperatures ranging from 120 to 180 °C. Organosolv pulping uses organic solvents, such as methanol and ethanol, acids and/or other catalysts with cooking temperatures between 120 to 250 °C to degrade and dissolve the lignin (*12*). The generated lignin is so-called organosolv lignin (Figure 1.6b).

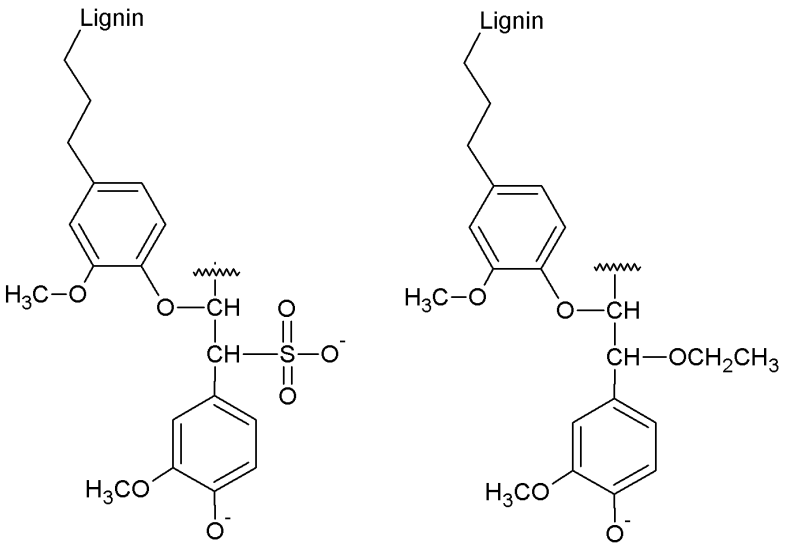

(a) Lignosulfonates (b) organosolv lignin

Figure 1.6 Representative structure of (a) Lignosulphonates and (b) organosolv lignin (*12*).

1.1.3 Common uses and applications

Up to now, technical lignin removed during pulp and papermaking still only serves for low priced applications, such as dispersants, resins, emulsion stabilizers, surfactants, and binders (*13*) or as an inefficient fuel source rather than higher value applications. In the predominant Kraft pulping process, (*14, 15*) only 1 – 2% of all Kraft lignin (KL)

generated worldwide is isolated and sold for value-added applications (*15*). There is therefore a motivation to develop more valuable applications of lignin instead of having its primary application be low quality fuel. Therefore, the application of lignin as a by-product and low-cost resource has been a topic of considerable interest (*14*). While dispersants are a well-known application of lignin (*15-17*), a relatively new application of lignin-based dispersants is preparing suspensions of carbon nanotubes (CNTs) (*18, 19*). Besides chemical utilization, another potential application is producing lignin based carbon fibres. Studies have already shown that carbon fibres can be produced successfully from technical lignin (*20-23*).

1.2 Carbon fibres

1.2.1 Properties and commercial applications

The combination of high strength, high modulus, and light weight makes carbon fibres one of the most important advanced materials (*24*). Other fibre properties, such as electrical conductivity and magnetic moment, also increase as a result of carbonization (*25, 26*). As such, carbon fibres are widely employed in areas where high strength and light weight are required. Carbon fibre reinforced composites are routinely used in sports equipment, construction, aircraft precursors and the automotive industry (*27*). Commercially, carbon fibres have two major types of precursors: pitch (petroleum or coal), and polyacrylonitrile (PAN) (*27-29*).

PAN is an excellent precursor for carbon fibres. PAN fibres have high strength and have been researched extensively; in fact PAN is the most widely used precursor for carbon fibre production (~90% of produced carbon fibre) (*30*). It is reported that global

consumption of carbon fibre was ~25,200 tons in 2006 and grew to 34,200 tons in 2010 (*31*). PAN based carbon fibres possess tensile strengths of 3–7 GPa and Young's moduli of 200–500 GPa, and dominate high performance aerospace and aviation markets (*28*). Pitch is the by-product of petroleum or coal tar which is a mixture of polycyclic aromatic compounds. Compared to PAN-based carbon fibres which exhibit higher tensile strength, pitch-based carbon fibres possess higher Young's moduli, as high as 900 GPa (*28*).

1.2.2 Lignin based carbon fibres

Petroleum based carbon fibres have some drawbacks, such as high and fluctuating prices due to the price and availability of oil and the finiteness of the petroleum precursors. Therefore, alternative carbon sources are highly sought after to produce carbon fibres. Lignin is a potential low cost, renewable, and non-petroleum based source for carbon fibre precursors. The first lignin-based carbon fibre was manufactured by Nippon Kayaku Co. in 1967 (*32*). The dry-spun fibres were made from lignosulfonate dissolved in an alkali, and Otani *et al*. (*33*) patented the lignin carbon fibre process in 1969. Comparing the mechanical properties of lignin carbon fibres produced from melt and dry spinning, it was found that dry-spinning of lignin fibres produced superior mechanical properties. This was attributable to longer solidification times, and better orientation of lignin molecules in dry-spinning. However, micro-voids caused by sodium impurities and a relative lack of orientation resulted in low modulus and low tensile strength carbon fibres (*34*). As a result, the use of these technical lignins as precursors for carbon fibres was abandoned.

Shortly thereafter Sudo *et al*. (*35, 36*) modified steam-exploded lignin by

hydrogenolysis and phenolation to improve processability and resulting mechanical properties of lignin carbon fibres. Organosolv lignin was also investigated and has been reported to produce carbon fibres by melt spinning. Organosolv lignins have fewer impurities than Kraft lignin (KL) and readily soften upon heating enabling thermal spinning. Moreover, this process was reported not to require thermostabilization because the high oxygen content of lignin facilitates molecular crosslinking. The 14±1 μm diameter organosolv lignin carbon fibres had tensile strengths and moduli of ~335 MPa and 39.1 GPa, respectively (*37, 38*). Again, this process did not proceed any further because of the non-commercial source of organsolv lignin and the poor mechanical properties as required for the high-performance carbon fibre market.

Kraft pulping is the most common and dominant commercial chemical pulping process. Therefore, technical lignin yielded from this process is currently more available/suitable than organsolv lignin as a carbon fibre precursor. Kadla *et al*. (*20*) produced carbon fibres from melt spinning a purified industrially produced hardwood kraft lignin. Purification to lower the salt content was crucial to prevent inclusions in the carbon fibres. To enhance melt spinning, a small amount (1-10 wt%) of poly (ethylene oxide) (PEO) was blended with the lignin. The resulting lignin fibres were then stabilized at temperatures up to 250 °C in air and carbonized at 1,000 °C in a nitrogen atmosphere. The carbon yield was between 40%–46% and carbon fibre diameter ranged from 31–63 μm. The tensile strength and the modulus were in the range of 400–550 MPa and 30–60 GPa, respectively. Kubo and Kadla (*23*) further produced carbon fibres from a blend of hardwood Kraft lignin and poly(ethylene terephthalate) (PET). The results showed that tensile strength and modulus were increased to 703 MPa and 94 GPa at a lignin/PET ratio

of 75/25. However, the carbon fibre yield decreased with the increasing PET. Most recently it has been reported that lignin based carbon fibre can be produced with strengths up to 1340 MPa and modulus of 103 GPa (*39*).

Despite these recent advances, the mechanical properties of lignin based carbon fibre still cannot compete with those made from PAN. Therefore, further improvement of fibre properties is needed as is the exploration of other possible applications for lignin derived carbon fibres. One approach to enhance mechanical properties is to reduce fibre diameters. Smaller diameters decrease the probability of defects and flaw sizes in fibres, and thereby increasing the mechanical properties (*40*). Although it is difficult to produce submicron fibres using wet and melt spinning techniques, electrospinning is well known to produce fibres with reduced fibre diameters. Not only do electrospun non-woven fabrics posses decreased fibre diameters, but they also have small pore sizes and high surface areas (*41, 42*). Softwood Kraft lignin (SKL) has been successfully electrospun into fibres (*43*).

1.3 Electrospinning

1.3.1 General description

Electrospinning refers to a fibre forming process wherein fibres are drawn by electrostatic forces. It is a simple method to produce nanoscale fibres from both synthetic (*44-46*) and natural (*47, 48*) polymers. Electrospinning was invented more than 100 years ago and was patented by Formhals in the 1930's (*49*). In 1969, it was published that the pedant polymer droplet formed at the tip of the needle developed into a cone shape when the surface tension was balanced by applied electrostatic force (*50*). This cone jet shape

was later referred to as the "Taylor Cone". In 1971, Baumgarten published that acrylic microfibres were produced by electrostatic spinning and fibres with diameters ranging from 500–1100 nm were obtained (*51*). In 1981, Larrondo and Manley demonstrated polyethylene and polypropylene fibres could be produced from polymer melts by electrospinning (*52*). However, despite the successes of producing nanofibres by electrospinning, it was not until the 1990's that they were really noticed (*53, 54*).

Besides significantly reducing the fibre diameter, electrospinning also increases the surface-to-volume ratios in nanofibres. Therefore, electrospun nanofibres have applications in many fields, such as composite reinforcement (*55*), filtration (*56*), tissue engineering (*57, 58*), electronics (*59, 60*), drug delivery, wound dressing (*61, 62*), and nanosensors (*63-65*). Electrospinning can use a wide variety of polymers (*66*) to produce highly porous nonwoven fabrics consisting of ultrafine fibres.

Electrospinning is a very simple process. In the lab, a syringe is filled with a polymer solution and the electrode is connected to the needle of the syringe and charged to high electric potential, as shown in Figure 1.7. The accumulation and mutual repulsion of charges on the surface of the droplet deform it into a conical shape, called a Taylor cone. Beyond a critical charge density, this cone is unstable and a jet of fluid is emitted from the tip of the cone (Figure 1.8). The transformation from the cone to the jet represents the initial stage of fibre formation (*67*).

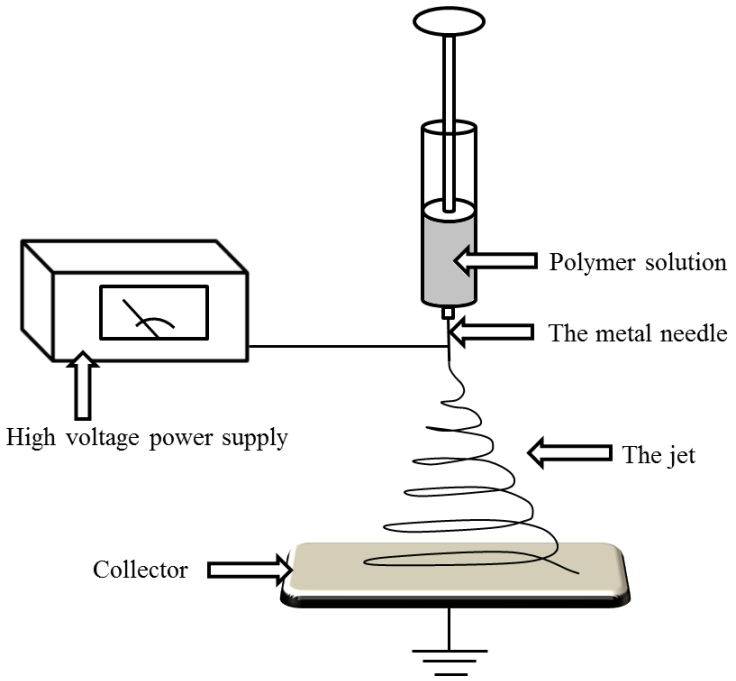

Figure 1.7 Scheme of the electrospinning process

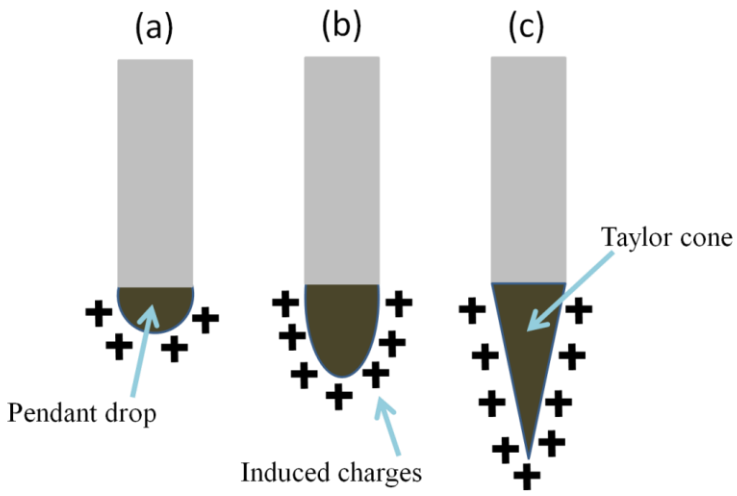

Figure 1.8 Scheme of formation of the Taylor cone. (a) Charges are induced to the surface of polymer and (b) accumulated at the surface of the pendant drop leading to elongation. (c) Charge repulsion overcomes the surface tension and deformation of the pendant drop occurs to form the Taylor cone due to charge-charge repulsion. (*68*)

The charged jet then undergoes a series of bending instabilities and travels to the ground which is the collector. The passage from the tip to the collector results in stretching and whipping of the jet, which is accompanied by the evaporation of solvents which dramatically reduces the diameter of the jet (*69*). As the solvent evaporates during the whipping process, the residue in the jet solidifies leading to the formation of fibres that accumulate on the collector (*70*). The key process to obtain submicron-scale fibres involves solution instability and the rapidly whipping jet (*71*).

Many processing parameters have been identified for influencing electrospinning and resulting properties of electrospun nanofibres. There are several parameters that can affect fibre diameter and morphology (*72*): the first group of parameters are the solution's properties such as polymer concentration, polymer molecular weight, solution viscosity, dielectric constant and solvent evaporation rate. The second class is based on processing factors such as spinning voltage, spinning distance, and the flow rate. The third is related to environmental factors such as humidity and temperature. Higher solution viscosity has been shown to result in a larger fibre diameter, which also indicates that a higher polymer concentration in solution will lead to larger fibre diameter (*73-75*). High viscosity polymer solutions require higher electric fields than lower viscosity solutions (*76*). However, increased viscosity can reduce formation of beads and defects and the average distance between beads on the fibres increases with increasing viscosity (*77*). In addition, the shape of beads changes from spherical to spindle-like as viscosity increases (*77*). With higher charge density on the surface of the solution jet during the electrospinning, it brings more electric charges to the jet such that higher elongation forces imposed on the jet results in smaller bead and fibre diameter (*66*). Also, increasing molecular weight can

reduce the number of beads and droplets (*45*) wherein a jet of low molecular weight fluid breaks up into small droplets, called electrospraying, i.e. solutions with dilute concentration and thus insufficient polymer chain overlap form droplets rather than continuous fibres (*45*). By contrast, polymer solutions with a sufficient amount and length of polymer chains will entangle, and continuous fibres will be formed during the electrospinning process (*78*).

Solvent properties can affect the spinning process as well. Solvents with a higher dielectric constant and dipole moment, will produce higher electrical susceptibility solutions when subjected to an electrostatic field, which helps increase the mass throughput from the spinneret (*79*). A large difference between the solubility parameter and the dielectric constant between the polymer and the solvent can also increase the size of beads in electrospinning (*79*). Likewise, changing the distance between the needle and collector affects the fibre morphology; beading occurring at distances too close to the collector where bead density decreases with increasing collector distance (*80*). Electrospinning polymer solutions using a volatile solvent requires less distance to form fibres since the solvent quickly evaporates during whipping (*76*).

The flow rate can also affect the electrospinning process. With a lower flow rate, fibres with smaller diameters are obtained (*70*); on the contrary, an excessive flow rate will produce fibres that have insufficient time to solidify before reaching the collector. When the delivery or feed rate of the polymer solution to the capillary tip exceeds the rate with which the solution is removed from the tip, an unstable jet results leading to the formation of fibres with large beads (*81*). Increasing the voltage will increase the rate

with which the solution is removed from the tip, but if increased to high the Taylor cone may not be maintained which will increase the instability of the jet and again lead to an increased formation of beads (*41*).

1.3.2 Mechanical and electrical conductive properties of electrospun fibres

Understanding the properties of electrospun fibres is critical for further applications. The most common way to determine mechanical properties such as tensile strength, Young's modulus, and tensile strain at the point of break of electrospun nanofibres is through tensile testing of nanofibre mats (*82*). Fibre mats are usually cut into rectangular or dumbbell shapes according to proper standard dimensions and are tested by a universal testing machine. Stretching-induced treatment could increase the strength and modulus of PAN fibres due to an improvement of molecular orientation (*83, 84*). The mechanical properties of electrospun fibres produced from a variety of other polymers are listed in Table 1.2.

Table 1.2 Tensile properties of electrospun fibre mats

Material	Fibre Diameter (nm)	Modulus (MPa)	Strength (MPa)	Reference
Silk from silk moth (bombyx mori)	200-400	600	15	(*85*)
Gelatin	100	117	2.9	(*86*)
Collagen-PEO	100-150	7	0.09	(*87*)
Peptide Polymer	450	1800	35	(*88*)
Polyurethane	100-500	3.7	10	(*89*)
PAN	100-300	1800	45.7	(*90*)

Electrical conductivity of electrospun carbon fibres has also drawn considerable attention with several studies having been published. Xuyen *et al*. (*91*) prepared electrospun polyamic acid (PAA) fibres and controlled fibre diameter by using triethyl amine as a catalyst. They found that the electrical conductivity of PAA carbon nanofibres increased with decreasing fibre diameter. They suggested that the number of cross junctions between nanofibres is key for improving carbon nanofibre conductivity. Wang *et al*. (*92*) investigated electrospun PAN carbon fibres and their results showed that a single PAN carbon fibre possessed a conductivity of around 4.9 S/cm. Panapoy *et al.* (*93*) prepared electrospun PAN nanofibres at different carbonization temperatures and results revealed that electrical conductivity increased with increasing carbonization temperature from 0.05 S/cm at 800^{o}C to 1.22 S/cm at 1000 ^{o}C. Similarly, Yang *et al.* (*94*) produced carbon nanofibres from polyimide carbonized at 1000 ^{o}C and obtained a conductivity of

2.5 S/cm.

1.4 Nanofillers

A common approach to enhance fibre mechanical and electrical conductive properties is through the addition of nanofillers (*46*). Interest in polymeric nanocomposites has been increasing in recent years due to their ability to significantly enhance material mechanical and electrical properties. Incorporation of nanofillers such as clay minerals, carbon nanotubes (CNTs) and inorganic nanoparticles into polymer matrices has been extensively investigated. Montmorillonite (MMT) has wide acceptability as a nanofiller because of its high surface area, and surface reactivity (*95*). It was reported that an improvement of mechanical properties was reached with a very small amount of MMT incorporated into nylon 6 matrices (*96*). In fact highly aligned MMT layers in nylon 6 crystallites in fibres could be obtained through electrospinning (*97*). The utilization of cellulose nanocrystals (CNCs) as reinforcing compounds has also been investigated intensely (*98*). These rodlike particles can be derived from a variety of renewable sources including wood, cotton, and ramie by acid hydrolysis (*99*). With high crystallinity, CNCs possess strong mechanical properties and serve as suitable nanofiller for reinforcing composites (*98, 99*). It has been reported that incorporating CNCs into electrospun fibres could increase fibre modulus (*100*). Carbon nanotubes (CNTs) are also commonly utilized in material composites to improve the properties (*82, 101*). A number of studies have reported the incorporation of CNTs into fibres leading improvements in mechanical properties and electrical conductivity (*46, 101-105*). It has been reported that the incorporation of CNTs with polyacrylonitrile (PAN) has improved the mechanical properties of the corresponding electrospun fibres (*46, 103*). However, due to their

natural tendency to form bundles through van der Waals forces, dispersion of CNTs is a major obstacle for further applications and utilizations (*106-108*).

1.4.1 Properties and applications

CNTs are cylindrical graphene sheets with the large aspect ratio (length/diameter which can be as large as 10^4-10^5) (*109*). CNTs are composed of sp^2 carbons and can take on a variety of structures as shown as in Figure 1.9. Depending on the structure the hexagons may spiral around the cylinder giving rise to "chirality" (shown in Figure 1.9), a twist that determines whether the CNT behaves like a metal (CNT adapts an "armchair" structure) or a semiconductor (*110*).

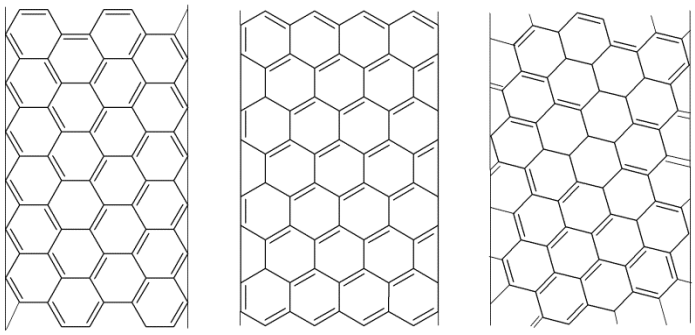

Figure 1.9 Single-walled CNTs of armchair (left), zig-zag type (middle), and helical type (right) (*111*).

CNTs are categorized as single-walled nanotubes (SWNTs) and multi-walled nanotubes (MWNTs). First discovery in 1991 by Iijima (*112*) they are now produced in large scale (*113*) by a variety of methods including high-pressure carbon monoxide (HiPCO) (*114*), chemical vapor decomposition (*115*) or carbon arc discharge (*116*)

methods.

It is now well known that CNTs possess outstanding mechanical properties (*117*) and electrical conductivity (*118*). The mechanical properties of CNTs have been studied by experimental and computational means. The tensile strength of CNTs is reported to be as high as 600 GPa, which is higher than current high-strength carbon fibres (*119*), and their density is approximately 1.3 g/cm^3 (*120*), which is lower than the density of commercial carbon fibres (1.78 g/cm^3). This means CNTs can result in volume or composite reduction at the same performance of other materials. This is important in aerospace and other high performance applications (*121*). CNTs are also one of the stiffest materials ever made. Compared to carbon fibres which typically have Young's moduli of up to 750 GPa, CNTs have moduli between 1 and 5 TPa (*122*). Their aspect ratios can be as high as 10,000 (*120*), which can be an advantage for imparting conductivity and strength to a composite system. It is apparent that the combination of size, structure and topology provides CNTs with excellent mechanical properties (*107*).

Because of their low energy dissipation, CNTs can carry tremendous current densities, higher than 100 MA/cm^2 for MWNTs, which may be compared to current densities of tens of kA/cm^2 for superconducting wires (*123*). Therefore, CNTs possess a notable electronic character (*124*).

1.4.2 Determination of the dispersion of CNTs by Raman spectroscopy

It has been reported that dispersion is one of the fundamental issues for mechanical reinforcement of composites and for an efficient load transfer to CNTs (*125*). Besides sonication, there are two general methods to disperse CNTs: non-covalent or covalent treatment to CNTs (*126*).

The chemical modification of CNTs involves the functionalization of the CNT surface through the introduction of polar groups (*127-129*), such as shown in Figure 1.10. Surface functionalization of CNTs can improve their chemical compatibility with the target medium (solvent or polymer solution/melt), in order to enhance wetting or adhesion characteristics and to reduce their tendency to agglomerate. A disadvantage of this strategy is the disruption of π-networks within CNTs, leading to a decrease in quality of mechanical and electrical properties (*130*).

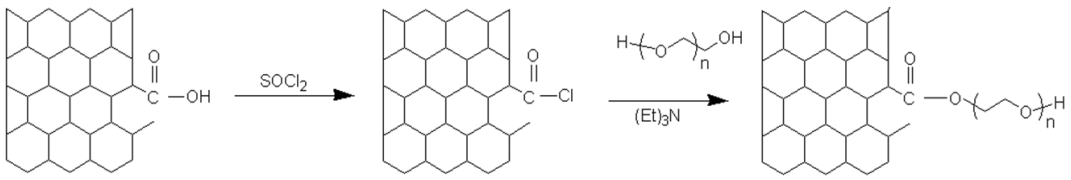

Figure 1.10 Synthesis of poly(ethylene glycol) (PEG)-grafted single-walled CNTs (*127*)

The mechanical method for dispersing CNTs includes ultrasonication and high shear mixing, which results in separating CNTs physically from each other. However, this approach can induce a considerable amount of defects, such as buckling and bending of CNTs leading to a more amorphous carbon structure (*131*). A second approach is the addition of polymers or surfactants capable of "wrapping" CNTs through non-covalent interactions (*18, 132-135*). However, high concentrations of polymers are usually needed to do so, creating difficulties for further processing and utilization (*136*).

Depending on the type of polymer or molecules added to the CNTs system, different mechanisms of interaction may exist. In non-oxidized CNTs it has been reported that the addition of aromatic molecules helps to disperse CNTs through π-interactions (*135, 137*). This approach does not form new covalent bonds or deteriorate the CNT's intrinsic properties, such as introducing sp^3-hybridized carbon through chemical modification, which could lead to decreased mechanical strength (*138*). In the case of surface-oxidized CNTs, π-interactions as well as the potential to interact via intermolecular hydrogen bonding in the presence of polar molecules may exist (*139, 140*).

Characterization of CNT dispersion is a critical issue. In general, suspensions are typically assessed or characterized by visual inspection, ultraviolet-visible absorption spectroscopy (UV-Vis) (*136, 141*), or Raman spectroscopy (*142-144*). Visual observations are not a quantitative way to determine CNT dispersion, particularly as CNTs have the disadvantage of forming visually black dispersions. However, they can provide a quick means by which to screen dispersion systems. In UV-Vis absorption spectroscopy, the absorption value at 500 nm is often chosen to quantify CNTs

dispersions. However, it is difficult to distinguish contributions from CNTs and other species, such as carbonaceous impurities or dispersing agents. Since visual inspection and UV-Vis adsorption are not suitable for the determination of CNT dispersion, Raman spectroscopy is the method of choice.

Raman spectroscopy is a spectroscopic technique used to study vibrational, rotational, and other low-frequency modes in a system and is a common method for characterization of CNTs (*142*), measuring impurity of CNTs in suspension or solid phase (*143*) and for the graphitization of carbon (*144*). Raman spectroscopy relies on the inelastic scattering of a laser source and is not very sensitive to the physical appearance of samples. Solid, liquid, and gas samples can be studied by Raman spectroscopy directly without other pre-treatments (*142*). During a scattering effect, an electron is excited by light and scattered by emitting or absorbing photons, then the electron relaxes to the valence state. The energy difference leads to the shifting of the photon's frequency; called the Raman effect, it is the frequency of the reemitted photons that is shifted up or down in comparison with the original monochromatic frequency.

In Raman spectra, graphite-like materials show two sharp peaks, the *G* band around 1580–1600 cm^{-1} and the *D* band around 1350 cm^{-1} (*145*). The G and D bands are only due to sp^2 sites, where the G band is based on the bond stretching of all pairs of sp^2 atoms in both rings and chains and the D band is due to the breathing modes of sp^2 atoms in rings (*146*). Figure 1.11 shows the eigenvector of the *G* band which involves the in-plane bond-stretching motion of pairs of carbon sp^2 atoms. This mode does not require the presence of six-fold rings, so it occurs at all sp^2 sites, not only those in rings. The *D* band

is a breathing mode and does not show up in perfectly ordered graphite, it only becomes active in the presence of disorder and defects. Its intensity is strongly related to the presence of six-fold aromatic rings (*145*).

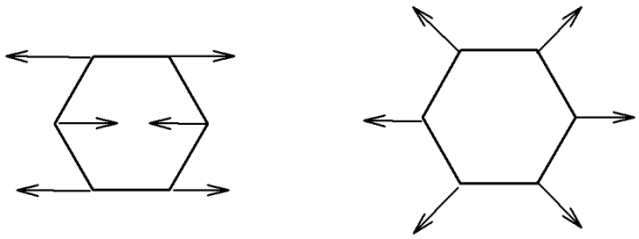

Figure 1.11 Carbon motions in the G (left) and D modes (right). (*145*)

Previous studies utilized Raman spectroscopy to characterize single-walled CNT dispersion in various solvents (*147-149*). These studies demonstrated that the G band intensity increased with sonication of the solutions, with more dispersion of CNTs (*147*). Therefore, Raman spectroscopy was chosen to characterize the D and G band of dispersion of multi-walled carbon nanotube (MWNT) suspensions in this study.

1.4.3 Incorporation of CNTs by electrospinning

CNTs can be utilized as electrically conducting components in polymer composites for commercial applications (*150*). However, CNTs are difficult to aligned when they are used as reinforcement in composites such that the resulting composite often does not exhibit the expected mechanical properties (*66*). Electrospinning has shown promise in improving the alignment of incorporated CNTs in polymer fibres (*151*). As such, several

researchers have tried to incorporate CNTs into polymer nanofibres produced through electrospinning (*46, 82, 101, 102*). It has been reported that the incorporation of CNTs into polyacrylonitrile (PAN) improved the mechanical properties of the electrospun fibres (*46, 103*). These results indicate that dispersed and aligned CNTs in the fibres make CNTs promising nanofillers for enhancing the mechanical properties of composite nanofibres. Ra *et al*. (*104*) also fabricated the electrospun PAN nanofibre fabrics embedded with MWNTs and it was found that the electrical conductivity was significantly enhanced with increasing MWNT concentration. At 10wt% MWNT concentration and carbonization at 1000°C, the conductivity reached 35 S/cm, about 10 times that of the pure PAN nanofibre fabric.

1.5 Goal of the project

Technical lignin has the potential to be utilized for high value products. The goal of this study is to produce carbon fibres from softwood Kraft lignin (SKL) with enhanced fibre properties. In order to improve fibre properties/performance, the addition of a nanofiller (MWNTs) and the reduction in fibre diameter was performed using electrospinning.

Although dispersion is an essential issue for composite reinforcement, it might be difficult to meet this requirement in the electrospinning of fibres with CNTs, due to the intrinsic properties of MWNTs, which tend to aggregate and form bundles. The first objective in this study is to disperse MWNTs in DMF by adding SKL and fractions thereof to the suspension and to investigate the correlation between lignin structure/properties and dispersion of MWNTs. It has been reported that KL can act as a

dispersant for MWNT; however, the mechanism of dispersion is still unclear. KL is a complex mixture of degraded native lignin fragments which vary greatly in molecular weight, types of inter-unit linkages, and functional groups. The structure of lignin naturally affects the predominant types of interactions contributing to dispersion of CNTs.

The second objective is to investigate the utility of Raman spectroscopy to characterize the dispersion of MWNTs in the presence of lignin. Aggregated and dispersed MWNTs suspensions likely have different R ratios (the ratio of intensity of G band and D band) in Raman spectra. Therefore we will investigate to see if there is a correlation between MWNT dispersion and measured R ratio.

The final objective is to investigate how the incorporation of MWCNTs affects fibre properties. Various concentrations of MWNTs were incorporated into electrospun fractionated SKL-based fibres. This included the characterization of as-spun, thermostabilized, and carbonized fibres in terms of morphology, graphitization, mechanical properties, and electrical conductivity.

1.6 Hypothesis

Numerous studies have utilized CNT incorporation to improve mechanical properties and electrical conductivity (*46, 101-105*) of composite fibres. Thus, adding CNTs into the SKL/PEO system may produce electrospun fibres with enhanced performance. Critical to improving mechanical properties and electrical conductivity of lignin based carbon fibres, is CNT dispersion and the efficient load transfer to the

reinforcing CNTs (*125*).

Kraft lignin (KL) is capable of acting as a dispersing agent for CNTs (*19*). KL is an aromatic polyol and may form π-interactions with CNTs and prevent or block van der Waals forces between CNTs that lead to CNT aggregation in solution. KL is known to aggregate into large supramolecular structures through the same π-π interactions as found in CNTs (*152*). Since KL consists of different fractions that can be extracted by organic solvents (*153*), each with varying molecular weights and functional group contents it can be expected that they may interact with CNTs differently. It is known that the various KL fractions have differing molecular mass as well as amounts of functional groups such as aliphatic and phenolic hydroxyl groups (*153*). The higher the molecular mass, the more aromatic nuclei present, the more potential to interact via π-π interactions. As well, it is known that aliphatic hydroxyl groups form stronger hydrogen bonds than phenolic hydroxyl groups (*154*). As a result, the fraction which contains higher aliphatic hydroxyl groups could form stronger interactions with the functionalized MWNTs used in this study and thus lead to enhanced dispersion. Therefore, it is hypothesized that fractionation of commercial SKL will produce SKL fractions with differing chemistries that will interact favorably with MWNTs leading to better dispersion and possibly to successful transference of mechanical and electrical conductive properties from the MWNTs to the fibres.

2 Materials and Methods

2.1 Materials

Softwood kraft lignin (Indulin-AT, SKL) was obtained from MeadWestvaco (Glen Allen, VA, USA) and repeatedly washed (10 x) with aqueous hydrochloric acid (HCl) at pH 2 to exchange sodium counterions and air dried at 105°C. Poly(ethylene oxide) (PEO) with an average molecular weight M_w of 1×10^6 g/mol, 4-nitrobenzaldehyde, pyridine, and chromium acetylacetonate were obtained from Sigma–Aldrich. *N*,*N*–Dimethylformamide (DMF), methylene chloride, n-propanol, methanol, acetic anhydride and potassium bromide (KBr) were obtained from Fisher Scientific (Ottawa, ON). Deuterated dimethyl sulfoxide ($DMSO_{d6}$) was obtained from Cambridge Isotope Laboratories, Inc. (MA, USA). Oxidized multi-walled carbon nanotubes (MWNTs) were obtained from CheapTubes.com (Brattleboro, VT, USA). PEO and all solvents were used as received.

2.2 Lignin fractionation

Lignin fractionation was performed as per a previously reported study (*153*). The commercial SKL was first acid-washed repeatedly 10 times by dispersing 500 g of SKL in 2 L of a dilute aqueous HCl solution (pH 2), mixed for 30-45 min and filtered. The final acid wash SKL was then dried in an oven at 105 ^oC to extract water. The acid-washed SKL was then fractionated by sequential solvent washing: first with methylene chloride, then n-propanol, followed by methanol, and finally methanol/methylene chloride (70/30, v/v). The methylene chloride-soluble fraction is referred to as F_1SKL, the n-propanol soluble fraction as F_2SKL, the methanol soluble fraction as F_3SKL, and the methanol/methylene chloride soluble fraction as F_4SKL. The

remaining insoluble fraction, termed F_5SKL, was not used in this study. One additional fraction was obtained by washing desalted SKL with methanol without performing the methylene chloride and n-propanol washing steps. Since it was observed that F_1SKL and F_2SKL were soluble in methanol we assumed that this fraction consisted of a mixture of F_1, F_2, and F_3 and will therefore be referred to as $F_{1\text{-}3}$SKL. Throughout each step of the fractionation procedure 1000 – 1500 mL of solvent were used per 150 g of lignin. The lignin suspensions were stirred at room temperature for 30 – 45 min and then filtered using Buchner funnel with cellulose filter paper (grade 1, Whatman). The dissolved lignin fraction was recovered by removing the solvent under reduced pressure, dried at room temperature overnight and stored in a vacuum desiccator. Each solvent treatment was performed twice and the residual lignin was dried and ground to a fine powder between treatment steps. After drying, each fractionated lignin was weighed to calculate yield; F_1SKL, F_2SKL, F_3SKL, and F_4SKL were 2.4%, 2.8%, 48.1% and 40.2% respectively. The yield of $F_{1\text{-}3}$SKL was 52.7%, approximately the same amount as the sum of the yields obtained for F_1SKL, F_2SKL, and F_3SKL.

2.3 Lignin characterization

Gel permeation chromatography (GPC) (Agilent 1100 Series GPC Analysis System, UV-Vis and RI detectors) connected to a multi-angle laser light scattering detector (MALLS) (Wyatt Dawn Heleos-II) equipped with fluorescence filters to eliminate signal contributions from lignin was carried out to determine the molecular weights of acetylated lignin fractions. Styrogel columns HR4, HR3 and HR1 (Waters Corp) were used at 35^{o}C with tetrahydrofuran (THF) as the eluting solvent (0.5 mL/min). Each fraction was dissolved in HPLC-grade THF at a concentration of 2 mg/ml and the

injection volume was 100 μL. The system was calibrated using polystyrene standards (Polysciences, Inc) and a lignin dn/dc of 0.159 (determined by preparing varied concentrations of lignin in THF) was used in the calculation of weight average molecular weights.

Acetylation was performed by dissolving 200 mg of SKL in 8 mL of pyridine/acetic anhydride (1:1, v/v) while stirring the reaction for 48 h at room temperature. The reaction solution was then added dropwise to 300 mL of stirred ice water. The precipitated lignin was then collected by filtration through a Nylon membrane (0.45 μm, 47 mm) and washed with diluted acid (HCl), saturated sodium bicarbonate, and ice-cold distilled water. Complete acetylation was confirmed by FT-IR spectroscopy and ^{1}H-NMR. The acetylated lignins were stored under vacuum at room temperature.

Fourier transform infrared spectroscopy (FT-IR) (Perkin Elmer Instruments – Spectrum One FT-IR Spectrometer) was employed to characterize the functional groups of the fractionated lignins. 1 mg of lignin powder sample was ground with 99 mg of Potassium Bromide (KBr), dried under vacuum to eliminate contribution by moisture and compressed into a pellet. Samples were analyzed using 32 scans collected over a scan range of 4000 – 600 cm^{-1} and a resolution of 4 cm^{-1}.

^{1}H and ^{13}C-NMR spectra were obtained using a Bruker Avance 300MHz spectrometer equipped with a BBO probe. In quantitative ^{1}H NMR, acetylated lignin (~ 5 mg) and the internal standard 4-nitrobenzaldehyde (~1 mg) were accurately weighed, mixed and dissolved in 500 μL of deuterated chloroform ($CDCl_3$) to enable quantitative

determination of hydroxyl group content. The NMR spectra were recorded at 25°C with a 90º pulse width and a 1.3 s acquisition time. A 7 s relaxation delay was used to ensure complete relaxation of the aldehyde protons. A total of 128 scans were collected. The phenolic OH and aliphatic OH content were obtained by integrating over the chemical shift range of $\delta_{2.6\text{-}2.2}$ ($\int_{2.6}^{2.2}$) or $\delta_{2.18\text{-}1.6}$ ($\int_{2.18}^{1.6}$), respectively, and normalizing the integral to that of the aldehyde proton ($\delta_{10.18}$) of the internal standard to 1. The amount of aliphatic and phenolic hydroxyl group content is obtained by the following equation:

$$\text{OH (mmol/g)} = \int_{2.6}^{2.2} \text{ or } \int_{2.18}^{1.6} \times \text{moles of standard} \div 3 \div \text{weight of SKL (g)} \qquad (1)$$

Quantitative ^{13}C NMR spectroscopy was performed using a lignin concentration of 15wt% in $DMSO_{d6}$ and with the addition of a relaxation agent chromium acetylacetonate (0.01 M) (*8*). Conditions for analysis were a 90º pulse width with a 0.9 s acquisition time and a 1.7 s relaxation delay. A total of 20,000 scans were collected.

Thermal analyses of fractionated SKL samples were performed by thermogravimetric analysis (TGA) and differential scanning calorimetery (DSC) using TA Instruments (New Castle, DE) Q500 and Q1000, respectively. The usual TGA procedure was to use 5 – 10 mg samples with a temperature program scanning from 40 to 600°C under nitrogen at a heating rate of 10°C/min. The decomposition temperature (T_d) of all samples was determined as the temperature at which 5% weight loss of the sample was measured and is based on 3 replicates. DSC analyses were performed under a nitrogen atmosphere in hermetically sealed aluminum pans using approximately 3 – 6 mg

samples. Samples were heated from –50 to 160°C at a heating rate of 10°C/min (first heating run), cooled to –50°C at 5°C/min (cooling run), and subjected to a second heating from –50 to 100, 130, 145, 180, 190, and 220°C (second heating run) for F_1SKL, F_2SKL, F_3SKL $F_{1\text{-}3}$SKL, SKL, and F_4SKL, respectively, at 10°C/min. Since the fractions differed in their T_d, the maximum temperature in the DSC experiments was varied according to the T_d of each fraction. The glass transition temperature (T_g) of the samples was recorded as the mid-point temperature of the heat capacity transition of the second heating run and reported as the average of 3 replicates.

2.4 Suspension preparation and characterization

MWNT suspensions were prepared by sonication of glass vials containing MWNT, DMF, and SKL or SKL fractions; 1 mg of lignin or lignin fraction and 3.1 mg MWNTs were added to 1 mL DMF in a 6 mL scintillation vial unless otherwise stated. The vial was placed into a cup with an immersed sonicating cone (Fisher Scientific, Sonicator Dismembrator, model 500) for 3 hours (sonicating program: 1 minute pulse on and 30 seconds pulse off) at a power level of 30 W (Figure 2.1). Dispersion of the MWNTs was characterized by optical microscopy (Olympus BX41) and Raman spectroscopy (RM1000, Renishaw, Gloucestershire U.K) equipped with a 785 nm laser using a 20x objective and a laser power density of approximately 1.0×10^4 W/cm^2. Samples were mounted on a cavity glass slide and measurements were taken at 5 different spots for each sample.

Figure 2.1 Sonicating cone with clamped sample

2.5 Solutions preparation and electrospinning

A mixture in F_4SKL:PEO weight ratio of 99:1 was used for all electrospinning experiments. Spinning dopes were prepared by weighing the appropriate amounts of F_4SKL and PEO (Table 2.1, sample A) into 7 mL scintillation vials followed by the addition of 1 mL of DMF to reach a final total polymer concentration of 25wt%. Vials of these solutions were then sealed and heated in an oil bath at 80°C. The solutions were vortexed every 30 min while heating for 2 hr. Solutions were cooled down for 10 min before electrospinning.

In the case of solutions containing MWNTs, various concentrations of F_4SKL and MWNTs (Table 2.1, sample B-E) were first dispersed in 1 mL DMF by sonicating (Fisher Scientific, Sonicator Dismembrator, model 500) for 3 hr (1 minute pulse on and 30 seconds pulse off) at a power level of 30 W. The MWNT/F_4SKL dispersions were then handled as per the other electrospinning samples, wherein the appropriate amount F_4SKL and PEO were added to obtain the 25wt% total polymer concentration, the vials sealed and heated in an oil bath as mentioned previously. A control sample without MWNT was also prepare the same way using the same sonication procedure.

Electrospinning was carried out in a vertical orientation using a 1 mL syringe fitted with a 21 G needle and the spinneret connected to a high voltage power supply (Glassman HighVoltage, Inc., High Bridge, NJ). The distance between the needle and the collector was 18 cm and a voltage of 15 kV was used (Figure 2.2). A controlled flow rate of 0.03 mL/min was maintained using a syringe pump (New Era Pump Systems, Inc. Wantagh, NY).

Table 2.1 Summary of MWNT concentrations in fibres and F_4SKL concentrations sonicated in suspensions with MWNTs

Sample	A	B	C	D	E
Amount of MWNTs in suspension	N/A	3.1 mg (1wt%)	12.4 mg (4wt%)	12.4 mg (4wt%)	18.6 mg (6wt%)
Amount of F_4SKL sonicated with MWNTs	N/A	1 mg	1 mg	100 mg	100 mg
Amount of F_4SKL added after sonication, before spinning	311 mg	307 mg	298 mg	199 mg	193 mg
Total amount of F_4SKL in spinning solution	311 mg (99wt%)	308 mg (98wt%)	299 mg (95wt%)	299 mg (95wt%)	293 mg (93wt%)
Amount of PEO added in solution after sonication	3.1 mg (1wt%)	3.1 mg	3.1 mg	3.1 mg	3.1 mg
Final conc. of polymer in solution	25% (314 mg)	25%	25%	25%	25%

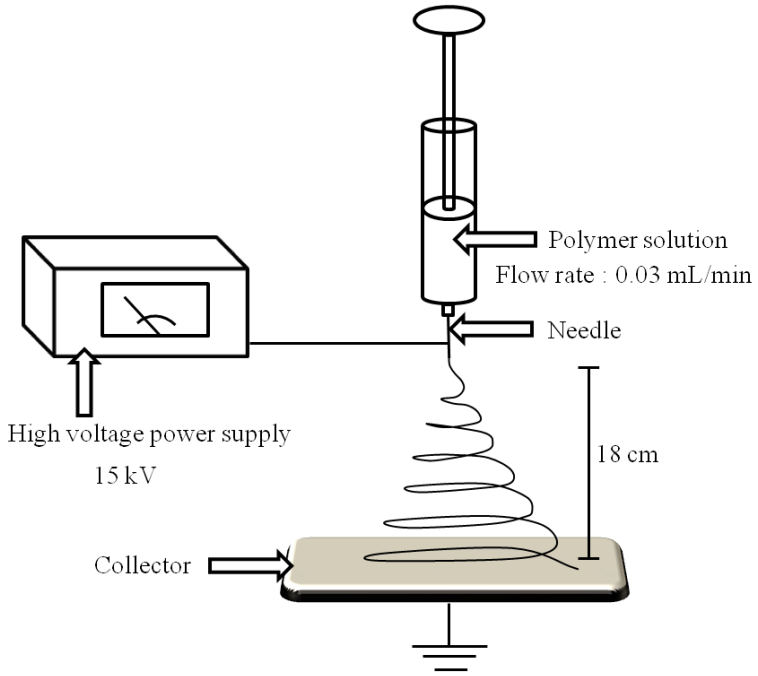

Figure 2.2 Scheme of electrospinning process and the parameters

2.6 Thermostabilization and carbonization

Thermostabilization was performed using a modified gas chromatography oven (Hewlett Packard HP 5890 Series II) (*20*). The four sides of the fibre mat (7.5 cm × 10.5 cm) were fixed onto a clamping system. The clamps were made of glass slides wrapped with Teflon™ tape to make an "L" shape. Both sides of the mat and clamps were covered with a glass petri dish (Figure 2.3a). The system was heated in air from room temperature at 5°C/min to 250°C and held for 1 hour. The thermostabilized fibre mats were cut into 0.5 cm × 5 cm pieces and then carbonized in a GSL1100X tube furnace (MTI corp.). Several pieces were stacked together and clamped at both ends using a steel frame-clamping rig (Figure 2.3b). The whole set was then placed into the tube furnace. To ensure there was no air in the system, the furnace was sealed and filled with nitrogen, then evacuated under vacuum (below 5 psi) and subsequently refilled with nitrogen.

Carbonization was achieved under a nitrogen atmosphere with the following heating program: 1) heat from 25°C to 250°C in 12 minutes, 2) isothermal at 250°C for 5 minutes, 3) heat to 1000°C at 10°C/min, and 4) isothermal at 1000°C for 1 h.

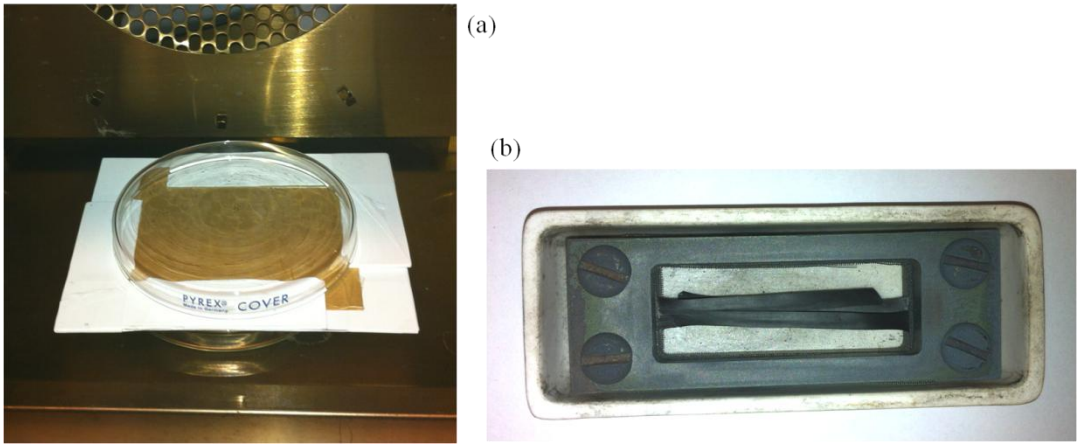

Figure 2.3 The clamping system for (a) thermostabilization and (b) carbonization process

2.7 Fibre characterization

Initial characterization of the fibre morphology was done through scanning electron microscopy (SEM; Hitachi S3000N) using gold coated samples and an accelerating voltage of 5 kV. Fibre diameter distributions were generated from the SEM images using ImageJ (U.S. National Institutes of Health) and average diameters (n=100) are reported. The comparison of fibre diameter was conducted by ANOVA at significance level of 0.05 to determine differences in fibre diameter due to the independent variables. Transmission electron microscopy (TEM; Hitachi H7600) operating at an accelerating voltage of 100 kV was employed to confirm the presence of MWNTs inside the as–spun,

thermostabilized, and carbonized fibres. Graphitization of carbon fibres and MWNTs was determined by X-ray diffraction (XRD, Bruker D8 Focus diffractometers equipped with a LynxEye detector) from 10° to 80° using a Cobalt source (λ= 1.79 Å). Carbon fibres were also characterized by Raman spectroscopy using a 20x objective and a laser power density of approximately 5.0×10^4 W/cm^2. The fibres required a lower laser intensity as compared to that used for the solutions (mentioned above) due to the lower spectral noise of the carbon fibres; for the solutions the laser power is set higher to obtain better resolution. Samples were loaded on a glass slide and three measurements were taken for each sample to confirm reproducibility. The Raman spectra were curve fit based on the model of Ferrari and Robertson (2000) (*145*).

Tensile strength testing was conducted with a Kato Tech KES-G1 Micro-Tensile Tester. Tensile testing samples were prepared by cutting the electrospun fabrics into strips of approximately 1 cm × 5 cm and mounting them onto a paper frame. The samples were then mounted into the micro-tensile tester and the tensile strength determined by pulling the bottom clamp down at a rate of 0.02 cm/s and recording the voltage as a function of time (20 replicates). The results were then processed as reported elsewhere (*82*). The time in seconds required to break the sample was recorded and converted to displacement (mm) by dividing with 0.02 cm/s (elongation rate) and then converted to strain by dividing with gauge length. The load on the samples was computed as gram force. Ultimate tensile strength, Young's modulus, % elongation at break and toughness were calculated. ANOVA was conducted to determine the differences of strength, moduli, elongation, and toughness between samples at significance level of 0.05.

For conductivity determination, carbonized fibres were cut into pieces of approximately 0.5 cm × 3.5 cm and each sample was fixed onto a glass slide by painting silver paint at two ends of sample (Figure 2.4). Fibre mat dimensions were determined by caliper measurements and the thickness was measured by optical microscopy. Samples were left in a fume hood overnight to let the silver paint dry.

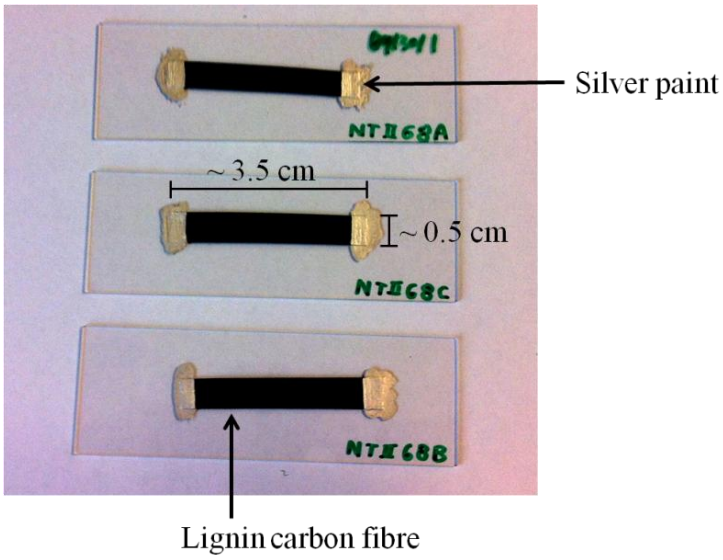

Figure 2.4 The specimens with silver paint at two ends for electrical conductivity measurements

Resistance was measured by a source meter (Keithley 2400) and the direct current conductivity, σ, was obtained by the equation:

$$\sigma = L / R \cdot t \cdot w \qquad (2)$$

where:

L is the length of the piece of material, R is the electrical resistance of the material, t is the thickness of the specimen, and w is the width of the specimen. The applied voltage ranged between –1 to +1 V at room temperature. Ten replicates were prepared and measured for each sample and the results were reported as an average.

3 Results and Discussion

3.1 Lignin characterization

Lignin is known to be a heterogeneous macromolecule, with varying lignin structure dependent on wood species (*5*), process of isolation (*10*) and fractionation (*153*). Therefore, SKL and other fractions (F_1SKL, F_2SKL, F_3SKL, $F_{1\text{-}3}$SKL, and F_4SKL) were characterized by GPC-MALLS, ^{1}H-NMR, ^{13}C-NMR TGA, and DSC.

3.1.1 GPC

Molecular weight measurements of acetylated lignin fractions were performed by GPC-MALLS. The measured molecular weights of lignin fractions are listed in Table 3.1. F_1SKL showed the smallest weight average molecular weight (Mw) and number average molecular weight (M_N) among the fractions at ~3,500 and ~1,600. F_2SKL, F_3SKL, and $F_{1\text{-}3}$SKL exhibited similar Mw at between 6,500-7,000 but distinctly different M_N's at 3,800-4,000, 2,600-2,900 and 3,000-3,200, respectively. F_4SKL exhibited both the highest Mw and M_N as well as PDI (M_W/ M_N) among the fractions. Interestingly the F_4SKL had M_W and M_N values significantly higher than that of the original SKL. This could be due to the fact that SKL is the mixture of all of the fractions F_1SKL, F_2SKL, F_3SKL, and F_4SKL (which is ~40% of the SKL). It may also be due to the fact that in the presences of the lower molecular weight fractions, F_4SKL does not associate to the same extent as when isolated and analyzed alone.

Table 3.1 Molecular weights from GPC with MALLS (fractions are acetylated) (n=2)

Fractions	M_W	M_N	M_W/ M_N
SKL	23,000 – 25,000	6,100 – 6,500	3.8
F_1SKL	3,200 – 3,700	1,400 – 1,800	2.2
F_2SKL	6,600 – 6,800	3,800 – 4,000	1.7
F_3SKL	6,600 – 7,000	2,600 – 2,900	2.5
F_{1-3}SKL	6,500 – 7,000	3,000 – 3,200	2.2
F_4SKL	34,000 – 36,000	8,000 – 10,000	3.9

The GPC-MALLS profiles obtained from the SKL and the various SKL fractions are shown in Figure 3.1, along with the trend in Molar mass vs elution volume. As expected the molecular mass distributions of F_1SKL, F_2SKL and F_3SKL overlapped within the range of F_{1-3}SKL. The elution profiles show relatively low molar masses with monomodal distributions. Moreover, those of the F_1SKL, F_2SKL and F_3SKL are well represented by F_{1-3}SKL. By contrast F_4SKL exhibited a multimodal distribution covering a very broad molar mass range. Although quite similar to that observed for the unfractionated SKL, the F_4SKL fraction has significantly more high molar mass material, shoulder at ~18.5 mL elution volume / $>10^5$ molar mass. Multimodal GPC distribution profiles with relatively large molecular masses have been widely reported for lignins; higher mass peaks arising from associated lignin macromolecules (*152, 155-157*). The GPC-MALLS results clearly show that there is a difference in the propensity to associate between the various fractions; F_1SKL, F_2SKL, F_3SKL and F_{1-3}SKL do not appear to form

any such supramolecular complexes, while F_4SKL does. Therefore in this regard $F_{1\text{-}3}$SKL appears to be a good representative sample for these lower molar mass fractions.

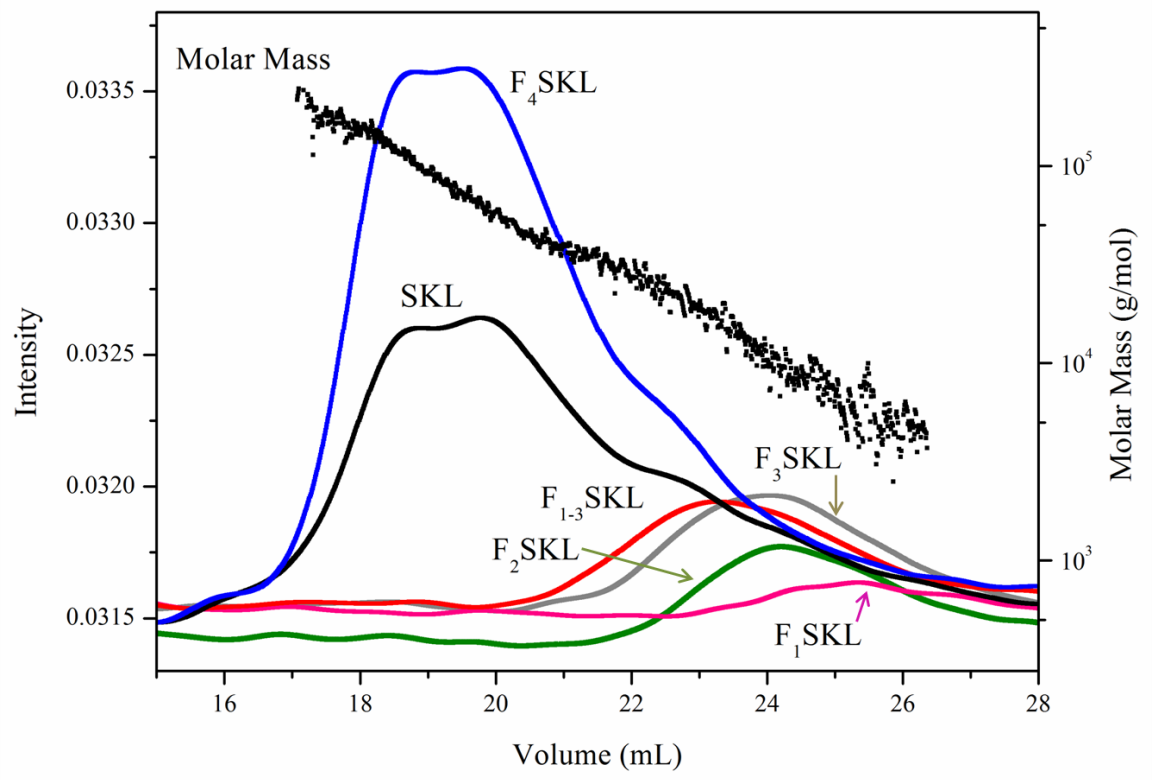

Figure 3.1 Molecular weights of acetylated SKL, F_1SKL, F_2SKL, F_3SKL, $F_{1\text{-}3}$SKL, and F_4SKL measured by MALLS

The addition of salts such as lithium chloride have been shown to eliminate lignin association, resulting in monomodal molecular weight distribution profiles being obtained (*158*). Moreover, studies using acetylated lignins to disrupt intermolecular hydrogen-bonding showed no affect on the multimodal distribution, indicating that hydrogen bonding was not the major driving force for macromolecular association (*159*). In fact, it has been proposed that the formation of such complexes arises from π–π

interactions between aromatic nuclei within lignin (*158*). Recently, Deng *et al.* (*157*) adjusted the aggregation between lignin molecules through the addition of Iodine and the formation of lignin-iodine complexes; electrostatic repulsions reduced the noncovalent orbital interactions between aromatic rings.

3.1.2 FT-IR

FT-IR analysis of non-acetylated SKL samples were measure in KBr over the range of 4000-600 cm^{-1} and are shown in Figure 3.2. FT-IR spectra of lignin samples were normalized at 1512 cm^{-1}, which represents the skeletal vibration of an aromatic ring. Enlarged ranges between 1800 – 1550 cm^{-1} and 1550 – 900 cm^{-1} are shown in Figure 3.3. These two regions represent bands associated with carbonyl stretching, aromatic C-C vibration, and C-H vibration and deformation.

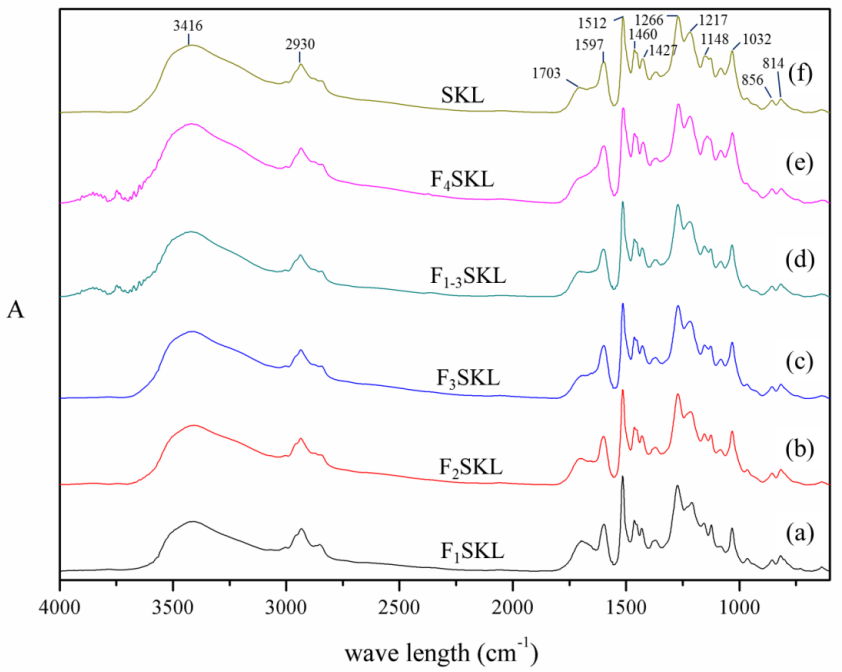

Figure 3.2 FT-IR spectra (4000 – 600 cm^{-1}) of (a) F_1SKL, (b) F_2SKL, (c) F_3SKL, (d) F_{1-3}SKL, (e) F_4SKL and (f) SKL

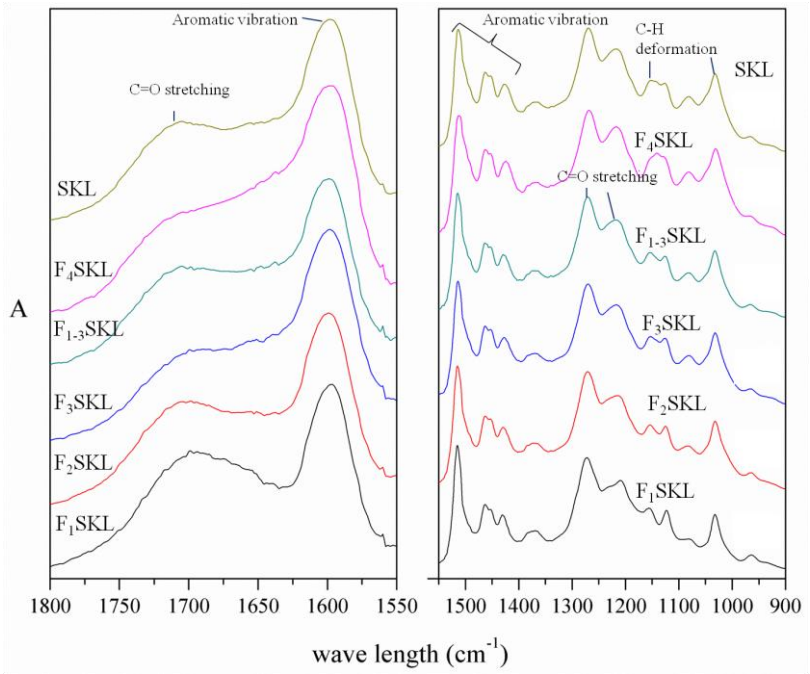

Figure 3.3 FT-IR spectra ranging from 1800 to 1550 cm^{-1} (left) and from 1550 to 900 cm^{-1} (right) of (a) F_1SKL, (b) F_2SKL, (c) F_3SKL, (d) F_{1-3}SKL, (e) F_4SKL and (f) SKL

Peak assignment of F_1SKL, F_2SKL, F_3SKL, $F_{1\text{-}3}$SKL, F_4SKL, and SKL is based on Boeriu *et al.* (*160*) and listed in Table 3.2.

Table 3.2 Peak assignment in FT-IR of Kraft lignin (*160*)

Wave length (cm^{-1})	Functional group
3460-3410	-OH
2930, 2843	-CH stretching
1703	unconjugated C=O stretching
1600, 1512, 1460, 1427	Aromatic vibration
1266	Guaiacyl ring and C=O stretch
1217	C-C, C-O, C=O stretching
1148	C-H deformation
1032	C-H vibration associated with C-O, C-C, and C-OH
854, 817	C-H vibration

F_1SKL exhibited a relatively higher intensity of carbonyl groups than the other fractions, which appeared to decrease with increasing fractionation number; the relative intensities being 0.31 (F_1SKL) > 0.28 (F_2SKL) > 0.24 (F_3SKL) and (F_4SKL). The peak between 1150 – 1100 cm^{-1} corresponding to deformations of C-H bonds in guaiacyl rings are slightly different between SKL fractions and may indicate a more condensed and complex aromatic substitution pattern in the F_4SKL. However, the characteristics of the aromatic ring vibrations (the region between 1625 – 1400 cm^{-1}), C=O/C-C/C-O stretching (the region between 1400 – 1200 cm^{-1}), and aromatic C-H deformation vibrations (the region between 1050 – 800 cm^{-1}) appear quite similar between fractions.

Overall, with the exceptions noted above, FTIR analysis of the various fractions appears to indicate that the functional groups do not exhibit large differences or shifting between fractions.

3.1.3 ^{1}H-NMR

Based on FT-IR, it was difficult to quantify the functional groups of each fraction. Therefore, a more detailed comparison was conducted using NMR. The ^{1}H-NMR spectrum of SKL is shown in Figure 3.4. The regions between 2.6-2.2 ppm and 2.18-1.6 ppm correspond to the acetyl methyl groups on the phenolic and aliphatic hydroxyl groups (OH), respectively.

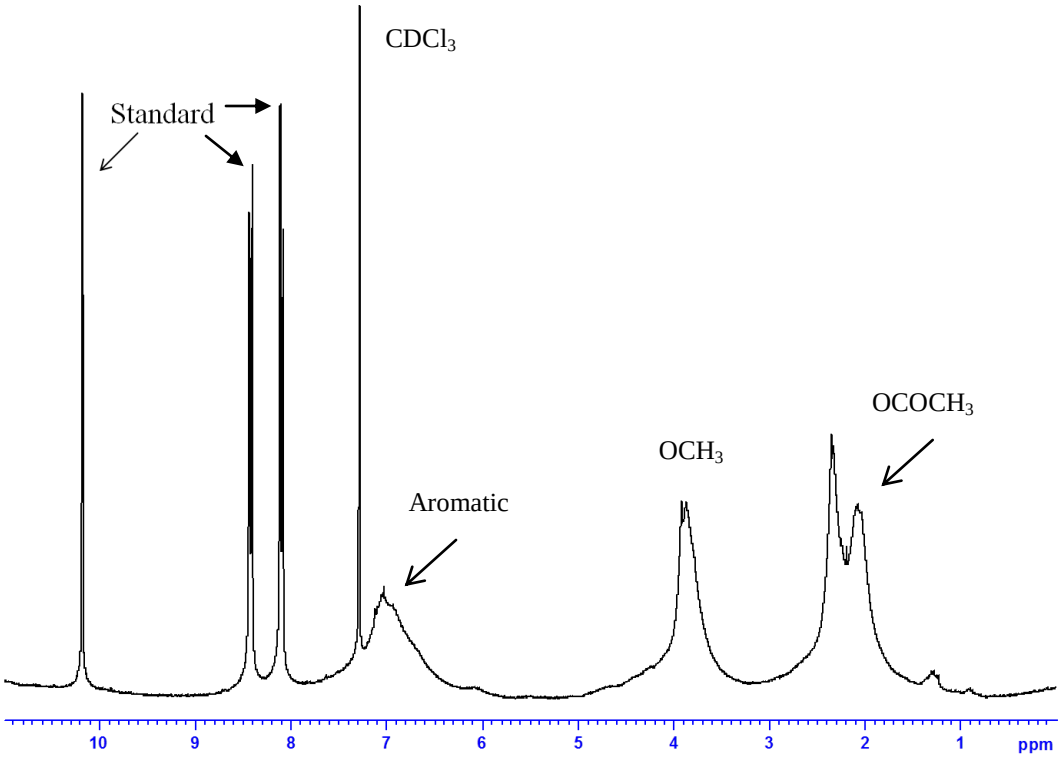

Figure 3.4 ^{1}H-NMR spectrum of acetylated SKL with internal standard (4-nitrobenzaldehyde) in $CDCl_3$.

The amount of phenolic and aliphatic hydroxyl groups in each of the SKL fractions determined from ^{1}H-NMR is listed in Table 3.3. In general the lower molecular mass fractions, F_1SKL, F_3SKL, and $F_{1\text{-}3}$SKL in particular contained higher total OH contents (8.36, 7.22, and 8.27 mmol/g, respectively) than F_4SKL (7.16 mmol/g). As well they (F_1SKL, F_2SKL, F_3SKL, and $F_{1\text{-}3}$SKL) had more phenolic hydroxyl groups and less aliphatic hydroxyl groups than the F_4SKL fraction; F_1SKL, F_2SKL, and F_3SKL contained ~3 mmol/g of aliphatic hydroxyl groups as compared to ~4.3 mmol/g for the F_4SKL and ~3.7-5 mmol/g versus 2.8 mmol/g phenolic hydroxyl groups.

Table 3.3 Phenolic and aliphatic hydroxyl groups contents of lignin fractions based on ^{1}H-NMR of acetylated samples

Sample	Phenolic OH (mmol/g)	Aliphatic OH (mmol/g)	Total OH (mmol/g)
SKL	3.75 ± 0.23	3.70 ± 0.12	7.45
F_1SKL	4.98 ± 0.65	3.38 ± 0.31	8.36
F_2SKL	3.77 ± 0.08	3.00 ± 0.15	6.77
F_3SKL	4.33 ± 0.50	2.89 ± 0.39	7.22
$F_{1\text{-}3}$SKL	4.46 ± 0.44	3.81 ± 0.23	8.27
F_4SKL	2.82 ± 0.15	4.34 ± 0.35	7.16

3.1.4 ^{13}C-NMR

Further structural information was obtained through quantitative ^{13}C-NMR (*150*). However, due to the fact that each quantitative ^{13}C-NMR experiment takes between 24-48 hours it was decided to use F_{1-3}SKL as a representative sample for the lower molecular mass fractions (recall that the molecular weight distribution, functional groups as determined by FT-IR, as well as the phenolic and aliphatic OH contents were found to be similar between F_1SKL, F_2SKL, F_3SKL and F_{1-3}SKL). Figure 3.5 and Figure 3.6 show the quantitative ^{13}C-NMR of acetylated F_{1-3}SKL (AceF_{1-3}SKL) and acetylated F_4SKL (AceF_4SKL). The corresponding peak assignments are listed in Table 3.4.

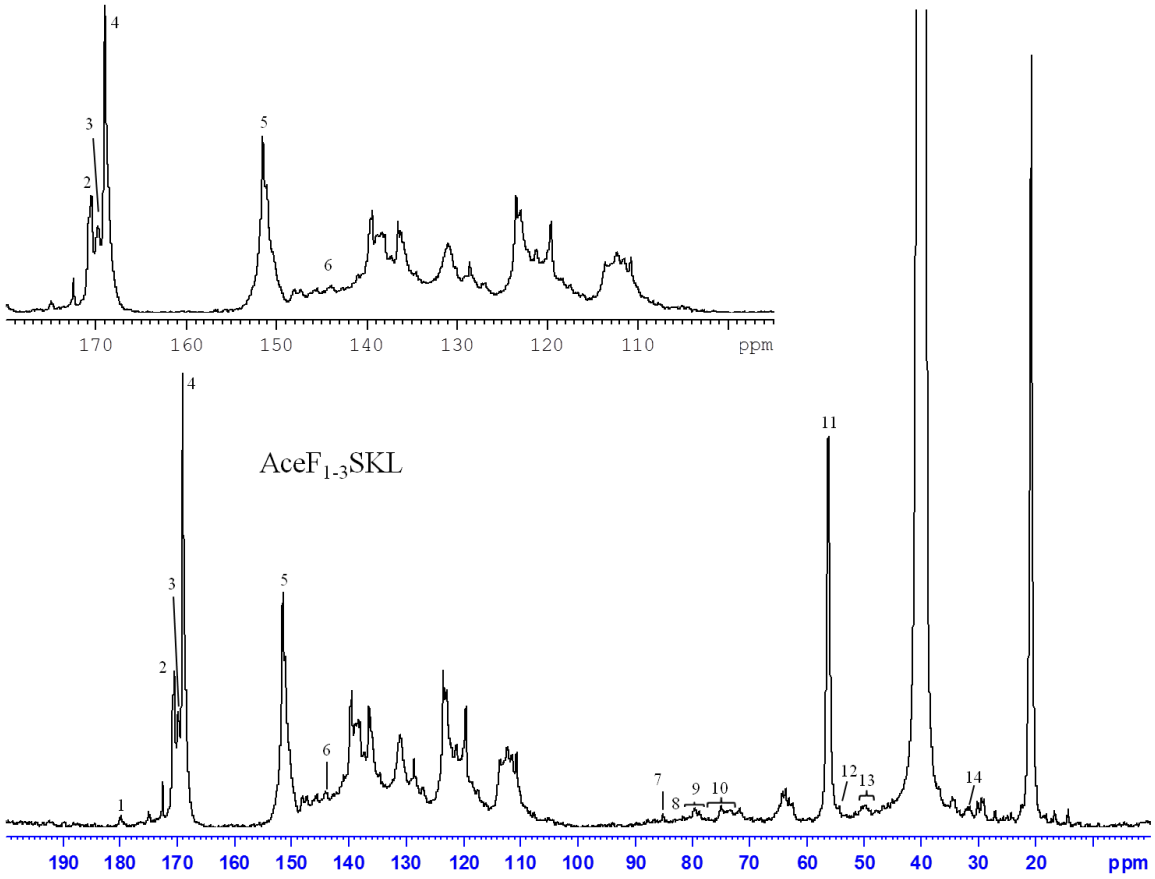

Figure 3.5 Quantitative ^{13}C-NMR spectrum (0 - 200 ppm) of acetylated F_{1-3}SKL, the area between 95-180 ppm is enlarged

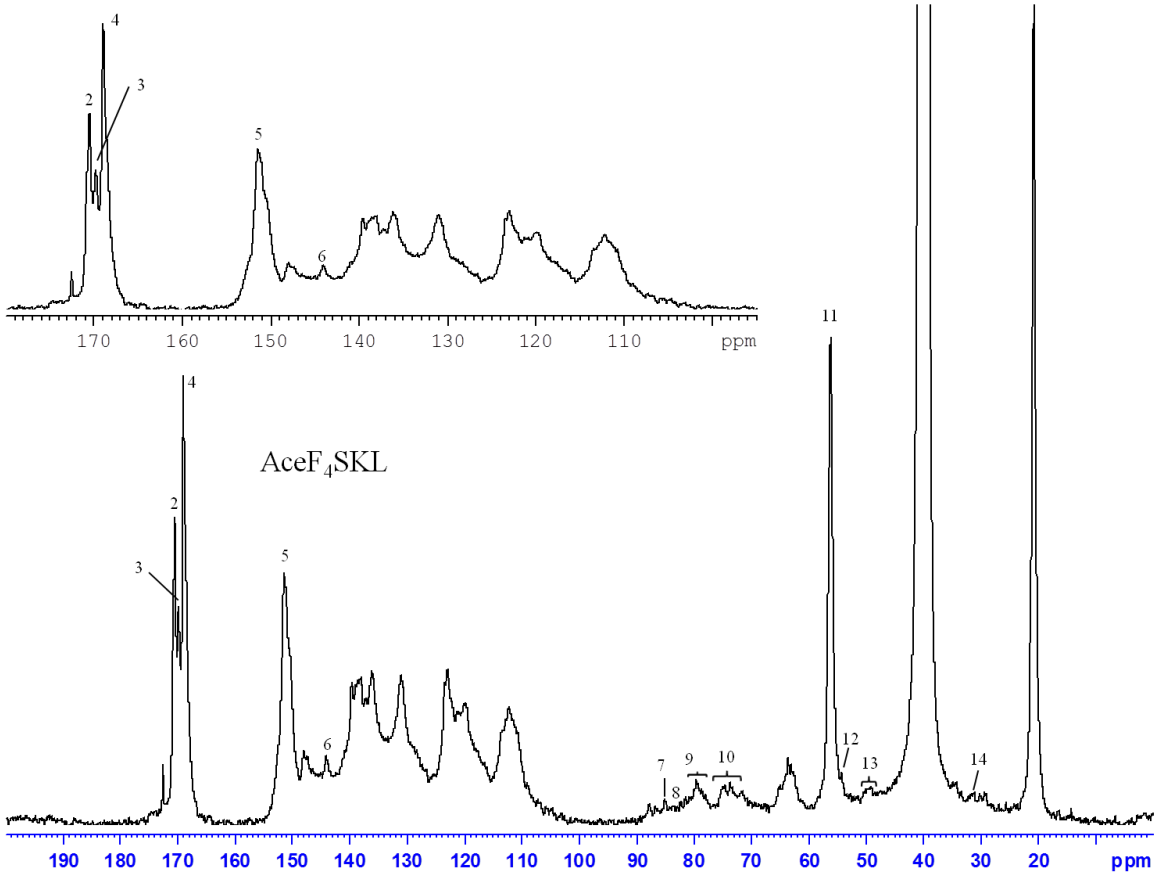

Figure 3.6 Quantitative ^{13}C-NMR spectrum (0 - 200 ppm) of acetylated F_4SKL, the area between 95-180 ppm is enlarged

Table 3.4 Signal assignment in the ^{13}C-NMR of acetylated $F_{1\text{-}3}$SKL and acetylated F_4SKL (*8*, *153*)

no.	$F_{1\text{-}3}$SKL	F_4SKL	Assignment	amount (per Ar) ($F_{1\text{-}3}$SKL/F_4SKL)
1	179.9	-	C4 in β-1	0.02/ -
2	170.5	170.5	Primary aliphatic C=O	0.30/0.33
3	169.8	169.8	Secondary aliphatic C=O	0.17/0.22
4	168.6	168.6	Aromatic C=O	0.70/0.64
5	162-148	162-148	C-3 (except in β-1/β-5), C-5 (in 4-0-5), C-4 in conjugated CO/COOR etherified units, C-α in coniferaldehyde	0.83/0.86
6	144.5-142.5	144.1-142.5	C-3 in β-5, C-4 in conjugated diaryl ether	0.11/0.17
7	88.1-86.0	88.1-86.0	C-α in β-5	0.02/0.04
8	86-83	86-83	C-α in β–β and DBDO	0.02/0.03
9	81.3-78.1	81.2-77.1	C-β in DBDO	0.08/0.17
10	77.2-72.4	77.2-72.4	α-OH/β-O-4	0.13/0.19
11	56.3	56.3	-OCH_3	0.80/0.86
12	54.3	54.3	C-β in β-β	0.03/0.07
13	51.1-48.6	51.1-48.7	C-β in β-5 and β-1	0.10/0.11
14	32.8-30.8	32.7-30.3	C-α in dihydroconiferyl alcohol	0.07/0.07
			Clusters	
	125-102		$C_{Ar\text{-}H}$	2.26/2.19
	90-58		Alk-O	0.72/1.08
	90-77		Alk-O-Ar, α-O-Alk	0.20/0.33
	77-65		γ-O-Alk, OH_{sec}	0.28/0.42
	65-58		OH_{prim}	0.24/0.32

Comparison of the two spectra reveals clear differences in the chemical structure of the two respective lignin fractions. First there is the clear appearance of peaks at 175 and 180 ppm (0.02/Ar) in the $AceF_{1\text{-}3}SKL$ that are not present in the $AceF_4SKL$. These correspond to the C4 position in β-1 structures and unconjugated aliphatic ester carbonyl groups. The region between 170.5-169.8 ppm and the peak at 169 ppm, which correspond to acetate carbonyl groups associated with primary/secondary aliphatic and aromatic hydroxyl groups, respectively, also differ with the amounts of both primary and secondary carbonyl groups from the acetylated groups in $AceF_4SKL$ being higher than in $AceF_{1\text{-}3}SKL$ (Table 3.4); 0.55/Ar for $AceF_4SKL$ versus 0.47/Ar for $AceF_{1\text{-}3}SKL$. Similarly, the aromatic hydroxyl content was lower in the $AceF_4SKL$ (0.64/Ar) as compared to that of the $AceF_{1\text{-}3}SKL$ (0.70/Ar). These results are consistent with those obtained from ^{1}H-NMR. The region between 144.5-142.5 that corresponds to C-3 in β-5 and C-4 in conjugated diaryl ether is higher in $AceF_4SKL$ (0.17/Ar) than $AceF_{1\text{-}3}SKL$ (0.11/Ar).

In the aliphatic region, C_α in pinoresinol and DBDO (the peak at 85.1 ppm) is higher in $AceF_{1\text{-}3}SKL$ (0.02/Ar) than $AceF_4SKL$ (0.03/Ar). $AceF_4SKL$ (0.17/Ar) exhibits higher C_β in DBDO (81-77 ppm) than $AceF_{1\text{-}3}SKL$ (0.08/Ar). As well C_α in β-aryl ethers is also higher in $AceF_4SKL$ (0.03/Ar) than $AceF_{1\text{-}3}SKL$ (0.02/Ar).The α-OH/β-O-4 is also higher in $AceF_4SKL$ (0.19/Ar) than in $AceF_{1\text{-}3}SKL$ (0.13/Ar) as is the methoxyl group content in $AceF_4SKL$ (0.86/Ar) as compared to $AceF_{1\text{-}3}SKL$ (0.80/Ar). $AceF_4SKL$ exhibited higher C-β in pinoresinal at 54.3 ppm (0.07/Ar) than $AceF_{1\text{-}3}SKL$ (0.03/Ar). These results support those observed from GPC analysis with the F_4SKL containing more of the traditional lignin linkages and may result in differing intermolecular interactions with MWNTs as compared to $F_{1\text{-}3}SKL$.

Estimations of the various lignin moieties were also made using the quantitative ^{13}C-NMR data (*8*). The amount of phenylcoumaran was estimated by integrating the region from 88-86 ppm to be 0.04/Ar for AceF_4SKL and 0.02/Ar for Ace$F_{1\text{-}3}$SKL. These integrals were then used to determine the β-1 (0.09/Ar and 0.09/Ar) structures in the AceF_4SKL and Ace$F_{1\text{-}3}$SKL by subtracting the phenylcoumaran integrals from 50-48 ppm. Most notable was the difference in the amount of β-O-4/α-OH linkages between the two fractions. Using the method of Capanema et al. (*8*) integrating the resonance at 77-72.5 ppm and correcting for some minor moieties, the amount of β-O-4/α-OH linkages per Aromatic unit was calculated to be 0.068/Ar in the F_4SKL while only 0.006/Ar in the $F_{1\text{-}3}$SKL. These values are lower than that reported for milled wood lignin (0.36/Ar) (*8*), as our moieties such as phenylcoumaran at 0.09/Ar. This could due to the Kraft pulping process which primarily degrades β-O-4 linkages and substantially modifies the native lignin structure.

3.1.5 Thermal analysis

SKL, F_1SKL, F_2SKL, F_3SKL, $F_{1\text{-}3}$SKL, and F_4SKL were characterized in terms of thermal and structural characteristics. As depicted in Figure 3.7 the TGA degradation profiles show that the residual weight of all of the lignin fractions with the exception of F_1SKL is around 45% at 600ºC, that of F_1SKL being only 20%.

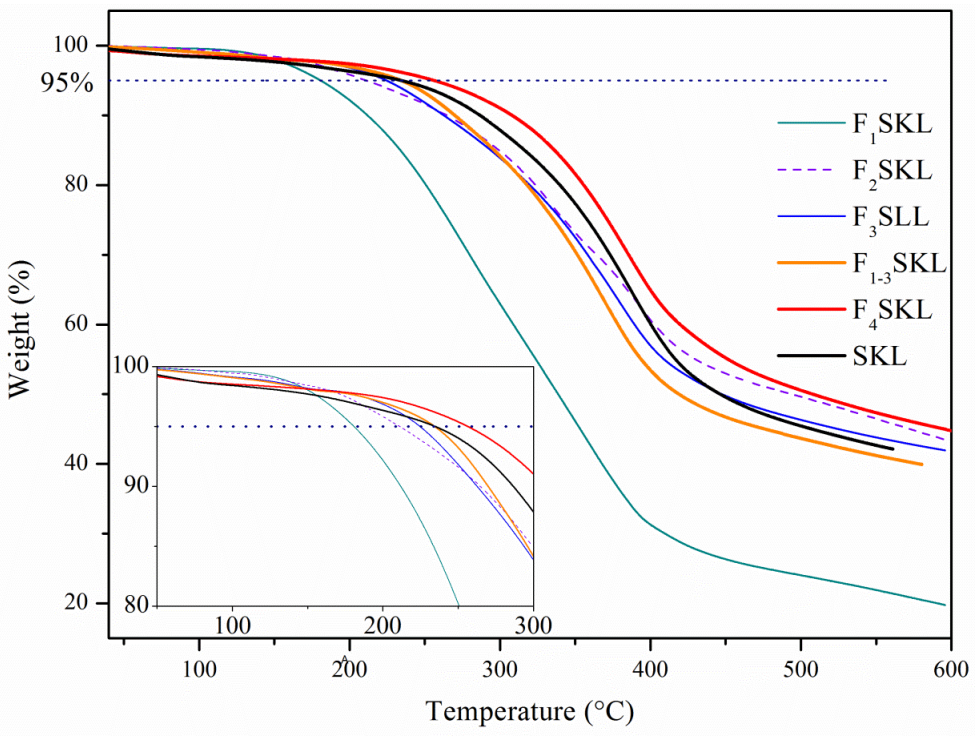

Figure 3.7 Thermograms of the various lignin fractions showing weight loss profiles as a function of temperature.

Also included in Figure 3.7 is an enlarged display of the temperature region wherein 5% weight loss occurs. F4SKL had a higher Td (260ºC) than SKL (242ºC), F1-3SKL (234ºC), F3SKL (223ºC), F2SKL (212ºC), and F1SKL (182ºC). Table 3.5 lists the average (of 3 replicates) Td and the peak maxima temperatures obtained from the DTGA curves (Figure 3.8).

Table 3.5 DTGA peak maxima and 95% decomposition (Td) temperatures obtained for the various lignin fractions

	Deriv. Weight loss	95% decomp (Td)
SKL	388.5 ± 4.4	241.7 ± 4.3
F_4SKL	390.7 ± 1.9	259.9 ± 4.3
$F_{1\text{-}3}$SKL	371.5 ± 1.1	234.4 ± 1.1
F_3SKL	355.9 ± 1.1	222.9 ± 2.5
F_2SKL	336.0 ± 6.1 352.4 ± 2.3 382.6 ± 10.5	212.1 ± 1.5
F_1SKL	277.9 ± 1.1 366.0 ± 3.5	181.8 ± 1.6

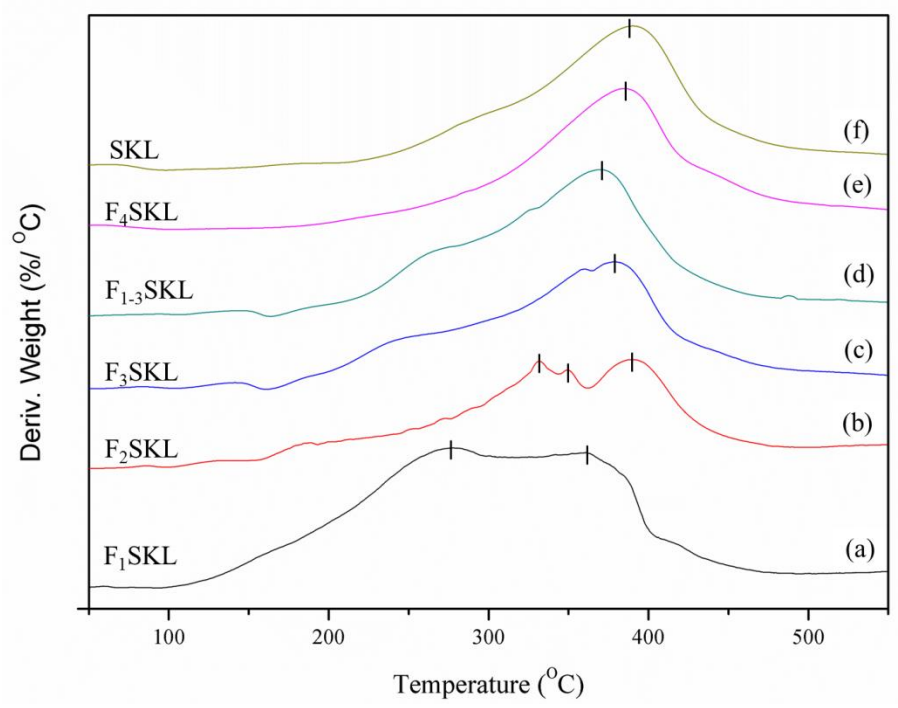

Figure 3.8 Derivative of weight loss as a function of temperature for samples of (a) F_1SKL, (b) F_2SKL, (c) F_3SKL, (d) $F_{1\text{-}3}$SKL, (e) F_4SKL and (f) SKL

All of the lignin fractions showed a broad DTGA curve with various shoulders. The DTGA curves of SKL and F_4SKL were very similar with a broad major peak at around 390ºC. In the case of the SKL a weak shoulder at around 300ºC was also observed. In the F_{1-3}SKL the main peak decreased to ~ 371ºC and a more pronounced shoulder was observed at ~ 270ºC. In the case of F_3SKL the major peak further decreased to ~ 360ºC as did the shoulder to ~ 250ºC. Both the F_2SKL and F_1SKL fractions exhibited multimodal decomposition profiles indicating the presence of a variety of components or linkages. The F_2SKL profile had a significantly higher main peak at 382ºC, comparable to that of SKL and F_4SKL and two weaker shoulders between 336-352ºC. A very distinct bimodal decomposition was observed in the F_1SKL with main peaks at ~ 260 and 370 ºC. These results clearly show that F_1SKL, F_2SKL, F_3SKL and F_{1-3}SKL are enriched in components that degrade at much lower temperatures than those of F_4SKL.

DSC curves for each of the lignin fractions are plotted in Figure 3.9. Since the fractions differed in their T_d, the maximum temperatures used in the DSC experiments were varied according to the T_d of each fraction in order not to decompose the samples in the instrument. As expected the F_1SKL exhibited the lowest Tg at 58ºC followed by F_2SKL at 91ºC, F_3SKL at 106ºC, and F_4SKL at 205ºC. The SKL Tg was 154ºC and interestingly that of the F_{1-3}SKL was 117ºC, higher than any of the component $F_1 - F_3$ fractions, potentially indicating strong interactions between the various fractions in the F_{1-3}SKL (*161*). The F_4SKL fraction exhibited the highest Tg among the 6 fractions, consistent with the measured T_d. According to the TGA and DSC results, the F_4SKL has a higher thermal stability and lower thermal mobility among the various fractions. This could imply that at higher temperature (such as 250 ºC of thermostabilization) it would

have less impact and degradation to F_4SKL based fibre than other fractions.

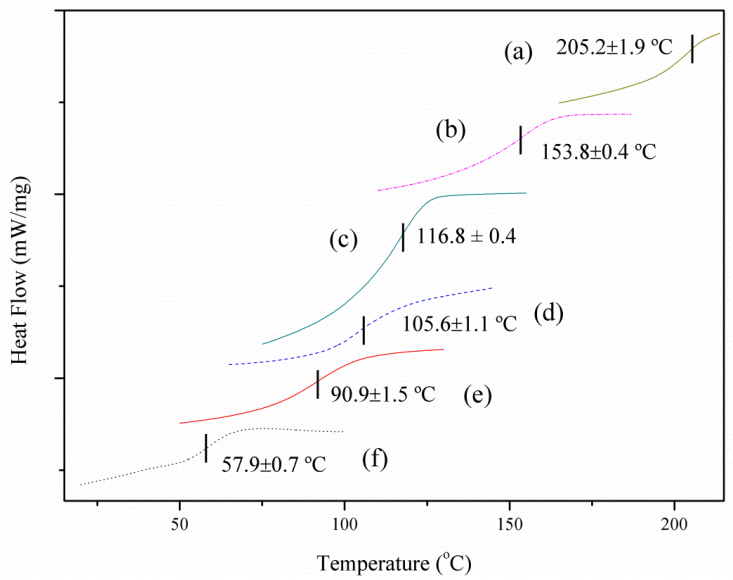

Figure 3.9 DSC profiles for the various lignin fractions (a) F_4SKL, (b) SKL, (c) $F_{1\text{-}3}$SKL, (d) F_3SKL, (e) F_2SKL, and (f) F_1SKL

3.2 Effect of lignin fractions on dispersion of MWNTs

From the characterization results it is evident that the different lignin fractions possess different molecular weights and degrees of lignin association, have differing amounts of aliphatic and phenolic hydroxyl groups, as well as different thermal mobility and stability. Therefore it is reasonable to assume that these differences might lead to differing abilities to interact and thereby disperse MWNTs. To investigate this and better study the mechanism by which lignin may disperse MWNTs, suspensions were prepared using varying amounts of MWNTs and the various and the dispersability characterized.

3.2.1 Optical images of MWNT suspensions

The effect of SKL and the various SKL fractions on the dispersion of MWNTs in DMF is shown in Figure 3.10. The optical micrographs clearly show that the MWNTs sonicated in the DMF alone are not well dispersed forming large aggregated flocs. However, in the presence of SKL a more uniform well-dispersed suspension is produced. Interestingly, the various SKL fractions behave quite differently. Suspensions sonicated with F_1SKL, F_2SKL, or F_3SKL had large MWNTs agglomerates similar to those observed in the absence of lignin. Not surprisingly similar results were obtained for $F_{1\text{-}3}$SKL. Interestingly, the suspensions containing F_4SKL appear very well dispersed. In fact, comparing the various optical images it appears that the relative apparent size of MWNT agglomerates in the F_4SKL is smaller than those obtained using the unfractionated SKL. i.e. F_4SKL better facilitates the dispersion of MWNTs than unfractionated SKL. These observations reveal that the different lignin fractions affect the extent of to which MWNTs can be dispersed, and that F_4SKL is likely the dominate fraction within SKL that can favorably interact with and disperse MWNTs.

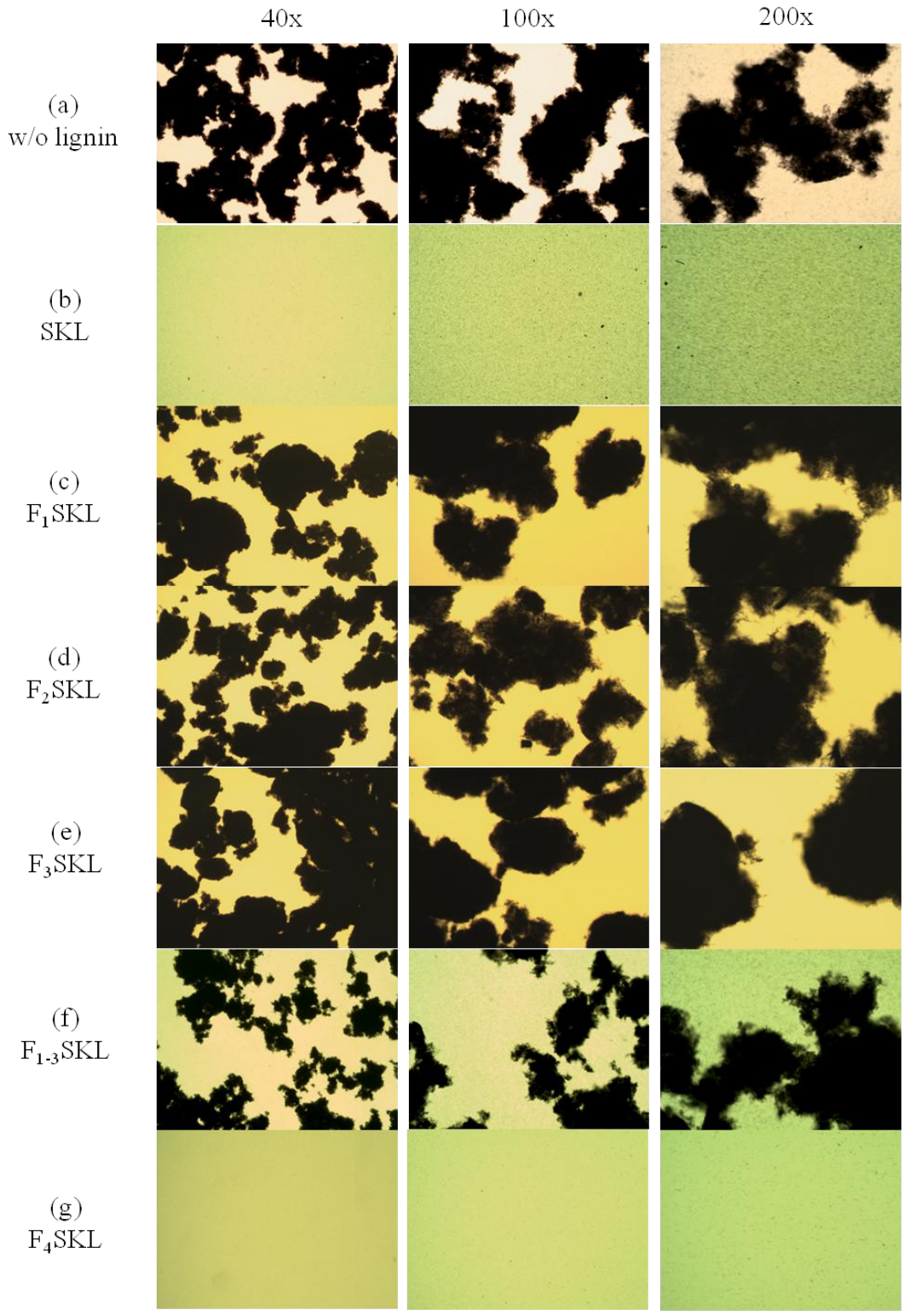

Figure 3.10 Optical microscope images of MWNT suspensions sonicated in DMF (a) without lignin and with (b) SKL (c) F_1SKL (d) F_2SKL (e) F_3SKL (f) $F_{1\text{-}3}$SKL (g) F_4SKL at 40x, 100x, and 200x magnification.

GPC-MALLS results showed that there was a clear difference in the propensity of the lignin fractions to associate into larger macromolecular complexes (Figure 3.1). Only the F_4SKL fraction showed the classic multimodal distribution typically associated with macromolecular association (*152, 155-157*). As our analyses were performed on acetylated samples in THF, it is unlikely hydrogen bonding is driving the association (*152*), rather electrostatic aromatic interactions are (*157, 158*). Therefore, our results indicate that associations due to the interaction between aromatic rings are less pronounced in F_1SKL F_2SKL, F_3SKL, and $F_{1\text{-}3}$SKL as compared to F_4SKL. As these are the same types of interactions reported to occur between CNTs (*149*) this may be a major driving force for their dispersion in the presence of lignin. It has been shown that lignins, although moderately soluble in DMF, form compact spherical structures indicative of macromolecular association (*162*). Since we observed a pronounced difference in the ability of the lignin fractions to disperse MWNTs in DMF, association or the underlying lignin interactions that cause association may play an important role in facilitating the dispersion of MWNTs. Specifically, during sonication the respective associations are disrupted and new interactions between lignin and MWNTs are formed; Propensity and extent depending largely on lignin structure. Further evidence supporting the role of hydrogen bonding in the dispersion of MWNTs by SKL was not evident. Although aliphatic hydroxyl groups form stronger intermolecular hydrogen bonds in lignin than phenolic hydroxyl groups (*154*), both $F_{1\text{-}3}$SKL and F_4SKL have approximately the same amount of aliphatic hydroxyl groups; indicating that hydrogen bonding between lignin and polar groups on the MWNT surfaces are less important than π--interactions.

Thus these results support that π-interactions and lignin structure likely play an important role in dispersing MWNTs. The association of F_4SKL, which is not observed in F_{1-3}SKL, and the larger molecule structure of F_4SKL than the other fractions indicate such π-interactions are more favored in this fraction. This may lead to F_4SKL interacting with the MWNTs through such interactions, and perhaps even physically preventing van der Waals attractions between MWNTs and the resulting reaggregate after sonication, i.e. F_4SKL self-association on the surfaces of the MWNTs. Moreover the F_1SKL F_2SKL, F_3SKL, and F_{1-3}SKL fractions, which do not self-associate into large supramolecular complexes, do not form such π-interaction with MWNTs and as such are not large enough to block such π-interactions between MWNTs. To better quantify the difference between SKL, F_4SKL and the other fractions in terms of MWNT dispersion, Raman spectroscopy was used.

3.2.2 Raman spectroscopy to analyze the dispersion of MWNT suspensions with various softwood Kraft lignin fractions

Raman spectroscopy has been used to characterize single-walled CNT dispersions in organic solvents (*147-149*). According to these studies the intensity of the tangential mode of carbon atoms that correspond to the stretching mode in the graphite plane, G band ($\mathbf{I_G}$), located between 1500 and 1630 cm^{-1} increases with concentration (*149*) and enhanced dispersion (*147*). Similarly, the aggregation of CNTs show differences in the radial breathing mode (RBM) region or D band ($\mathbf{I_D}$), known as the disordered or defect mode, usually located between 1330 and 1360 cm^{-1} (*148*). Therefore, by comparing the relative intensities of these two bands (I_G/I_D), a more quantitative assessment of MWNT dispersion can be made.

The results obtained from Raman spectroscopy are shown in Figure 3.11. As expected the MWNT suspensions, which appeared more dispersed in the optical images displayed higher G band intensity compared to the D band (I_G/I_D). The MWNT suspensions sonicated with SKL and F_4SKL were visually dispersed and exhibited a higher G band intensity compared to the D band, where the ratios of G band to D band intensities (I_G/I_D) were 0.67 and 0.98, for SKL and F_4SKL respectively. By contrast suspensions with F_1SKL, F_2SKL, F_3SKL, and $F_{1\text{-}3}$SKL exhibited weaker G band intensities and were visually aggregated. Table 3.6 lists the intensities of the D band (I_D), G band (I_G), and I_G/I_D ratios of the MWNTs suspensions with and without lignin. The data reveals a possible correlation between aggregation of MWNTs and I_G/I_D ratio; in fact the suspensions sonicated with F_4SKL visually appear dispersed and exhibit 8 times higher I_G/I_D ratios than suspensions sonicated without lignin.

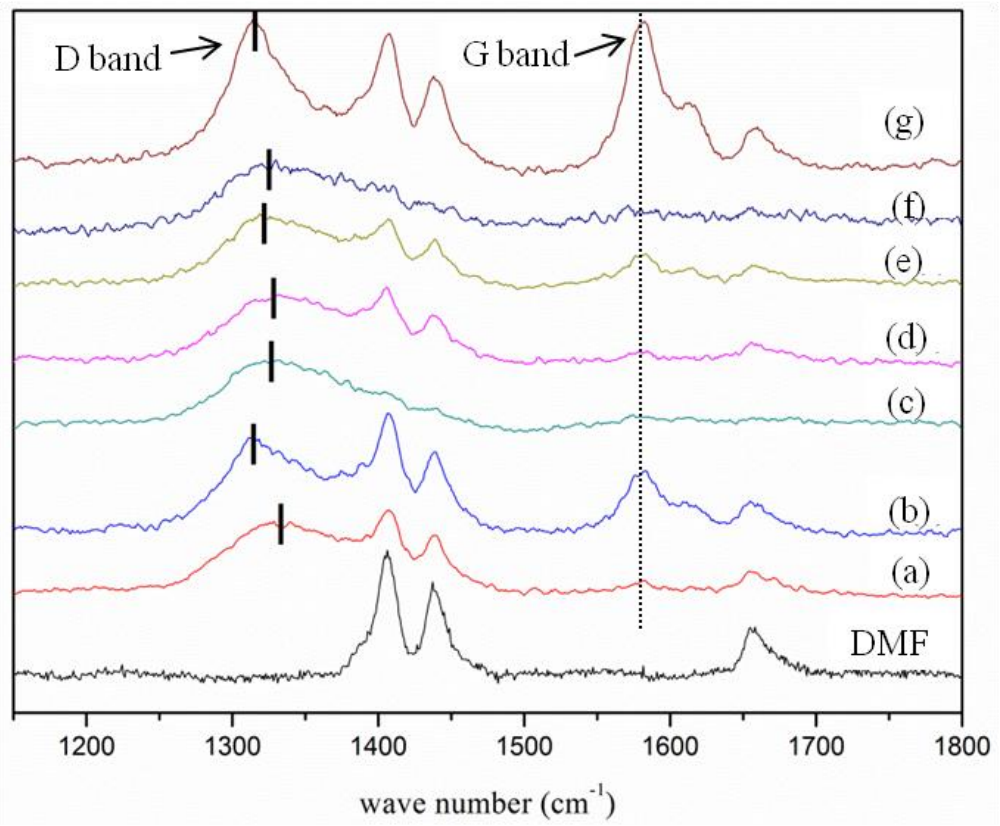

Figure 3.11 Raman spectra (1150 - 1800 cm^{-1}) of 1 mL DMF-MWNTs suspensions sonicated with 1mg SKL fractions. (a) DMF+MWNT, (b) DMF+MWNT+SKL, (c) DMF+MWNT+F_1SKL, (d) DMF+MWNT+F_2SKL, (e) DMF+MWNT+F_3SKL, (f) DMF+MWNT+F_{1-3}SKL, (g) DMF+MWNT+F_4SKL

Table 3.6 D band, G band, and I_G/I_D ratios of MWNTs suspensions (3.1 mg = 1 wt%) sonicated with various lignin fractions

Sample (MWNT/lignin)	D band (cm^{-1})	G band (cm^{-1})	I_G/I_D
3.1 mg /1mgSKL	1323	1584	0.67±0.13
3.1 mg /1mgF_1SKL	1338	1584	0.12±0.14
3.1 mg /1mgF_2SKL	1335	1581	0.16±0.04
3.1 mg /1mgF_3SKL	1336	1584	0.37±0.07
3.1 mg /1mgF_{1-3}SKL	1338	1579	0.12±0.09
3.1 mg /1mgF_4SKL	1322	1586	0.98±0.14
3.1 mg /without lignin	1333	1582	0.12±0.09

Further evidence supporting the correlation between dispersal of MWNTs and the intensities of D and G band was found by varying the concentration of F_4SKL in MWNTs suspensions (Figure 3.12).

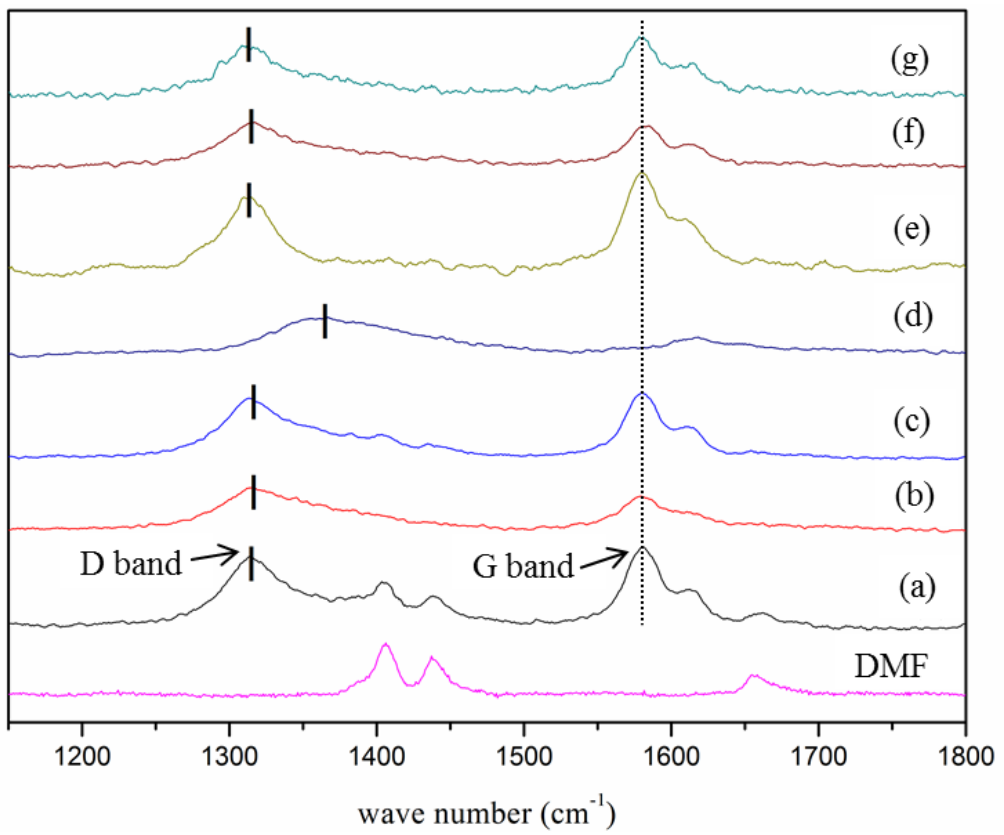

Figure 3.12 Raman spectra (1150 - 1800 cm^{-1}) of DMF and MWNTs suspensions contained (a) 6.2 mg, (b) 9.3 mg, (c) 12.4 mg, (d) 15.5 mg MWNTs sonicated with 1 mg F_4SKL and (e) 12.4 mg, (f) 15.5 mg, (g) 18.6 sonicated with 10 mg F_4SKL in 1 mL DMF.

Further evidence supporting the correlation between aggregation of MWNTs and I_G/I_D ratio was found by varying the concentration of F_4SKL in MWNTs suspensions. Specifically, suspensions of varying concentrations of both F_4SKL and MWNTs were prepared and the limitations of dispersion were determined by visual evaluation and Raman spectroscopy. The positions of the G and D bands as well as the I_G/I_D are listed in Table 3.7. The maximum MWNTs concentration that could be dispersed with 1 mg F_4SKL as measured by Raman spectroscopy was 12.4 mg of MWNTs (Figure 3.12). Beyond 12.4 mgs of MWNTs the suspensions with 1 mg F_4SKL start to aggregate, as

seen by the spectrograph of samples prepared with 15.5 mg MWNT (Figure 3.12d). In addition, the aggregated suspensions have broader D bands and shift to higher wavenumbers, similar to that observed in suspensions sonicated with lignin fractions F_1SKL, F_2SKL, F_3SKL and F_{1-3}SKL (Figure 3.11).

Table 3.7 D band, G band, and I_G/I_D ratios of MWNTs suspensions with varied MWNTs concentrations sonicated with different F_4SKL concentrations

Sample (MWNT/F_4SKL)	D band (cm^{-1})	G band (cm^{-1})	I_G/I_D
18.6 mg (=6 wt%)/10 mg	1316	1586	1.25±0.10
15.5 mg (=5 wt%)/10 mg	1320	1582	1.08±0.08
12.4 mg (=4 wt%) /10 mg	1315	1586	1.28±0.07
15.5 mg (=5 wt%) /1 mg	1336	1582	0.38±0.05
12.4 mg (=4 wt%) /1 mg	1320	1587	1.28±0.14
9.3 mg (=3 wt%)/1 mg	1312	1585	1.20±0.13
6.2 mg (=2 wt%) /1 mg	1320	1588	1.15±0.06

Increasing the F_4SKL concentration from 1 to 10 mg further increased the concentration of MWNT that could be dispersed in DMF. Using 10 mg F_4SKL the I_G/I_D ratio of the dispersions containing 15.5 mg of MWNTs (Figure 3.12f) increased from 0.38 (measured with 1 mg F_4SKL) to 1.08. Moreover, when sonicated with 10 mg F_4SKL in 1 mL DMF the concentration of MWNTs that could be successfully dispersed

increased to 18.6 mg MWNTs.

A potential explanation for the observed results is that when carbon nanotubes form bundles and aggregates, the contribution of the outer layers of MWNTs is likely higher than the inner graphite layers. Since the MWNTs used in this study were oxidized, it could be that the outer layers have more defects introduced into the carbon lattice despite the inner layers retaining a higher quality graphitic structure. In CNTs, it is known that the D band is also activated by the presence of heteroatoms, vacancies, grain boundaries, and other defects (*145, 146*). Thus, when MWNTs are more dispersed the incident laser would have a greater chance to detect the inner layers of the MWNTs, which may exhibit higher graphitization and result in a higher G band intensity; decrease in G band intensity has been previously reported for suspensions of bundled CNTs (*147*). Another possibility is that portions of the outer shell carbon lattice with a high degree of graphitic structure are the portions which are hidden in the MWNT aggregates. It has been reported that chemical modification opens the ends of CNTs (*163*). It may be that the higher D band observed comes from the ends of MWNTs protruding outward from MWNT aggregates while the more graphitic lattice occurring along the long axis of the MWNTs remains buried in large aggregates where they are less accessible to the incident laser beam.

Oxidization of CNTs form functional groups on their surface and help increase the dispersion of CNTs in DMF. After sonication, the oxidized CNTs may be moderately dispersed in DMF through intermolecular hydrogen bonding with the CNT surface carboxylic acid groups, as well as through van der Waals interactions arising from the dipolar polarization of DMF (*164*). However, as the system is allowed to equilibrate

re-aggregation of the CNTs occurs, as the attractive forces between CNTs are stronger than the dispersive forces of DMF. A similar phenomenon occurs in lignin/DMF solutions; lignin readily dissolves in DMF (*162*), but large macromolecular assembles form due to intra- and intermolecular π–π interactions between aromatic rings in lignin (*158*); i.e. the same as those reported for CNTs. Therefore, when lignin is added to the CNT/DMF system a complex system of intermolecular interactions involving lignin-lignin, CNT-CNT and lignin-CNT exist. Moreover, as the surfaces of the CNTs become "coated" with lignin, lignin-lignin association may occur leading to larger supramolecular complexes that physically block and preclude the attraction of CNTs, thus maintaining CNT dispersion. These complex intra- and intermolecular interactions leading to CNT dispersion is dependent on the lignin fraction, or lignin structure used.

3.3 Correlation between the degree of dispersion of MWNTs suspensions and electrospinning

The formation of a stable jet is critical to obtaining uniform fibres during electrospinning. In initial electrospinning experiments, it was evident that aggregation of MWNT in the spinning solution resulted in poor stability of the electrospinning process. To illustrate the effect of aggregated suspensions on the electrospinning process, electrospun fabrics were obtained from dispersed and aggregated MWNT suspensions, and are shown in Figure 3.13. Figure 3.13a shows the fabric produced from F_4SKL/PEO (99:1) without addition of MWNTs. It was shown that $F_{1\text{-}3}$SKL was less effective in dispersing MWNTs as compared to F_4SKL, therefore dispersed and aggregated MWNT suspensions were prepared by sonicating MWNTs (12.4 mg) with 1 mg of F_4SKL and $F_{1\text{-}3}$SKL, respectively in 1 mL of DMF followed by the addition of F_4SKL and PEO to

achieve the 25 wt% concentration needed for electrospinning (SKL wt% + PEO wt% + MWNT wt% = 25). The electrospun fabrics produced from the MWNTs dispersed in F_4SKL are uniform and continuous (Figure 3.13b), while those using $F_{1\text{-}3}$SKL show extensive electrospraying (Figure 3.13c), and a complete fabric could not be obtained. In addition, the darker fibre using F_4SKL to disperse MWNTs (compare to the fibres without addition of MWNTs) indicates the success of incorporating MWNTs in fibres. While the fibre using $F_{1\text{-}3}$SKL sprayed a lot with MWNTs particles (the dark part in the middle of collector) and with lighter color compared with fibres using F_4SKL. This shows that less MWNTs incorporating into fibres when using $F_{1\text{-}3}$SKL such that formed lighter fibre colour.

Figure 3.13 Images of electrospun fibres produced from (a) F_4SKL/PEO (99:1) DMF solutions without MWNTs and F_4SKL/PEO (96:1) DMF solutions containing 3wt% MWNT suspensions which sonicated with (b) F_4SKL and (c) $F_{1\text{-}3}$SKL. Total polymer concentration = 25wt%

Similar results were obtained when the concentration of MWNTs was increased beyond a critical limit. Although increasing the MWNT concentration from 9.3 mg to 12.4 mg in the presence of 1 mg of F_4SKL did not affect electrospinning, a further increase to 15.5 mg resulted in electrospraying and poor fibre formation (similar to

Figure 3.13c). Increasing the amount of F_4SKL during sonication allowed for higher MWNT concentration suspensions to be obtained.

Raman spectroscopy was shown be useful to evaluate the dispersion of MWNTs in SKL/DMF solutions by comparing the intensities of the G- and D-bands, I_G/I_D ratio. The G band representing the complete graphitization and purity of CNTs and carbon fibres and the D band representing disorder or defects *(145, 146)*. Dispersed MWNTs solution would result in stronger G band while aggregated suspension would show a low G band intensity. Investigated the correlation between the amount of F_4SKL and MWNTs dispersion we observed that in the samples prepared with 1 mg F_4SKL increasing the MWNT concentration from 6.2 mg to 12.4 mg formed dispersed MWNT suspensions. However, at 15.5 mg MWNT, the Raman spectrum appeared poorly resolved with a clear shift in the G- and D-bands observed and the solution was visually aggregated. This likely indicates the transition from the dispersed state at ~12.4 mg MWNT to one in which the suspensions starts to aggregate at ~ 15.5 mg MWNT. Increasing the F_4SKL content to 10 mg allowed 15.5 mg MWNT suspensions dispersed. At the higher F_4SKL content (10 mg) the MWNTs suspension concentration could be increased to 18.6 mg MWNTs in 1 mL DMF and still maintain a satisfactory I_G/I_D ~ 1.2. Increasing the amount of MWNTs to 21.7 mg in 10 mg F_4SKL solution formed visually agglomerates (data not shown) therefore 18.6 mg MWNTs was chosen as the highest concentration for this dispersion system.

Although a clear relationship between MWNT dispersion and electrospinning was found (vide infra) an unexpected behavior was observed as the content of lignin used to increase the amount of MWNT dispersed was increased. At 12.4 mg or 4 wt% MWNTs in the final fibre, both the 1 mg and 10 mg F_4SKL dispersion systems could form continuous fibres. However, when the MWNT content was increased to 18.6 mg or 6 wt% based on final fibre weight both the 1 mg and 10 mg F_4SKL dispersion systems formed droplets and even electrospray (1 mg dispersion system) during electrospinning. This instability in the electrospinning process in the 10 mg F_4SKL dispersion system occurred despite the MWNTs being well dispersed. Interestingly, when the amount of F_4SKL was increased to 100 mg (~ 1/3 of the total lignin) or further to 293 mg (or 100% of the total lignin used), stable electrospinning was obtained at the 6 wt% MWNT content. The higher amounts of F_4SKL better facilitates MWNT dispersion as more lignin is available to interact with the MWNT, thereby decreasing the possibility of agglomerate formation and leading to the more stable electrospinning process. Further increasing the MWNT content to 21.7 mg or 7 wt% in 100 mg F_4SKL dispersion system again resulted in droplets and electrospraying, and prohibited the collection of fibre mats (this was not surprising as it was a visually aggregated suspension). Therefore, the highest concentration of MWNTs used to study the impact on fibre properties and ensure the stability of the electrospinning process was 6wt% MWNTs for the 100 mg F_4SKL dispersion system, and 4wt% MWNTs when comparing to the 1 mg F_4SKL dispersion system.

3.4 Fibre morphology

SEM images of as-spun, thermostabilized, and carbonized fibres produced with and without MWNTs are shown in Figure 3.14. The fibre diameter was manually measured and listed in Table 3.8. A distinct difference in fibre morphology is apparent between the various fibres. Fibres with MWNTs curled after carbonization whereas no such morphology changes occurred in fibres without MWNTs. This is likely due to the difference in the extent of shrinking between F_4SKL and MWNTs (*90, 104*).

Table 3.8 Average diameter of fibres with varying MWNTs concentration at different heating stages (nm) (n=100) (The same alphabet labeled after data means no significant differences between groups)

Sample	As-spun	Thermostabilized	Carbonized
A) 0 wt% MWNT	977 ± 112^{c}	786 ± 96^{c}	639 ± 75^{c}
B) 1 wt% MWNTs	930 ± 98^{c}	784 ± 90^{c}	596 ± 65^{d}
C) 4 wt% MWNTs (1 mg F_4SKL)	769 ± 98^{d}	730 ± 77^{d}	579 ± 84^{d}
D) 4wt% MWNTs (100 mg F_4SKL)	1305 ± 129^{a}	864 ± 102^{b}	722 ± 42^{b}
E) 6wt% MWNT	1170 ± 141^{b}	1107 ± 96^{a}	816 ± 91^{a}

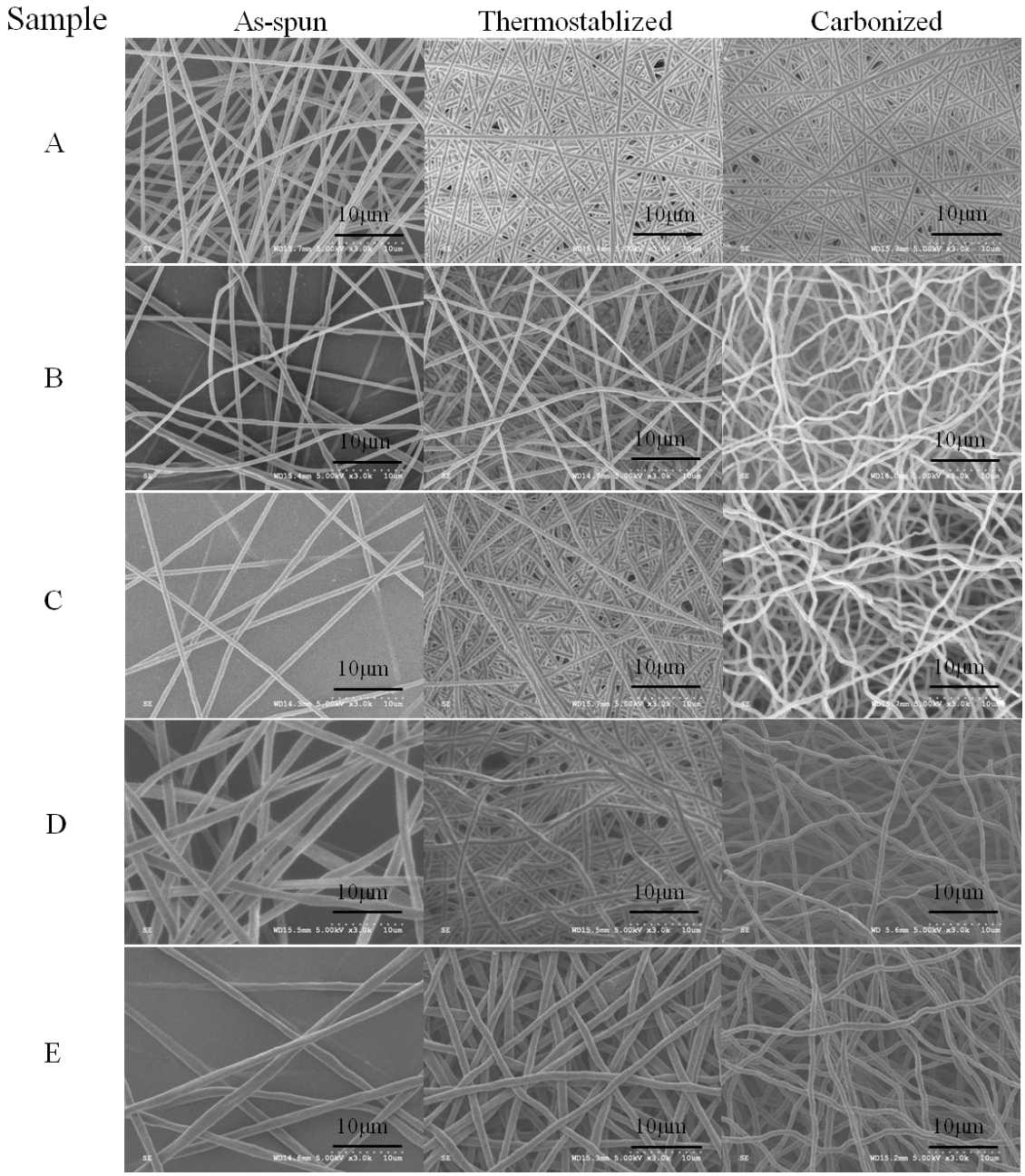

Figure 3.14 SEM images of as-spun, thermostabilized and carbonized fibres of sample A to E. (A: F_4SKL:PEO:MWNT =99:1:0; B: F_4SKL:PEO:MWNT = 98:1:1; C: F_4SKL:PEO:MWNT = 95:1:4 (sonicated with 1 mg F_4SKL); D: F_4SKL:PEO:MWNT = 95:1:4 (sonicated with 100 mg F_4SKL); E: F_4SKL:PEO:MWNT = 93:1:6)

The fibre diameters of the electrospun fibres decreased with increasing MWNT content from 977 nm (sample A – no MWNT) to 769 nm (sample C – 4 wt% MWNT; 1 mg F_4SKL). This trend was also observed in the thermostabilized and carbonized fibre diameters (Table 3.8). Interestingly, when the F_4SKL content used to disperse the MWNT was increased from 1 mg to 100 mg a significant increase in fibre diameter was observed; 769 nm (sample C – 1 mg F_4SKL/4 wt% MWNT) vs 1305 nm (sample D – 100 mg F_4SKL/4 wt% MWNT). This increase in fibre diameter may be a result of higher spinning solution viscosities arising from a more dispersed and interconnected network structure. It is known that electrospun fibre diameter is influenced by solution viscosity (*73, 74*), and it has been reported that CNTs can lead to physical contacts between unentangled particles in fluids, forming three-dimensional networks such that the viscosity of the suspension increases (*165*).

The presence of MWNTs in the fibres was confirmed through TEM. The MWNTs are clearly visible as darker tubular structures embedded in the lignin fibre (Figure 3.15). The outer diameter of MWNTs measured from TEM images was ranging from 30 to 60 nm. Due to the large diameter of the F_4SKL based fibres, thinner fibres were selected to show the presence of MWNTs within the fibre. Therefore, the fibre diameters shown in the TEM images are not representative of the actual fibre diameters. Images of thermostabilized and carbonized fibres containing 4 wt% MWNT show MWNTs protruding out of the ends of fractured fibres. This illustrates MWNT pullout during fracture, indicating poor interfacial interaction between the fibre matrix and the MWNTs (*125*). Interestingly, this MWNT pullout occurred only in the thermostabilized, and carbonized fibres, and was not observed in the as-spun fibres. This may indicate that

during the thermal processing changes in the lignin structure and resulting properties decrease the interaction/compatability with the MWNTs.

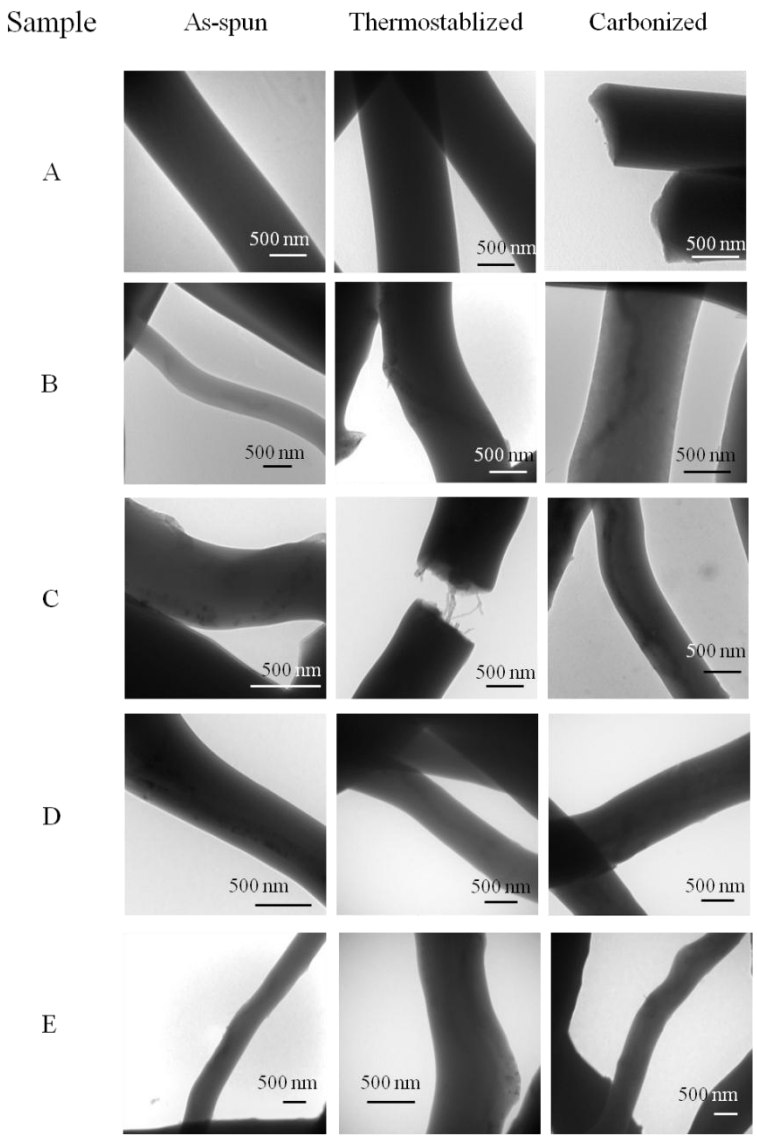

Figure 3.15 TEM images of (a) as-spun (b) thermostabilized and (c) carbonized fibres with varied MWNTs concentration. (A: F_4SKL:PEO:MWNT =99:1:0; B: F_4SKL:PEO:MWNT = 98:1:1; C: F_4SKL:PEO:MWNT = 95:1:4 (sonicated with 1 mg F_4SKL); D: F_4SKL:PEO:MWNT = 95:1:4 (sonicated with 100 mg F_4SKL); E: F_4SKL:PEO:MWNT = 93:1:6)

3.5 Determination of the graphitization of lignin based carbon fibre by X-ray diffraction (XRD) and Raman spectroscopy

XRD was carried out to characterize the graphitization of carbon fibres. Figure 3.16 shows representative XRD patterns of the various samples A-E along with that of the MWNT. In the MWNTs, the sharp peak at 30.4° corresponds to the diffraction of highly ordered graphite (002) and the other two peaks correspond to the lattice planes (100) and (004) at 50.4° and 63.3°, respectively. (*166*) The corresponded interatomic spacing of the planes is also labeled in Figure 3.16. The graphite (002) peak was also apparent in the SKL-based carbon fibres which contained MWNTs confirming their presence in the carbon fibres (*167*). As expected the peak intensity increased with MWNTs concentration (Figure 3.16) (*90, 168*).

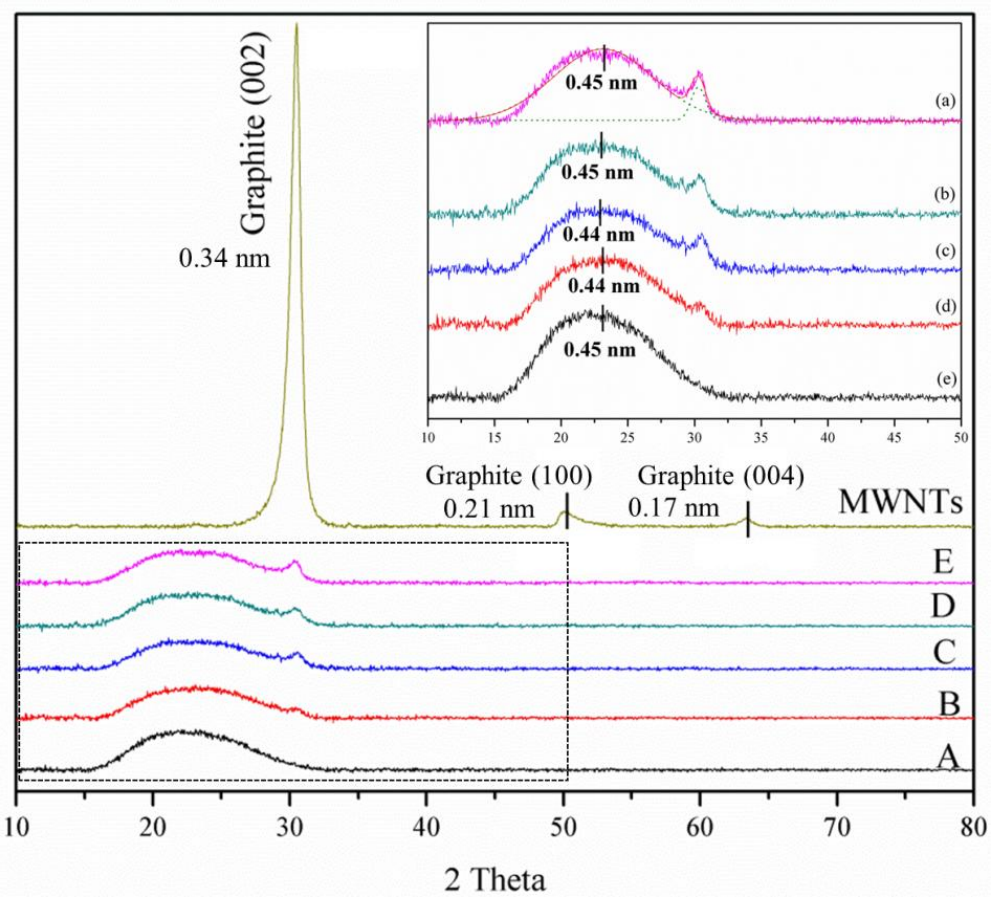

Figure 3.16 XRD pattern of carbon fibres containing different MWNTs concentration (A-E) and plain MWNTs. (A: F_4SKL:PEO:MWNT =99:1:0; B: F_4SKL:PEO:MWNT = 98:1:1; C: F_4SKL:PEO:MWNT = 95:1:4 (sonicated with 1 mg F_4SKL); D: F_4SKL:PEO:MWNT = 95:1:4 (sonicated with 100 mg F_4SKL); E: F_4SKL:PEO:MWNT = 93:1:6)

The broad band in the SKL-based samples from 15 – 33° is from amorphous carbon suggesting that the lignin-based carbon fibre was still amorphous after heating to 1000°C. This band appears to have a bimodal pattern, however extending the scanning time (data not shown) did not increase the resolution or lower the signal to noise ratio to clarify this. The amorphous carbon band did not shift with increasing MWNTs concentration or the presence of MWNTs (Figure 3.16) and the diffraction patterns show no significant

difference between fibres with varied MWNTs concentrations. This suggests that the interatomic spacing of lignin carbon fibres did not change with incorporation of MWNTs.

Further information regarding the graphitization or lack thereof in the lignin-based carbon fibres were observed using Raman spectroscopy. Figure 3.17 shows the Raman spectra of carbon fibres with 6 wt% MWNTs and 0 wt% MWNTs. The graphitization of carbon fibres is usually represented as the ratio of the $I_D/I_G = R$; in graphite a lower ratio represents a higher graphitization. The ratios for D and G band intensities of 0 wt% and 6 wt% were both 1.854. Also, both the G band and D band did not shift or change in shape with addition of 6 wt% MWNTs. The absence of the (100) lattice plane in the XRD of the lignin carbon fibre could indicate that the lateral size (L_a) is less than 2 nm and corresponds to the range of nanocrystalline graphite (*145*). While Raman spectroscopy only analyzes the surface structure down to ~10 nm depth (*169*), it is possible that the interfacial region between lignin-derived carbon and MWNTs could be slightly more graphitic; however, the XRD patterns were too noisy to confirm if any increase in graphitic structure occurred. These observations support that the embedded MWNTs did not increase the graphitization of lignin-based carbon fibre. In studies involving PAN-based carbon fibres (*170, 171*), the embedded MWNTs could act as crystallization site (*172*), such that they induce the growth of carbon crystals and crystalline regions become more ordered with increased MWNTs content. Since lignin is intrinsically heterogeneous, amorphous/nonlinear in structure, and has complex thermal decomposition chemistry (*173*), it would be difficult to expect that ordered layer aligned MWNTs would form during carbonization.

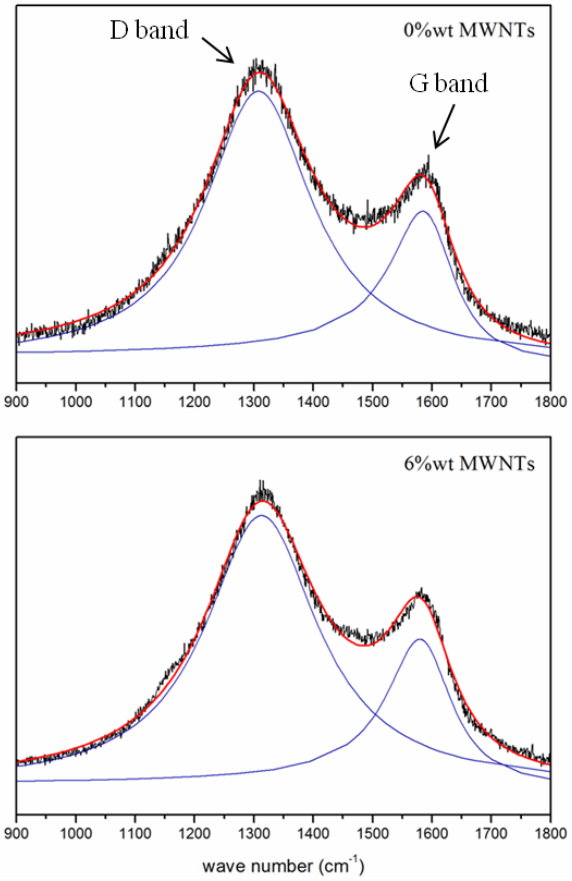

Figure 3.17 Raman spectra of carbon fibres prepared from F_4SKL/PEO with 0wt% MWNT (top) and 6wt% MWNTs (bottom)

3.6 Tensile testing of lignin based fibres

Tensile testing was carried out to characterize fibre mechanical properties in terms of strength, modulus, elongation, and toughness for as-spun, thermostabilized, and carbonized fabrics. Results are shown in Figure 3.18 - Figure 3.21.

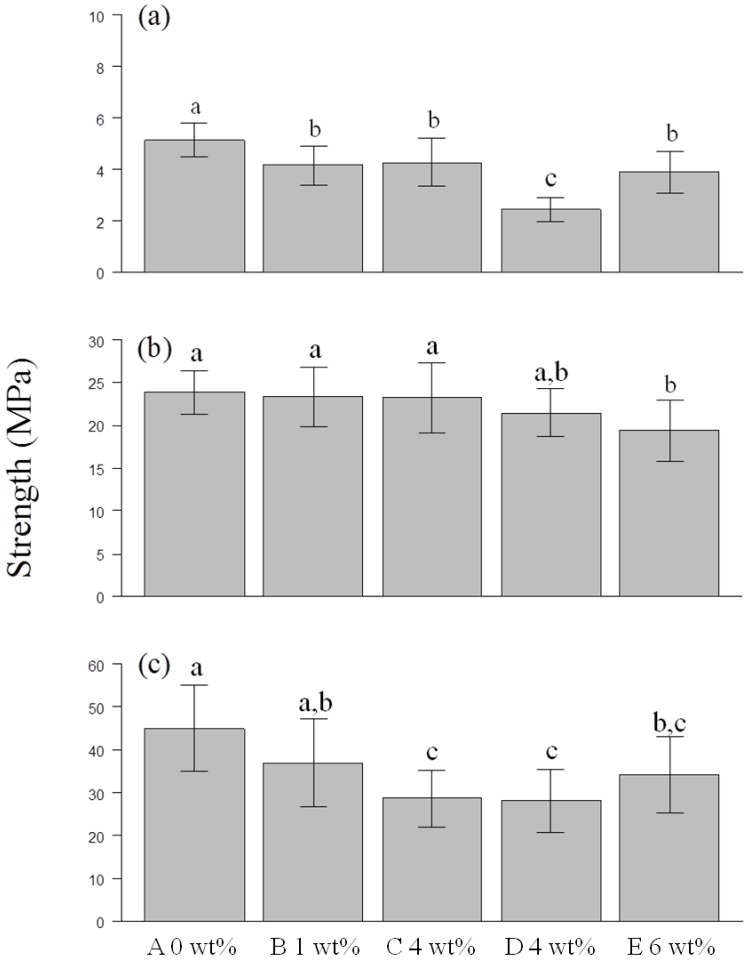

Figure 3.18 Bar-plots of (a) as-spun (b) thermostabilized and (c) carbonized fibres strength (MPa) (A: F_4SKL:PEO:MWNT =99:1:0; B: F_4SKL:PEO:MWNT = 98:1:1; C: F_4SKL:PEO:MWNT = 95:1:4 (sonicated with 1 mg F_4SKL); D: F_4SKL:PEO:MWNT = 95:1:4 (sonicated with 100 mg F_4SKL); E: F_4SKL:PEO:MWNT = 93:1:6) (The same alphabet labeled above the bar means no significant differences between groups)

The addition of 1 wt% MWNTs resulted in a decrease in the strength of the as-spun fibres, from 5.13 to 4.16 MPa for the fibres produced using the 1 mg F_4SKL dispersion system. Further increasing the MWNT loading to 4 wt% (1 mg F_4SKL) did not decrease the as-spun fibre strength any further. However, as fibre diameter can influence

mechanical performance of electrospun fibres; finer fibres generating higher strength and modulus (*86*), the larger diameter as-spun fibres produced using the 100 mg F_4SKL dispersion system had dramatically reduced strength, decreasing to 2.46 and 3.98 MPa for 4 and 6 wt% MWNT loadings, respectively. For the thermostabilized fabrics, the measured strength again trended with fibre diameter; only the larger 6 wt% MWNT containing fibres saw a decrease in strength from an average of ~23 to 19.4o MPa. By contrast the strength of the resulting carbon fibres decreased with increasing MWNTS addition up to 4 wt% and then slightly increased at 6 wt% MWNTs. Unlike the as-spun fibres, there was no difference in the carbon fibre strength between the two F_4SKL dispersion systems. In general, the addition of MWNTs did not improve the strength of the lignin-based fibres in any of the three different heating stages. This is in contrast to results reported for PAN-based fibres, where fibre strength increased with the inclusion of 10 wt% MWNTs (*103*). In that study (*103*), a rough surface morphology was observed in the PAN based fibres incorporating MWNTs, and the encapsulated MWNTs were ordered and oriented along the axis of the nanofibre. In our lignin-based carbon fibres the MWNTs, although roughly orientated along the fibre, were poorly ordered and more randomly aligned (Figure 3.15); the random order manifesting in the observed curly morphology after carbonization, as well as the poor mechanical performance.

On the other hand, the fibre modulus of both as-spun and thermostabilized fibres increased with the addition of MWNTs (Figure 3.19). The addition of 4 wt% MWNT (sonicated with 1 mg F_4SKL) increased the modulus from 514 to 663 MPa and 918 to 1070 MPa for the as-spun and corresponding thermostabilized fibres, respectively. However, when the fibres were subsequently carbonized significant decrease in modulus

was found in all of the MWNT reinforced fibres as compared to the control lignin-based carbon fibres; decreasing from 6238 to 4648 MPa with only 1 wt% MWNT addition and further to ~2400 MPa with 4 wt% MWNT. The decreasing tendency in modulus for the carbon fibres may be related to the carbon fibre morphology (Figure 3.14) that was clearly affected by the incorporation of MWNTs, specifically the curled morphology.

Similar behavior was observed for fibre elongation and toughness (Figure 3.20 and Figure 3.21). The addition of MWNT in as-spun fibres also decreased the elongation from 1.73% (fibres without MWNTs) to 1.05% (4 wt% MWNTs sonicated with 1 mg F_4SKL) while the fibres with MWNT loading increased to 6 wt% (1.44%) possessed the same elongation as fibres without MWNTs (Figure 3.20). However, the addition of MWNTs decreased the elongation of thermostabilized fibres from 3.12% (fibres without MWNTs) to 2.08% (4 wt% MWNTs sonicated with 1 mg F_4SKL). The thermostabilized fibres with different loading of MWNTs possessed the same elongation. In carbon fibres, the addition of 1 wt% MWNTs (0.97%) had the same elongation as fibres without MWNTs (0.76%). Elongation increased with 4 wt% MWNTs loading or more from 0.76% to 1.42.

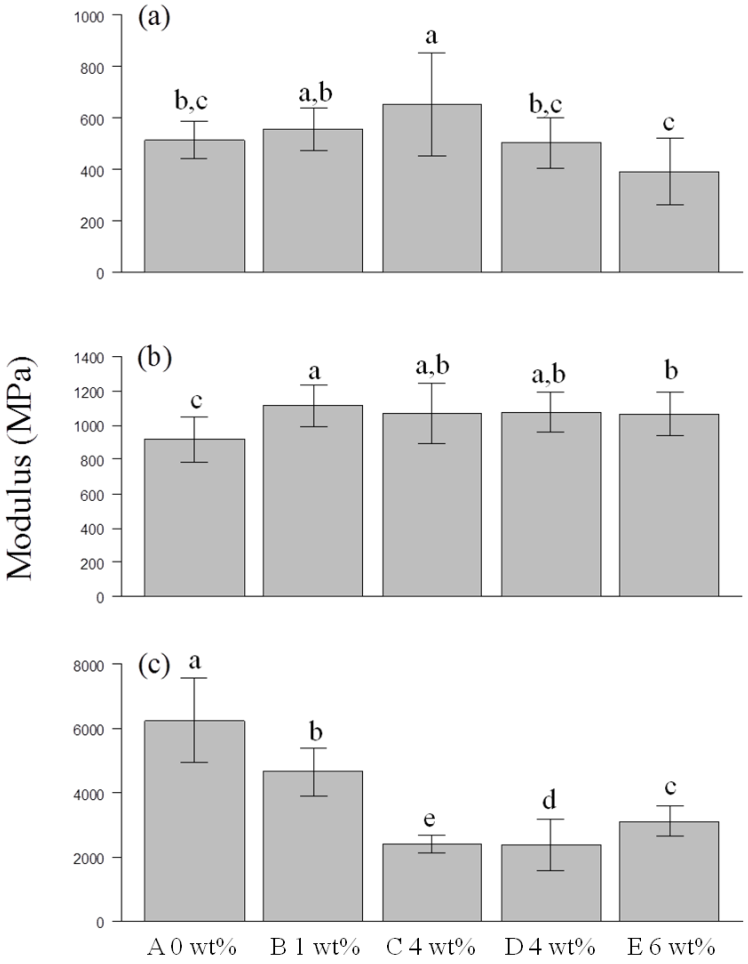

Figure 3.19 Bar-plots of (a) as-spun (b) thermostabilized and (c) carbonized fibres modulus (MPa) (A: F_4SKL:PEO:MWNT =99:1:0; B: F_4SKL:PEO:MWNT = 98:1:1; C: F_4SKL:PEO:MWNT = 95:1:4 (sonicated with 1 mg F_4SKL); D: F_4SKL:PEO:MWNT = 95:1:4 (sonicated with 100 mg F_4SKL); E: F_4SKL:PEO:MWNT = 93:1:6) (The same alphabet labeled above the bar means no significant differences between groups)

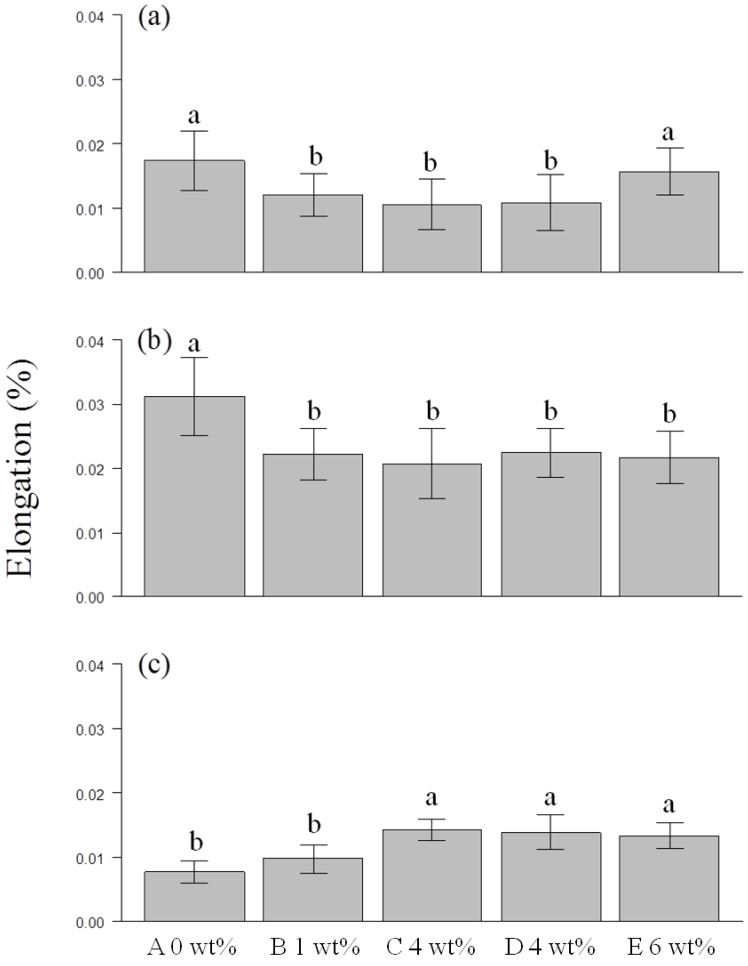

Figure 3.20 Bar-plots of (a) as-spun (b) thermostabilized and (c) carbonized fibres elongation (%) (The same alphabet labeled above the bar means no significant differences between groups)

Toughness decreased in as-spun fibres with 1 wt% addition of MWNTs from 38.55 (fibres without MWNTs) to 25.26 kJ/m^3 (Figure 3.21). The fibres with 4 wt% MWNTs loading (sonicated with 1 mg and 100 mg F_4KSL) possessed the same toughness as fibres contained 1 wt% MWNTs. When increased to 6 wt% MWNTs loading in as-spun fibres, the toughness increased to 26.92 kJ/m^3 while is still lower than fibres without MWNTs. In thermostabilized fibres, toughness decreased with addition of MWNTs from 436.59 to

181.68 kJ/m^3 (fibres with 6 wt% MWNTs). The loading of 1 wt% and 4 wt% MWNTs (sonicated with 1 and 100 mg F_4SKL) had the same toughness between 229 and 251 kJ/m^3. Toughness remained unchanged in carbon fibres without or with 1 to 6 wt% MWNTs loading in fibres.

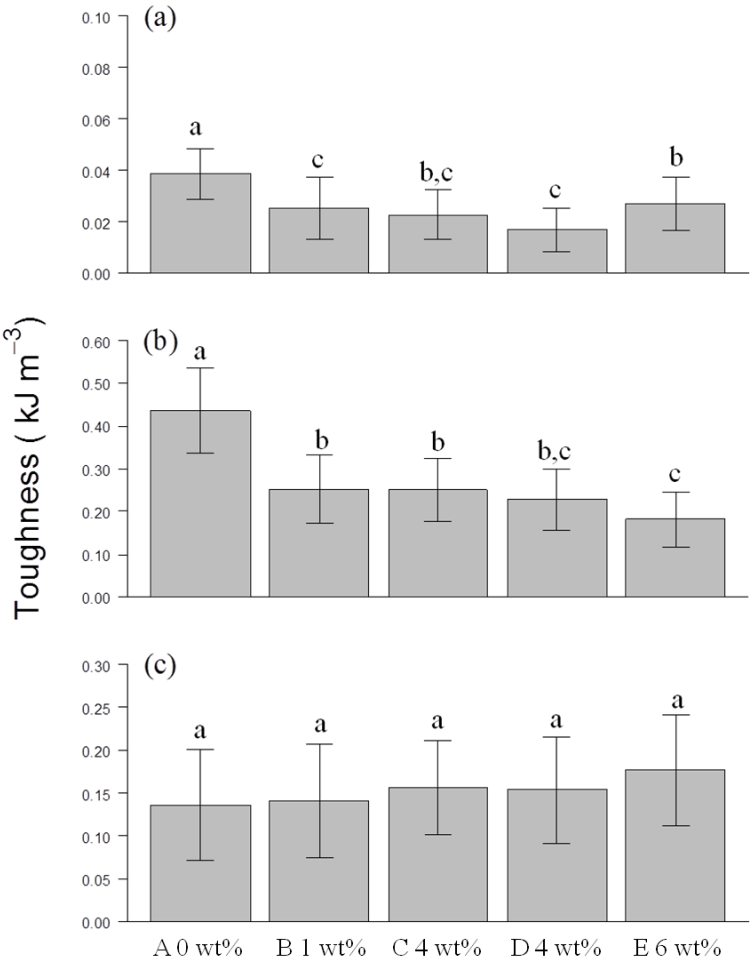

Figure 3.21 Bar-plots of (a) as-spun (b) thermostabilized and (c) carbonized fibre toughness (kJ/m^3) (The same alphabet labeled above the bar means no significant differences between groups)

The decreased strength and modulus with incorporation of MWNTs may be due to the poor interfacial interaction between the MWNTs and lignin. The TEM images support a poor interaction between thermostabilized and carbonized fibres and MWNT, as evident by the MWNT pullout observed at fracture ends of the fibres. There are four key requirements for fibre reinforcement: aspect ratio, dispersion, alignment, and interfacial stress transfer (*174*). Dispersion and interfacial association are the two most important aspects. Although the requirement for dispersion was met, reinforcement really depends on the ability to transfer load from the matrix to the CNTs (*175*). A more ordered interface and better interfacial interaction could improve the stress transfer to MWNTs (*176*), however lignin is amorphous and is intrinsically a disordered phase, leading to poor MWNT alignment and failure in mechanical reinforcement. XRD and Raman observations support that the addition of MWNTs did not increase the graphitization in lignin-based carbon fibres. In addition, the concentration of MWNTs in these fibres could be beyond a certain threshold where their distributions are not very dispersed in the fibre during the electrospinning. Instead the conditions lead to aggregation of MWNTs, which in turn decreases the fibre mechanical properties (*90, 103, 174-177*).

3.7 Electrical conductivity of MWNT incorporated in lignin based carbon fibres

In addition to fibre reinforcement for mechanical property improvement, CNT incorporation has been shown to improve electrical conductivity when incorporated into fibres (*46, 101-104*). Increasing the incorporation of MWNTs from 0 to 4wt% (sonicated with both 1 mg and 100 mg F_4SKL), did not affect the measured electrical conductivity. When the MWNT content was increased to 6wt% the electrical conductivity of the carbon fibres moderately increased from 2.31 to 2.98 S/cm (Table 3.9). However, the

large standard derivation indicates the apparent improvement is not significant.

MWNTs possess electrical conductivities between 1.7×10^{-1} to 2.0×10^{5} S/cm (*178*) and the conductivity performance is influenced by the chirality of CNTs (*179*). When the graphene is rolled into a nanotube, the hexagons may spiral around the cylinder, giving rise to “chirality”, a twist that determines whether the CNT behaves like a metal or a semiconductor, the latter resulting in the enhancement in electrical conductivity being not significant. The MWNTs used in this study are oxidized and showed a strong D band (*180*) similar in intensity to the G band, which indicates a less ordered sp^2 CNT structure with a high quantity of defects (*181*). As the MWNTs used in this study have electrical conductivities of > 100 S/cm, it could be that they are more semiconductive, instead of metallic, thus the conductivity of the fibres would not be expected to increase significantly.

Table 3.9 Electrical conductivity of carbonized F_4SKL/PEO fabrics with varying MWNT concentrations (n=10)

Samples	Conductivity (S/cm)
A 0 wt% MWNT	2.31 ± 0.78
B 1 wt% MWNTs	2.11 ± 0.41
C 4 wt% MWNTs (1 mg F_4SKL)	2.14 ± 0.32
D 4wt% MWNTs (100 mg F_4SKL)	2.21 ± 0.26
E 6wt% MWNT	2.98 ± 1.31

PAN-based carbon fibres have been reported with electrical conductivities of between 0.5 to 1.42 S/cm (*93, 104*) using thermostabilization temperatures of 260 and 280°C. While Bayat *et al.* (*25*) also produced PAN based fibres with electrical conductivity of 2.6 S/cm, and thermostabilized at 250°C (the same thermostabilization temperatuer as our fibres), PAN based carbon fibres produced in our lab had electrical conductivity values of 9.59 S/cm. This clearly illustrates that it is extremely difficult to compare values from fibres produced using different conditions and from different labs. The electrical conductivity of the F_4SKL based carbon fibres produced in our study possessed a conductivity of 2.31 S/cm, which is comparable to the result from Bayat *et al.* (*25*). However, unlike the PAN based fibres where incorporating 7.5wt% MWNTs substantially increased the electrical conductivity from 0.5 to 8 S/cm (*104*), such a significant increase in electrical conductivity was not observed in the F_4SKL fibres. In

addition to the processing conditions used, there is another possibility that the MWNTs used in our study are not metallic, which we can speculate from the results of Raman spectroscopy, along with the amorphous carbon and poorer orientation of MWNTs in lignin fibres as compared to PAN fibres resulting in poor electrical conductivity.

4 Conclusion

Results of lignin characterizationrevealed that F_4SKL exhibited the highest molecular weights among lignin fractions and only SKL and F_4SKL exhibited the multimodal distribution which is related to the association of lignin and lignin molecules while the other fractions did not show this. This self-assembled aggregation could be a result of interactions between aromatic rings in lignin and is the important factor of dispersing MWNTs It supports the hypothesis that the structure of lignin plays an important role in facilitating the dispersion of MWNTs. Hydroxyl group and interunit linkage contents were found to be different in the various lignin fractions. No direct evidence was found to support hydrogen bonding between lignin and the oxidized MWNT surface attributed to the dispersion of the MWNTs. Therefore, it is proposed that π-interaction between aromatic rings is the major driving force for MWNT dispersion.

Raman spectroscopy has the potential to quantify the dispersion of MWNTs. A correlation between the degree of dispersion of MWNTs and the G band intensity in Raman spectroscopy was observed. Dispersed suspensions resulted in higher G band intensity while aggregated suspensions exhibited weak G band intensities. Raman also revealed that F_4SKL is likely the primary component that enables the unfractionated SKL to sufficiently disperse the MNWTs. Furthermore, Raman spectroscopy showed that increasing the amount of F_4SKL increased the amount of MWNTs that could be dispersed. This indicates that more interactions between F_4SKL and MWNTs can occur supporting the hypothesis that π-interaction similar to those in association of lignin are responsible for the dispersion of MWNTs.

The stability of the electrospinning process was dramatically affected by the MWNT dispersion; the better the dispersion, the better the spinning. Fibre morphology depended on the thermal processing and addition of MWNTs. Carbon fibres containing MWNTs became curly as compared to the corresponding as-spun and thermostabilized fibres. This could due to differing shrinkage amounts between F_4SKL and MWNTs at higher temperature. The change in fibre morphology affected the performance of the fibres, specifically the tensile modulus. TEM images revealed poor interaction between F_4SKL and MWNTs, as observed by MWNT pullout, which indicates the load transfer to the MWNTs was not successful. XRD and Raman spectroscopy revealed that the lignin based carbon fibres were still amorphous therefore decreasing the intrinsic mechanical performance. The addition of MWNTs did not improve the graphitization of the lignin based carbon fibres which could imply that the interaction between lignin and MWNTs was not strong enough to meet the basic reinforcement requirement for reinforcing composites. Therefore, the mechanical properties did not improve with incorporating MWNTs. The electrical conductivity did not increase with adding MWNTs which could be due to the aforementioned morphology issues. As well the MWNTs used in this study may be more semiconductive than metallic and the loading used in this study may be too low such that the percolation threshold has not met.

5 Future Work

A correlation between dispersion of MWNT suspension and G band intensity was observed in this work and possible mechanisms were proposed. The work implies that Raman spectroscopy is an efficient method to characterize dispersion of MWNTs. The reason for D band shifting to higher wave number and becoming broader in aggregated suspension is still unclear. As such, further Raman spectroscopy studies are needed to confirm the factors affecting the D band and G band. Rheology analysis could be another potential method to determine dispersion. Isolated MWNTs can lead to physical contacts between un-entangled particles to form networks (*165*) such that the viscosity of the suspension increases. An efficient method to quantify dispersion of MWNTs in suspensions is required for further applications, such as nano-composites.

The proposed method of incorporating MWNTs into lignin based fibres to improve mechanical properties of the fibres was not significant and the strength and modulus decreased with higher MWNT loading. Although dispersion of MWNTs in suspensions was studied, the interfacial interaction between MWNTs and F_4SKL is another fundamental issue pertaining to reinforcement of composites, and is a topic which requires further investigation. Failure of load transfer to MWNTs could lead to defects and heterogeneity in fibres decreasing the performance of mechanical properties. Further studies are needed to investigate interfacial bonding and techniques to form stronger interactions between MWNTs and lignin. One possibility is the modification of MWNTs via attaching lignin molecules on the surface of MWNTs to increase the attraction between lignin and MWNTs. Another possibility could be that the MWNTs used in this study were low quality such that it has less ability to enhance fibre properties.

Non-oxidized MWNTs could have fewer defects and possess a better quality than oxidized MWNTs. Although SWNTs are harder to disperse, it may be a desirable option since it is well know that SWNTs possess outstanding mechanical and electrical conductivity, superior to MWNTs.

The mechanical properties of lignin based carbon fibre produced in this study still have to be improved to compete with PAN-based fibre. Increasing the temperature during carbonization could lead to a better degree of graphitization. A more ordered carbon structure can transfer the stress to MWNTs and increase the mechanical properties and could also affect the performance of electrical conductivity. Although lignin based carbon fibres exhibited amorphous carbon structure in XRD, they still possess lower resistivity than PAN based carbon fibres under the same conditions. This implies the development of other novel applications of electrospun lignin fibres.

References

1. Ralph, J., Lundquist, K., Brunow, G., Lu, F., Kim, H., Schatz, P. F., Marita, J. M., Hatfield, R. D., Ralph, S. A., Christensen, J. H., and Boerjan, W. (2004) Lignins: Natural polymers from oxidative coupling of 4-hydroxyphenylpropanoids, *Phytochemistry Reviews 3*.
2. Donaldson, L. A. (2001) Lignification and lignin topochemistry - an ultrastructural view, *Phytochemistry 57*.
3. Donald, D. (2010) Overview, In *Lignin and Lignans*, pp 1-10, CRC Press.
4. Kubo, S., and Kadla, J., F. (2007) Carbon Fibers from Lignin-Recyclable Plastic Blends, In *Encyclopedia of Chemical Processing*, pp 317-331, Taylor & Francis.
5. Boerjan, W., Ralph, J., and Baucher, M. (2003) Lignin biosynthesis, *Annual Review Of Plant Biology 54*, 519-546.
6. Cathala, B., Chabbert, B., Joly, C., Dole, P., and Monties, B. (2001) Synthesis, characterisation and water sorption properties of pectin-dehydrogenation polymer (lignin model compound) complex, *Phytochemistry 56*, 195-202.
7. Santos, R. B., Capanema, E. A., Balakshin, M. Y., Chang, H.-m., and Jameel, H. (2012) Lignin Structural Variation in Hardwood Species, *J. Agric. Food. Chem. 60*, 4923-4930.
8. Capanema, E. A., Balakshin, M. Y., and Kadla, J. F. (2004) A Comprehensive Approach for Quantitative Lignin Characterization by NMR Spectroscopy, *J. Agric. Food. Chem. 52*, 1850-1860.
9. Donaldson, L. A., (Ed.) (2001) *Lignin and Lignans*.
10. Zakzeski, J., Bruijnincx, P. C. A., Jongerius, A. L., and Weckhuysen, B. M. (2010) The Catalytic Valorization of Lignin for the Production of Renewable Chemicals, *Chem. Rev. 110*, 3552-3599.
11. Stenius, P. (2000) Papermaking Science and Technology Series - Forest Products Chemistry, 350.
12. Johansson, A., Aaltonen, O., and Ylinen, P. (1987) Organosolv pulping — methods and pulp properties, *Biomass 13*, 45-65.
13. Gellerstedt, G., Sjoholm, E., and Brodin, I. (2010) The wood-based biorefinery: a source of carbon fiber?, *Open Agr. J. 4*, 119-124.
14. Gosselink, R. J. A., de Jong, E., Guran, B., and Abächerli, A. (2004) Co-ordination network for lignin—standardisation, production and applications adapted to market requirements (EUROLIGNIN), *Ind. Crops Prod. 20*, 121-129.
15. Lora, J. H., and Glasser, W. G. (2002) Recent Industrial Applications of Lignin: A Sustainable Alternative to Nonrenewable Materials, *J. Polym. Environ. 10*, 39-48.
16. Gargulak, J. D., and Lebo, S. E. (1999) Commercial Use of Lignin-Based Materials, In *Lignin: Historical, Biological, and Materials Perspectives*, pp 304-320, American Chemical Society.

17. Joseph, L. M., and Aminul, I. (1999) Lignin Chemistry, Technology, and Utilization: A Brief History, In *Lignin: Historical, Biological, and Materials Perspectives*, pp 2-99, American Chemical Society.
18. Haggenmueller, R., Rahatekar, S. S., Fagan, J. A., Chun, J., Becker, M. L., Naik, R. R., Krauss, T., Carlson, L., Kadla, J. F., Trulove, P. C., Fox, D. F., DeLong, H. C., Fang, Z., Kelley, S. O., and Gilman, J. W. (2008) Comparison of the Quality of Aqueous Dispersions of Single-Wall Carbon Nanotubes Using Surfactants and Biomolecules, *Langmuir 24*, 5070-5078.
19. Milczarek, G. (2010) Kraft lignin as dispersing agent for carbon nanotubes, *J. Electroanal. Chem. 638*, 178-181.
20. Kadla, J. F., Kubo, S., Venditti, R. A., Gilbert, R. D., Compere, A. L., and Griffith, W. (2002) Lignin-based carbon fibers for composite fiber applications, *Carbon 40*, 2913-2920.
21. Qin, W., and Kadla, J. F. (2011) Effect of Organoclay Reinforcement on Lignin-Based Carbon Fibers, *Ind. Eng. Chem. Res. 50*, 12548-12555.
22. Compere, A. L., and Griffith, W. L. (2009) Preparation and Analysis of Biomass Lignins, In *Biofuels*, pp 185-212.
23. Kubo, S., and Kadla, J. F. (2005) Lignin-based Carbon Fibers: Effect of Synthetic Polymer Blending on Fiber Properties, *J. Polym. Environ. 13*, 97-105.
24. Bahl, O. P., Shen, Z., Lavin, J. G., and Ross, R. A. (1998) *Carbon Fibers*, Marcel. Dekker New York, NY.
25. Bayat, M., Yang, H., and Ko, F. (2011) Electromagnetic properties of electrospun Fe3O4/carbon composite nanofibers, *Polymer 52*, 1645-1653.
26. Park, S. H., Kim, C., and Yang, K. S. (2004) Preparation of carbonized fiber web from electrospinning of isotropic pitch, *Synth. Met. 143*, 175-179.
27. D.D, E. (1998) The effect of processing on the structure and properties of carbon fibers, *Carbon 36*, 345-362.
28. Minus, M., and Kumar, S. (2005) The processing, properties, and structure of carbon fibers, *JOM 57*, 52-58.
29. Morgan, P. (2005) Precursors for Carbon Fiber Manufacture, In *Carbon Fibers and Their Composites*, pp 121-184, CRC Press.
30. Chae, H. G., Choi, Y. H., Minus, M. L., and Kumar, S. (2009) Carbon nanotube reinforced small diameter polyacrylonitrile based carbon fiber, *Compos. Sci. Technol. 69*, 406-413.
31. Frank, E., Hermanutz, F., and Buchmeiser, M. R. (2012) Carbon Fibers: Precursors, Manufacturing, and Properties, *Macromolecular Materials and Engineering 297*, 493-501.
32. Otani, S. (1981) Carbonaceous Mesophase and Carbon Fibers, *Mol. Cryst. Liq. Cryst. 63*, 249-263.
33. Otani, S., Fukuoka, Y., Igarashi, B., and Sasaki, K. (1969) Method for producing carbonized lignin

fiber., *US Pat. 3461082*.

34. Tomizuka, I., and Johnson, D. J. (1978) Microvoids in pitch-based and lignin-based carbon fibres as observed by X- ray small angle scattering, *Yogyo-Kyokai-Shi 86*, 186-192.
35. Sudo, K., and Shimizu, K. (1992) A new carbon fiber from lignin, *J. Appl. Polym. Sci. 44*, 127-134.
36. Sudo, K., Shimizu, K., Nakashima, N., and Yokoyama, A. (1993) A new modification method of exploded lignin for the preparation of a carbon fiber precursor, *J. Appl. Polym. Sci. 48*, 1485-1491.
37. Uraki, Y., Kubo, S., Nigo, N., Sano, Y., and Sasaya, T. (1995) Preparation of carbon-fibers from Organosolv lignin obtained by aqueous acetic-acid pulping., *Holzforschung 49*, 343-350.
38. Kubo, S., Uraki, Y., and Sano, Y. (1998) Preparation of carbon fibers from softwood lignin by atmospheric acetic acid pulping, *Carbon 36*, 1119-1124.
39. Baker, F. S., Gallego, N. C., and Baker, D. A. (2010) Utilization of sustainable resource materials for production of carbon fiber materials for structural and energy efficiency applications, In *SAMPE Conference Proceedings*, St. Simons Island, Georgia.
40. Hamad, W. (2006) On the Development and Applications of Cellulosic Nanofibrillar and Nanocrystalline Materials, *Can. J. Chem. Eng. 84*, 513-519.
41. Deitzel, J. M., Kleinmeyer, J., Harris, D., and Beck Tan, N. C. (2001) The effect of processing variables on the morphology of electrospun nanofibers and textiles, *Polymer 42*, 261-272.
42. Wan, L.-S., Ke, B.-B., Wu, J., and Xu, Z.-K. (2007) Catalase Immobilization on Electrospun Nanofibers: Effects of Porphyrin Pendants and Carbon Nanotubes, *J. Phys. Chem. C 111*, 14091-14097.
43. Dallmeyer, I., Ko, F., and Kadla, J. F. (2010) Electrospinning of Technical Lignins for the Production of Fibrous Networks, *J. Wood Chem. Technol. 30*, 315-329.
44. Norris, I. D., Shaker, M. M., Ko, F. K., and MacDiarmid, A. G. (2000) Electrostatic fabrication of ultrafine conducting fibers: polyaniline/polyethylene oxide blends, *Synth. Met. 114*, 109-114.
45. Gupta, P., Elkins, C., Long, T. E., and Wilkes, G. L. (2005) Electrospinning of linear homopolymers of poly(methyl methacrylate): exploring relationships between fiber formation, viscosity, molecular weight and concentration in a good solvent, *Polymer 46*, 4799-4810.
46. Ko, F., Gogotsi, Y., Ali, A., Naguib, N., Ye, H., Yang, G. L., Li, C., and Willis, P. (2003) Electrospinning of Continuous Carbon Nanotube-Filled Nanofiber Yarns, *Adv. Mater. 15*, 1161-1165.
47. Matthews, J. A., Wnek, G. E., Simpson, D. G., and Bowlin, G. L. (2002) Electrospinning of Collagen Nanofibers, *Biomacromolecules 3*, 232-238.
48. Li, M., Mondrinos, M. J., Gandhi, M. R., Ko, F. K., Weiss, A. S., and Lelkes, P. I. (2005) Electrospun protein fibers as matrices for tissue engineering, *Biomaterials 26*, 5999-6008.
49. Formhals, A. (1934) US Patent #1,975,504.

50. Taylor, G. (1969) Electrically Driven Jets, *Proceedings of the Royal Society of London. A. Mathematical and Physical Sciences 313*, 453-475.

51. Baumgarten, P. K. (1971) Electrostatic spinning of acrylic microfibers, *J. Colloid Interface Sci. 36*, 71-79.

52. Larrondo, L., and St. John Manley, R. (1981) Electrostatic fiber spinning from polymer melts. I. Experimental observations on fiber formation and properties, *Journal of Polymer Science: Polymer Physics Edition 19*, 909-920.

53. Doshi, J., and Reneker, D. H. (1993) Electrospinning process and applications of electrospun fibers, In *Industry Applications Society Annual Meeting, 1993., Conference Record of the 1993 IEEE*, pp 1698-1703 vol.1693.

54. Reneker, and Iksoo Chun, D. (1996) Nanometre diameter fibres of polymer, produced by electrospinning, *Nanotechnology 7*, 216.

55. Ayutsede, J., Gandhi, M., Sukigara, S., Micklus, M., Chen, H.-E., and Ko, F. (2005) Regeneration of Bombyx mori silk by electrospinning. Part 3: characterization of electrospun nonwoven mat, *Polymer 46*, 1625-1634.

56. Tsai, P. P., Schreuder-Gibson, H., and Gibson, P. (2002) Different electrostatic methods for making electret filters, *J. Electrost. 54*, 333-341.

57. Pham, Q., Sharma, U., and Mikos, A. G. (2006) Electrospinning of polymeric nanofibers for tissue engineering applications: a review, *Tissue Eng 12*, 1197-1211.

58. Li, C., Vepari, C., Jin, H.-J., Kim, H. J., and Kaplan, D. L. (2006) Electrospun silk-BMP-2 scaffolds for bone tissue engineering, *Biomaterials 27*, 3115-3124.

59. Wang, M., Singh, H., Hatton, T. A., and Rutledge, G. C. (2004) Field-responsive superparamagnetic composite nanofibers by electrospinning, *Polymer 45*, 5505-5514.

60. Viet, A. L., Reddy, M. V., Jose, R., Chowdari, B. V. R., and Ramakrishna, S. (2009) Nanostructured Nb2O5 Polymorphs by Electrospinning for Rechargeable Lithium Batteries, *J. Phys. Chem. C 114*, 664-671.

61. Khil, M.-S., Cha, D.-I., Kim, H.-Y., Kim, I.-S., and Bhattarai, N. (2003) Electrospun nanofibrous polyurethane membrane as wound dressing, *Journal of Biomedical Materials Research Part B: Applied Biomaterials 67B*, 675-679.

62. Chen, J.-P., Chang, G.-Y., and Chen, J.-K. (2008) Electrospun collagen/chitosan nanofibrous membrane as wound dressing, *Colloids and Surfaces A: Physicochemical and Engineering Aspects 313–314*, 183-188.

63. Zhang, Y., He, X., Li, J., Miao, Z., and Huang, F. (2008) Fabrication and ethanol-sensing properties of micro gas sensor based on electrospun SnO2 nanofibers, *Sensors and Actuators B: Chemical 132*, 67-73.

64. Ding, B., Wang, M., Yu, J. Y., and Sun, G. (2009) Gas sensors based on electrospun nanofibers,

Sensors 9.

65. Burger, C., Hsiao, B. S., and Benjamin, C. (2006) Nanofibrous materials and their applications, *Annu. Rev. Mater. Res. 36*.
66. Huang, Z.-M., Zhang, Y. Z., Kotaki, M., and Ramakrishna, S. (2003) A review on polymer nanofibers by electrospinning and their applications in nanocomposites, *Compos. Sci. Technol. 63*, 2223-2253.
67. Rutledge, G., and Fridrikh, S. (2007) Formation of fibers by electrospinning, *Adv Drug Deliv Rev 59*, 1384-1391.
68. Baji, A., Mai, Y.-W., Wong, S.-C., Abtahi, M., and Chen, P. (2010) Electrospinning of polymer nanofibers: Effects on oriented morphology, structures and tensile properties, *Compos. Sci. Technol. 70*, 703-718.
69. Kakade, M. V., Givens, S., Gardner, K., Lee, K. H., Chase, D. B., and Rabolt, J. F. (2007) Electric Field Induced Orientation of Polymer Chains in Macroscopically Aligned Electrospun Polymer Nanofibers, *J. Am. Chem. Soc. 129*, 2777-2782.
70. Fridrikh, S. V., Yu, J. H., Brenner, M. P., and Rutledge, G. C. (2003) Controlling the Fiber Diameter during Electrospinning, *Phys. Rev. Lett. 90*, 144502.
71. Shin, Y. M., Hohman, M. M., Brenner, M. P., and Rutledge, G. C. (2001) Experimental characterization of electrospinning: the electrically forced jet and instabilities, *Polymer 42*, 09955-09967.
72. Reneker, D. H., and Yarin, A. L. (2008) Electrospinning jets and polymer nanofibers, *Polymer 49*, 2387-2425.
73. Doshi, J., and Reneker, D. H. (1995) Electrospinning process and applications of electrospun fibers, *J. Electrost. 35*, 151-160.
74. Demir, M. M., Yilgor, I., Yilgor, E., and Erman, B. (2002) Electrospinning of polyurethane fibers, *Polymer 43*, 3303-3309.
75. Tagawa, T., and Miyata, T. (1997) Size effect on tensile strength of carbon fibers, *Mater. Sci. Eng. 238*, 336-342.
76. Buchko, C. J., Chen, L. C., Shen, Y., and Martin, D. C. (1999) Processing and microstructural characterization of porous biocompatible protein polymer thin films, *Polymer 40*.
77. Fong, H., Chun, I., and Reneker, D. H. (1999) Beaded nanofibers formed during electrospinning, *Polymer 40*, 4585-4592.
78. McKee, M. G., Wilkes, G. L., Colby, R. H., and Long, T. E. (2004) Correlations of Solution Rheology with Electrospun Fiber Formation of Linear and Branched Polyesters, *Macromolecules 37*, 1760-1767.
79. Wannatong, L., Sirivat, A., and Supaphol, P. (2004) Effects of solvents on electrospun polymeric fibers: preliminary study on polystyrene, *Polym. Int. 53*, 1851-1859.

80. Frenot, A., and Chronakis, I. S. (2003) Polymer nanofibers assembled by electrospinning, *Current Opinion in Colloid & Interface Science 8*, 64-75.
81. Zhang, C., Yuan, X., Wu, L., Han, Y., and Sheng, J. (2005) Study on morphology of electrospun poly(vinyl alcohol) mats, *Eur. Polym. J. 41*, 423-432.
82. Gandhi, M., Yang, H., Shor, L., and Ko, F. (2009) Post-spinning modification of electrospun nanofiber nanocomposite from Bombyx mori silk and carbon nanotubes, *Polymer 50*, 1918-1924.
83. Liao, C.-C., Wang, C.-C., Chen, C.-Y., and Lai, W.-J. (2011) Stretching-induced orientation of polyacrylonitrile nanofibers by an electrically rotating viscoelastic jet for improving the mechanical properties, *Polymer 52*, 2263-2275.
84. Wu, S., Zhang, F., Hou, X., and Yang, X. (2008) Stretching-induced Orientation for Improving the Mechanical Properties of Electrospun Polyacrylonitrile Nanofiber Sheet, *Advanced Materials Research 47-50*.
85. Ohgo, K., Zhao, C., Kobayashi, M., and Asakura, T. (2003) Preparation of non-woven nanofibers of Bombyx mori silk, Samia cynthia ricini silk and recombinant hybrid silk with electrospinning method, *Polymer 44*, 841-846.
86. Huang, Z.-M., Zhang, Y. Z., Ramakrishna, S., and Lim, C. T. (2004) Electrospinning and mechanical characterization of gelatin nanofibers, *Polymer 45*, 5361-5368.
87. Huang, L., Nagapudi, K., P.Apkarian, R., and Chaikof, E. L. (2001) Engineered collagenPEO nanofibers and fabrics, *Journal of Biomaterials Science, Polymer Edition 12*, 979-993.
88. Huang, L., McMillan, R. A., Apkarian, R. P., Pourdeyhimi, B., Conticello, V. P., and Chaikof, E. L. (2000) Generation of Synthetic Elastin-Mimetic Small Diameter Fibers and Fiber Networks, *Macromolecules 33*, 2989-2997.
89. Pedicini, A., and Farris, R. J. (2003) Mechanical behavior of electrospun polyurethane, *Polymer 44*, 6857-6862.
90. Hou, H., Ge, J. J., Zeng, J., Li, Q., Reneker, D. H., Greiner, A., and Cheng, S. Z. D. (2005) Electrospun Polyacrylonitrile Nanofibers Containing a High Concentration of Well-Aligned Multiwall Carbon Nanotubes, *Chem. Mater. 17*, 967-973.
91. Xuyen, N. T., Ra, E. J., Geng, H.-Z., Kim, K. K., An, K. H., and Lee, Y. H. (2007) Enhancement of Conductivity by Diameter Control of Polyimide-Based Electrospun Carbon Nanofibers, *J. Phys. Chem. B 111*, 11350-11353.
92. Wang, Y., Serrano, S., and Santiago-Aviles, J. J. (2002) Conductivity measurement of electrospun PAN-based carbon nanofiber, *J. Mater. Sci. Lett. 21*, 1055-1057.
93. Panapoy, M., Dankeaw, A., and Ksapabutr, B. (2008) Electrical Conductivity of PAN-based Carbon Nanofibers Prepared by Electrospinning Method, *Thammasat Int. J. Sc. Tech. 13*, 11-17.
94. Yang, K. S., Edie, D. D., Lim, D. Y., Kim, Y. M., and Choi, Y. O. (2003) Preparation of carbon fiber web from electrostatic spinning of PMDA-ODA poly(amic acid) solution, *Carbon 41*,

2039-2046.

95. Sinha Ray, S., and Okamoto, M. (2003) Polymer/layered silicate nanocomposites: a review from preparation to processing, *Prog. Polym. Sci. 28*, 1539-1641.

96. Kojima, Y., Usuki, A., Kawasumi, M., Okada, A., Kurauchi, T., and Kamigaito, O. (1993) Synthesis of nylon 6–clay hybrid by montmorillonite intercalated with ϵ-caprolactam, *J. Polym. Sci., Part A: Polym. Chem. 31*, 983-986.

97. Fong, H., Liu, W., Wang, C.-S., and Vaia, R. A. (2002) Generation of electrospun fibers of nylon 6 and nylon 6-montmorillonite nanocomposite, *Polymer 43*, 775-780.

98. Eichhorn, S., Dufresne, A., Aranguren, M., Marcovich, N., Capadona, J., Rowan, S., Weder, C., Thielemans, W., Roman, M., Renneckar, S., Gindl, W., Veigel, S., Keckes, J., Yano, H., Abe, K., Nogi, M., Nakagaito, A., Mangalam, A., Simonsen, J., Benight, A., Bismarck, A., Berglund, L., and Peijs, T. (2010) Review: current international research into cellulose nanofibres and nanocomposites, *Journal of Materials Science 45*, 1-33.

99. Azizi Samir, M. A. S., Alloin, F., and Dufresne, A. (2005) Review of Recent Research into Cellulosic Whiskers, Their Properties and Their Application in Nanocomposite Field, *Biomacromolecules 6*, 612-626.

100. Dong, H., Strawhecker, K., E. , Snyder, J. F., Orlicki, J. A., Reiner, R. S., and Rudie, A. W. (2012) Cellulose nanocrystals as a reinforcing material for electrospun poly(methyl methacrylate) fibers: Formation, properties and nanomechanical characterization, *Carbohydr Polym 87*, 2488-2495.

101. Lu, P., and Hsieh, Y.-L. (2010) Multiwalled Carbon Nanotube (MWCNT) Reinforced Cellulose Fibers by Electrospinning, *ACS Appl. Mater. Interfaces 2*, 2413-2420.

102. Almecija, D., Blond, D., Sader, J. E., Coleman, J. N., and Boland, J. J. (2009) Mechanical properties of individual electrospun polymer-nanotube composite nanofibers, *Carbon 47*, 2253-2258.

103. Ge, J. J., Hou, H., Li, Q., Graham, M. J., Greiner, A., Reneker, D. H., Harris, F. W., and Cheng, S. Z. D. (2004) Assembly of Well-Aligned Multiwalled Carbon Nanotubes in Confined Polyacrylonitrile Environments: Electrospun Composite Nanofiber Sheets, *J. Am. Chem. Soc. 126*, 15754-15761.

104. Ra, E. J., An, K. H., Kim, K. K., Jeong, S. Y., and Lee, Y. H. (2005) Anisotropic electrical conductivity of MWCNT/PAN nanofiber paper, *Chem. Phys. Lett. 413*, 188-193.

105. Regev, O., ElKati, P. N. B., Loos, J., and Koning, C. E. (2004) Preparation of Conductive Nanotube–Polymer Composites Using Latex Technology, *Adv. Mater. 16*, 248-251.

106. Bandyopadhyaya, R., Nativ-Roth, E., Regev, O., and Yerushalmi-Rozen, R. (2001) Stabilization of Individual Carbon Nanotubes in Aqueous Solutions, *Nano Lett. 2*, 25-28.

107. Breuer, O., and Sundararaj, U. (2004) Big returns from small fibers: A review of polymer/carbon nanotube composites, *Polym. Compos. 25*, 630-645.

108. Liew, K. M., Wong, C. H., and Tan, M. J. (2005) Buckling properties of carbon nanotube bundles, *Appl. Phys. Lett. 87*, 041901-041903.
109. Saito, R., Dresselhaus, G., and Dresselhaus, M. S. (1998) Physical Properties Of Carbon Nanotubes, World Scientific Publishing and Imperial College Press.
110. Schönenberger, C., and Forro, L. (2000) Physics of Multiwall Carbon Nanotubes, *Physics World 13*.
111. Iijima, S. (2002) Carbon nanotubes: past, present, and future, *Physica B: Condensed Matter 323*, 1-5.
112. Iijima, S. (1991) Helical microtubules of graphitic carbon, *Nature 354*, 56-58.
113. Ebbesen, T. W., and Ajayan, P. M. (1992) Large-scale synthesis of carbon nanotubes, *Nature 358*, 220-222.
114. Bronikowski, M. J., Willis, P. A., Colbert, D. T., Smith, K. A., and Smalley, R. E. (2001) Gas-phase production of carbon single-walled nanotubes from carbon monoxide via the HiPco process: A parametric study, *Journal of Vacuum Science & Technology A 19*, 1800-1805.
115. José-Yacamán, M., Miki-Yoshida, M., Rendón, L., and Santiesteban, J. G. (1993) Catalytic growth of carbon microtubules with fullerene structure, *Appl. Phys. Lett. 62*.
116. Bethune, D. S., Kiang, C. H., Vries, M. S. D., Gorman, G., Savoy, R., Vazquez, J., and Beyers, R. (1993) Cobalt-catalysed growth of carbon nanotubes with single-atomic-layer walls, *Nature 363*, 605-607.
117. Yu, M.-F., Lourie, O., Dyer, M. J., Moloni, K., Kelly, T. F., and Ruoff, R. S. (2000) Strength and Breaking Mechanism of Multiwalled Carbon Nanotubes Under Tensile Load, *Science 287*, 637-640.
118. Hong, S., and Myung, S. (2007) Nanotube Electronics: A flexible approach to mobility, *Nat Nano 2*, 207-208.
119. Cooper, C. A., Ravich, D., Lips, D., Mayer, J., and Wagner, H. D. (2002) Distribution and alignment of carbon nanotubes and nanofibrils in a polymer matrix, *Compos. Sci. Technol. 62*, 1105-1112.
120. Hadjiev, V. G., Iliev, M. N., Arepalli, S., Nikolaev, P., and Files, B. S. (2001) Raman scattering test of single-wall carbon nanotube composites, *Appl. Phys. Lett. 78*, 3193-3195.
121. Li, F., Cheng, H. M., Bai, S., Su, G., and Dresselhaus, M. S. (2000) Tensile strength of single-walled carbon nanotubes directly measured from their macroscopic ropes, *Appl. Phys. Lett. 77*, 3161.
122. Bower, C., Rosen, R., Jin, L., Han, J., and Zhou, O. (1999) Deformation of carbon nanotubes in nanotube--polymer composites, *Appl. Phys. Lett. 74*, 3317-3319.
123. Lerner, E. J. (1999) Putting Nanotubes to Work, *The Industrial Physicist*.
124. Lau, A. K.-T., and Hui, D. (2002) The revolutionary creation of new advanced materials—carbon

nanotube composites, *Composites Part B: Engineering 33*, 263-277.

125. Coleman, J. N., Khan, U., Blau, W. J., and Gun'ko, Y. K. (2006) Small but strong: A review of the mechanical properties of carbon nanotube–polymer composites, *Carbon 44*, 1624-1652.
126. Vaisman, L., Wagner, H. D., and Marom, G. (2006) The role of surfactants in dispersion of carbon nanotubes, *Advances in Colloid and Interface Science 128-130*, 37-46.
127. Jung, D.-H., Koan Ko, Y., and Jung, H.-T. (2004) Aggregation behavior of chemically attached poly(ethylene glycol) to single-walled carbon nanotubes (SWNTs) ropes, *Mater. Sci. Eng., Proc, Conf. 24*, 117-121.
128. Saito, T., Matsushige, K., and Tanaka, K. (2002) Chemical treatment and modification of multi-walled carbon nanotubes, *Physica B: Condensed Matter 323*, 280-283.
129. Lee, G.-W., and Kumar, S. (2005) Dispersion of Nitric Acid-Treated SWNTs in Organic Solvents and Solvent Mixtures, *J. Phys. Chem. B 109*, 17128-17133.
130. Ausman, K. D., Piner, R., Lourie, O., Ruoff, R. S., and Korobov, M. (2000) Organic Solvent Dispersions of Single-Walled Carbon Nanotubes: Toward Solutions of Pristine Nanotubes, *J. Phys. Chem. B 104*, 8911-8915.
131. Lu, K. L., Lago, R. M., Chen, Y. K., Green, M. L. H., Harris, P. J. F., and Tsang, S. C. (1996) Mechanical damage of carbon nanotubes by ultrasound, *Carbon 34*, 814-816.
132. Vaisman, L., Wagner, H. D., and Marom, G. (2006) The role of surfactants in dispersion of carbon nanotubes, *Adv. Colloid Interface Sci. 128-130*, 37-46.
133. Star, A., Liu, Y., Grant, K., Ridvan, L., Stoddart, J. F., Steuerman, D. W., Diehl, M. R., Boukai, A., and Heath, J. R. (2003) Noncovalent Side-Wall Functionalization of Single-Walled Carbon Nanotubes, *Macromolecules 36*, 553-560.
134. Yurekli, K., Mitchell, C. A., and Krishnamoorti, R. (2004) Small-Angle Neutron Scattering from Surfactant-Assisted Aqueous Dispersions of Carbon Nanotubes, *J. Am. Chem. Soc. 126*, 9902-9903.
135. Chen, R. J., Zhang, Y., Wang, D., and Dai, H. (2001) Noncovalent Sidewall Functionalization of Single-Walled Carbon Nanotubes for Protein Immobilization, *J. Am. Chem. Soc. 123*, 3838-3839.
136. Sinani, V. A., Gheith, M. K., Yaroslavov, A. A., Rakhnyanskaya, A. A., Sun, K., Mamedov, A. A., Wicksted, J. P., and Kotov, N. A. (2005) Aqueous Dispersions of Single-wall and Multiwall Carbon Nanotubes with Designed Amphiphilic Polycations, *J. Am. Chem. Soc. 127*, 3463-3472.
137. Gutierrez, F., Rubianes, M. D., and Rivas, G. A. (2012) Dispersion of multi-wall carbon nanotubes in glucose oxidase: Characterization and analytical applications for glucose biosensing, *Sens. Actuators, B 161*, 191-197.
138. Garg, A., and Sinnott, S. B. (1998) Effect of chemical functionalization on the mechanical properties of carbon nanotubes, *Chemical Physics Letters 295*, 273-278.
139. Rasheed, A., Dadmun, M. D., Ivanov, I., Britt, P. F., and Geohegan, D. B. (2006) Improving

Dispersion of Single-Walled Carbon Nanotubes in a Polymer Matrix Using Specific Interactions, *Chem. Mater. 18*, 3513-3522.

140. Adsul, M. G., Rey, D. A., and Gokhale, D. V. (2011) Combined strategy for the dispersion/dissolution of single walled carbon nanotubes and cellulose in water, *J. Mater. Chem. 21*, 2054-2056.

141. Ikeda, A., Hamano, T., Hayashi, K., and Kikuchi, J.-i. (2006) Water-Solubilization of Nucleotides-Coated Single-Walled Carbon Nanotubes Using a High-Speed Vibration Milling Technique, *Org. Lett. 8*, 1153-1156.

142. Athalin, H., and Lefrant, S. (2005) A correlated method for quantifying mixed and dispersed carbon nanotubes: analysis of the Raman band intensities and evidence of wavenumber shift, *Journal of Raman Spectroscopy 36*, 400-408.

143. Itkis, M. E., Perea, D. E., Jung, R., Niyogi, S., and Haddon, R. C. (2005) Comparison of Analytical Techniques for Purity Evaluation of Single-Walled Carbon Nanotubes, *J. Am. Chem. Soc. 127*, 3439-3448.

144. Wang, Y., Serrano, S., and Santiago-Avilés, J. J. (2003) Raman characterization of carbon nanofibers prepared using electrospinning, *Synth. Met. 138*, 423-427.

145. Ferrari, A. C., and Robertson, J. (2000) Interpretation of Raman spectra of disordered and amorphous carbon, *Phys. Rev. B 61*.

146. Ferrari, A., and Robertson, J. (2001) Resonant Raman spectroscopy of disordered, amorphous, and diamondlike carbon, *Phys. Rev. B 64*.

147. Strano, M. S., Moore, V. C., Miller, M. K., Allen, M. J., Haroz, E. H., Kittrell, C., Hauge, R. H., and Smalley, R. E. (2003) The role of surfactant adsorption during ultrasonication in the dispersion of single-walled carbon nanotubes, *J. Nanosci. Nanotechnol. 3*, 81-86.

148. Heller, D. A., Barone, P. W., Swanson, J. P., Mayrhofer, R. M., and Strano, M. S. (2004) Using Raman Spectroscopy to Elucidate the Aggregation State of Single-Walled Carbon Nanotubes, *J. Phys. Chem. B 108*, 6905-6909.

149. Salzmann, C. G., Chu, B. T. T., Tobias, G., Llewellyn, S. A., and Green, M. L. H. (2007) Quantitative assessment of carbon nanotube dispersions by Raman spectroscopy, *Carbon 45*, 907-912.

150. Baughman, R. H., Zakhidov, A. A., and de Heer, W. A. (2002) Carbon Nanotubes--the Route Toward Applications, *Science 297*, 787-792.

151. Dror, Y., Salalha, W., Khalfin, R. L., Cohen, Y., Yarin, A. L., and Zussman, E. (2003) Carbon Nanotubes Embedded in Oriented Polymer Nanofibers by Electrospinning, *Langmuir 19*, 7012-7020.

152. Sarkanen, S., Teller, D. C., Stevens, C. R., and McCarthy, J. L. (1984) Lignin. 20. Associative interactions between kraft lignin components, *Macromolecules 17*, 2588-2597.

153. Morck, R., yoshida, H., and Kringstad, K. P. (1986) Fractronation of Kraft lignin by successive extraction with organic solvents. I. Functional groups, ^{13}C-NMR-spectra and morecular weight distributions, *Holzforschung 40*, 51-60.

154. Kubo, S., and Kadla, J. F. (2005) Hydrogen Bonding in Lignin: A Fourier Transform Infrared Model Compound Study, *Biomacromolecules 6*, 2815-2821.

155. Lindströmn, T. (1979) The colloidal behaviour of kraft lignin, *Colloid. Polym. Sci. 257*, 277-285.

156. Sarkanen, S., Teller, D. C., Hall, J., and McCarthy, J. L. (1981) Lignin. 18. Associative effects among organosolv lignin components, *Macromolecules 14*, 426-434.

157. Deng, Y., Feng, X., Zhou, M., Qian, Y., Yu, H., and Qiu, X. (2011) Investigation of Aggregation and Assembly of Alkali Lignin Using Iodine as a Probe, *Biomacromolecules 12*, 1116-1125.

158. Connors, W. J., Sarkanen, S., and McCarthy, J. L. (1980) Gel chromatography and association complexes of lignin, *Holzforschung 34*.

159. Dutta, S., and Sarkanen, S. (1990) A New Emphasis in Strategies for Developing Lignin-Based Plastics, *Materials Research Society 197*.

160. Boeriu, C. G., Bravo, D., Gosselink, R. J. A., and van Dam, J. E. G. (2004) Characterisation of structure-dependent functional properties of lignin with infrared spectroscopy, *Ind. Crops Prod. 20*, 205-218.

161. Lu, X., and Weiss, R. A. (1992) Relationship between the Glass Transition Temperature and the Interaction Parameter of Miscible Binary Polymer Blends, *Macromolecules 25*.

162. Dong, D., and Fricke, A. L. (1995) Intrinsic viscosity and the molecular weight of kraft lignin, *Polymer 36*, 2075-2078.

163. Banerjee, S., Hemraj-Benny, T., and Wong, S. S. (2005) Covalent Surface Chemistry of Single-Walled Carbon Nanotubes, *Adv. Mater. 17*, 17-29.

164. Tchoul, M. N., Ford, W. T., Lolli, G., Resasco, D. E., and Arepalli, S. (2007) Effect of Mild Nitric Acid Oxidation on Dispersability, Size, and Structure of Single-Walled Carbon Nanotubes, *Chem. Mater. 19*.

165. Hilding, J., Grulke, E. A., Zhang, Z. G., and Lockwood, F. (2003) Dispersion of Carbon Nanotubes in Liquids, *J. Dispersion Sci. Technol. 24*.

166. Li, W., Liang, C., Zhou, W., Qiu, J., Zhou, Sun, G., and Xin, Q. (2003) Preparation and Characterization of Multiwalled Carbon Nanotube-Supported Platinum for Cathode Catalysts of Direct Methanol Fuel Cells, *J. Phys. Chem. B 107*, 6292-6299.

167. Wan, Y.-Q., He, J.-H., and Yu, J.-Y. (2007) Carbon nanotube-reinforced polyacrylonitrile nanofibers by vibration-electrospinning, *Polym. Int. 56*, 1367-1370.

168. Liao, G.-Y., Zhou, X.-P., Chen, L., Zeng, X.-Y., Xie, X.-L., and Mai, Y.-W. (2012) Electrospun aligned PLLA/PCL/functionalised multiwalled carbon nanotube composite fibrous membranes and their bio/mechanical properties, *Compos. Sci. Technol. 72*, 248-255.

169. Kim, C., Yang, K. S., Kojima, M., Yoshida, K., Kim, Y. J., Kim, Y. A., and Endo, M. (2006) Fabrication of Electrospinning-Derived Carbon Nanofiber Webs for the Anode Material of Lithium-Ion Secondary Batteries, *Adv. Funct. Mater. 16*, 2393-2397.
170. Chen, I. H., Wang, C.-C., and Chen, C.-Y. (2010) Fabrication and Structural Characterization of Polyacrylonitrile and Carbon Nanofibers Containing Plasma-Modified Carbon Nanotubes by Electrospinning, *J. Phys. Chem. C 114*, 13532-13539.
171. Prilutsky, S., Zussman, E., and Cohen, Y. (2010) Carbonization of electrospun poly(acrylonitrile) nanofibers containing multiwalled carbon nanotubes observed by transmission electron microscope with in situ heating, *J. Polym. Sci., Part B: Polym. Phys. 48*, 2121-2128.
172. Prilutsky, S., Zussman, E., and Cohen, Y. (2008) The effect of embedded carbon nanotubes on the morphological evolution during the carbonization of poly(acrylonitrile) nanofibers, *Nanotechnology 19*, 9.
173. Kubo, S., and Kadla, J. F. (2008) Thermal Decomposition Study of Isolated Lignin Using Temperature Modulated TGA, *Journal of wood chemistry and technology. 28*, 106-121.
174. Coleman, J. N., Khan, U., and Gun'ko, Y. K. (2006) Mechanical Reinforcement of Polymers Using Carbon Nanotubes, *Adv. Mater. 18*, 689-706.
175. Calvert, P. (1999) Nanotube composites: A recipe for strength, *Nature 399*, 210-211.
176. Coleman, J. N., Cadek, M., Ryan, K. P., Fonseca, A., Nagy, J. B., Blau, W. J., and Ferreira, M. S. (2006) Reinforcement of polymers with carbon nanotubes. The role of an ordered polymer interfacial region. Experiment and modeling, *Polymer 47*, 8556-8561.
177. Manchado, M. A. L., Valentini, L., Biagiotti, J., and Kenny, J. M. (2005) Thermal and mechanical properties of single-walled carbon nanotubes–polypropylene composites prepared by melt processing, *Carbon 43*, 1499-1505.
178. Miao, M. (2011) Electrical conductivity of pure carbon nanotube yarns, *Carbon 49*, 3755-3761.
179. Ebbesen, T. W., Lezec, H. J., Hiura, H., Bennett, J. W., Ghaemi, H. F., and Thio, T. (1996) Electrical conductivity of individual carbon nanotubes, *Nature 382*, 54-56.
180. Teng, N. Y., Dallmeyer, I., and Kadla, J. (2012) Investigation of Correlation between Multiwalled Carbon nanotubes and Softwood Kraft Lignin (submitted), *Ind. Eng. Chem. Res.*
181. Costa, S., Borowiak-palen, E., Kruszyńska, M., Bachmatiuk, A., and Kaleńczuk, R. J. (2008) Characterization of carbon nanotubes by Raman spectroscopy, *Materials Science–Poland 26*.

Appendices

Appendix A: Spectra

^{13}C-NMR spectra of non-acetylated SKL, F_1SKL, F_2SKL, F_3SKL, $F_{1\text{-}3}$SKL, and F_4SKL

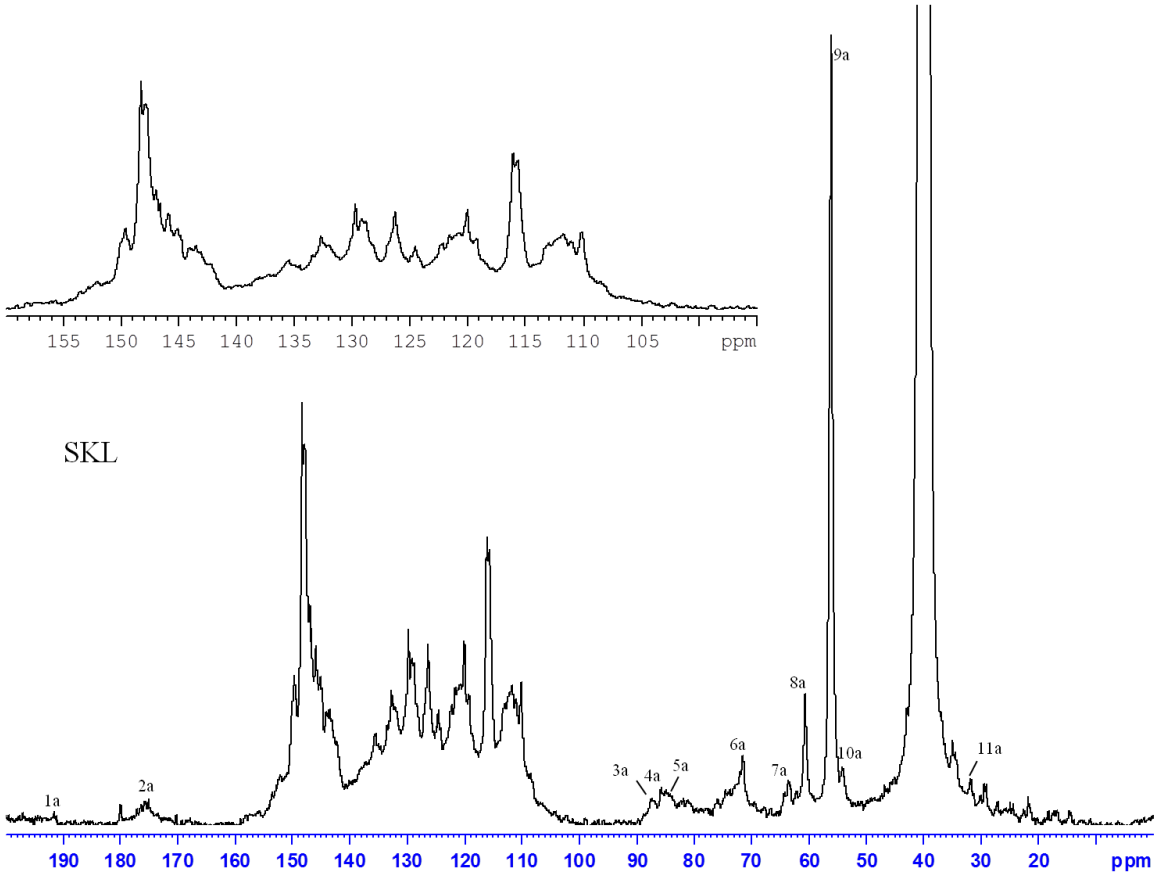

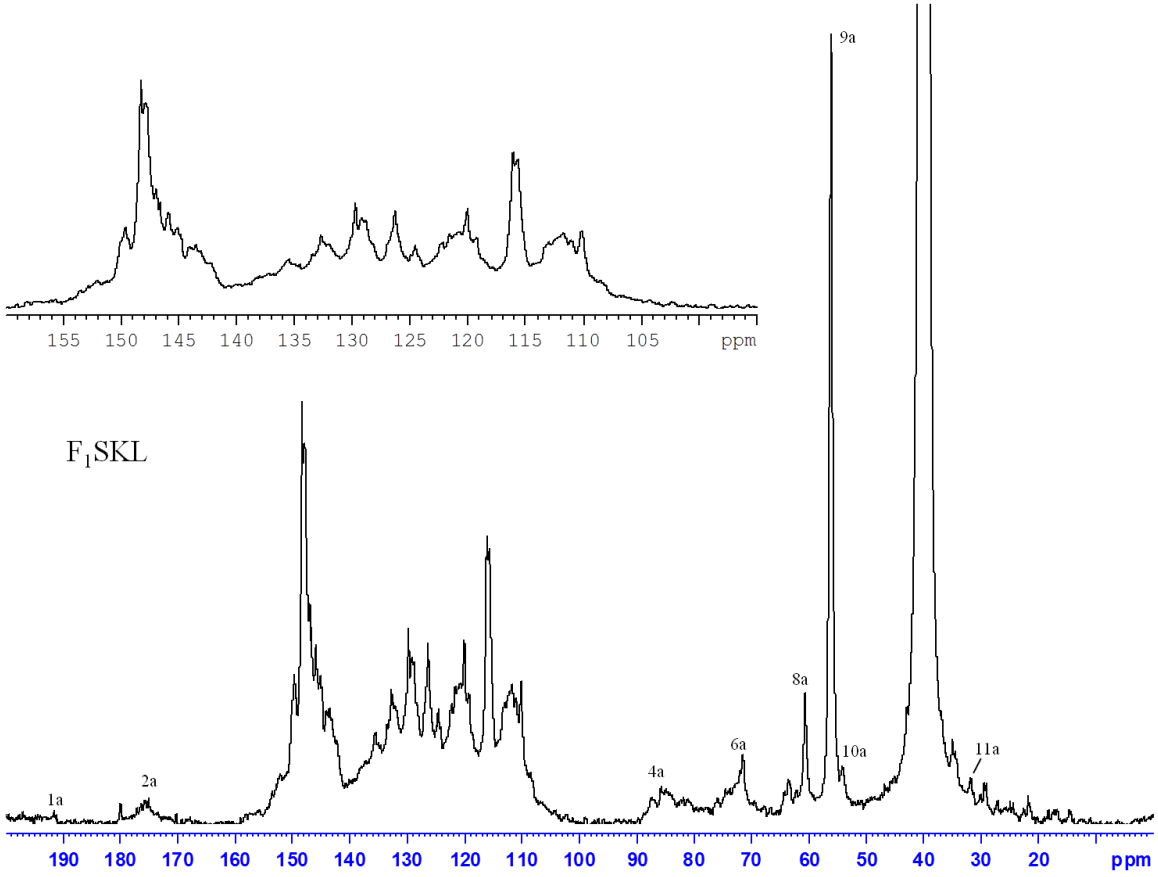
155 150 145 140 135 130 125 120 115 110 105 ppm
F1SKL
1a
2a
4a
6a
8a
9a
10a
11a
190 180 170 160 150 140 130 120 110 100 90 80 70 60 50 40 30 20 ppm

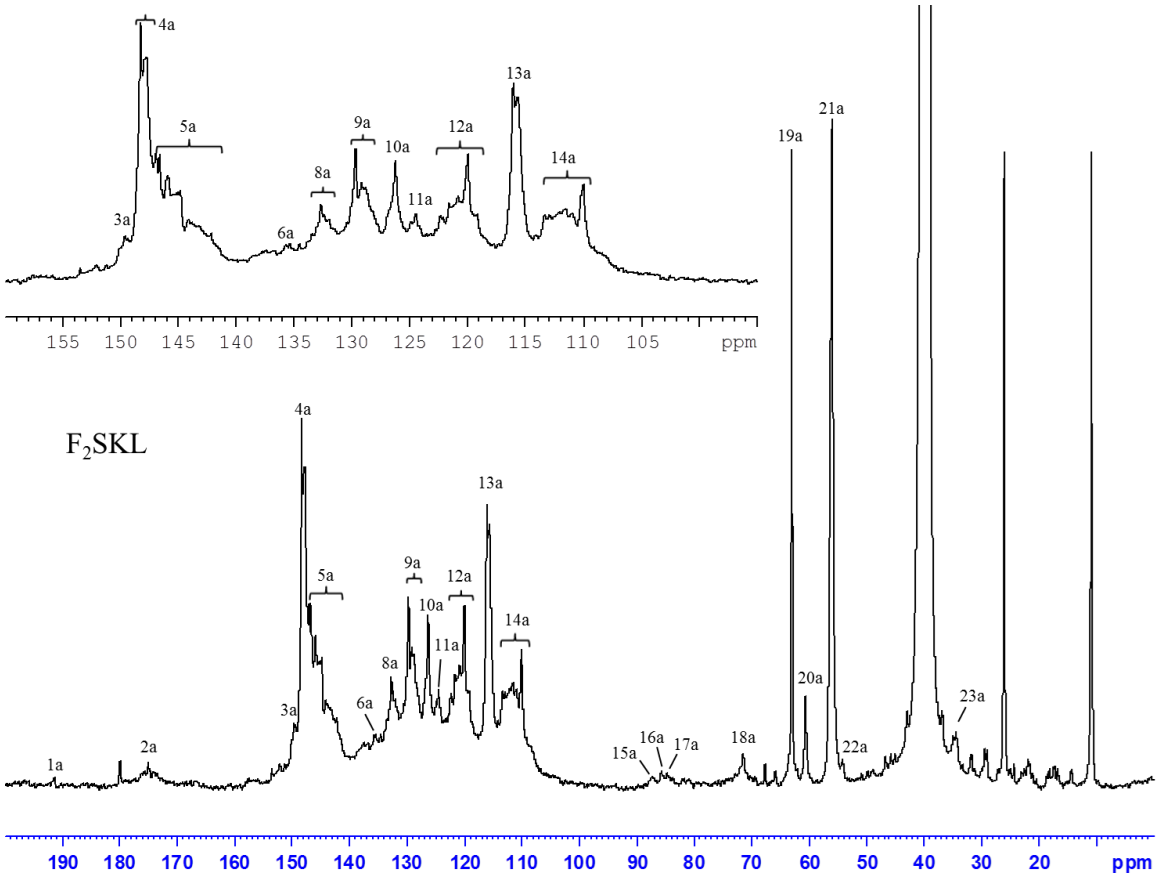
4a
5a
3a
6a
8a
9a
10a
11a
12a
13a
14a
155 150 145 140 135 130 125 120 115 110 105 ppm
F2SKL
4a
13a
5a
9a
12a
10a
14a
11a
8a
3a
6a
1a
2a
15a
16a
17a
18a
19a
21a
20a
22a
23a
190 180 170 160 150 140 130 120 110 100 90 80 70 60 50 40 30 20 ppm

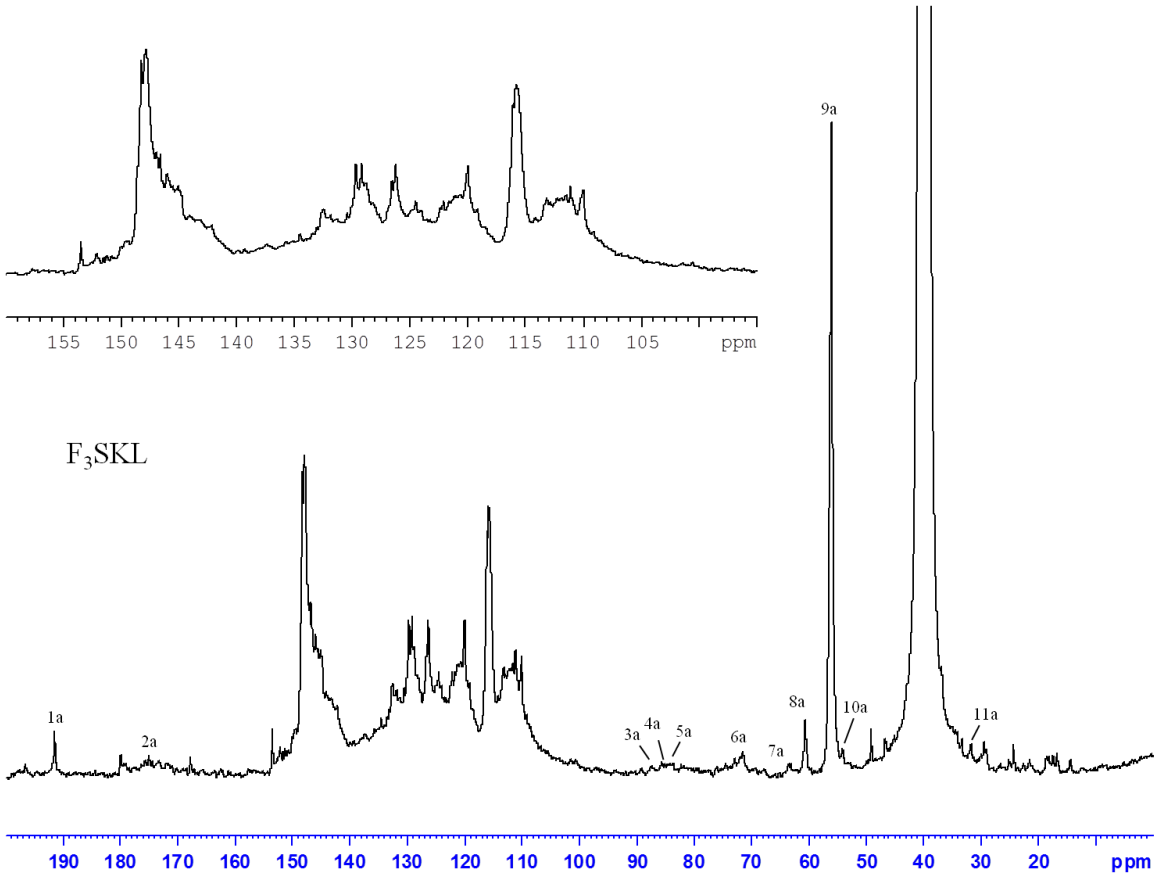
155 150 145 140 135 130 125 120 115 110 105 ppm
F3SKL
1a
2a
3a
4a
5a
6a
7a
8a
9a
10a
11a
190 180 170 160 150 140 130 120 110 100 90 80 70 60 50 40 30 20 ppm

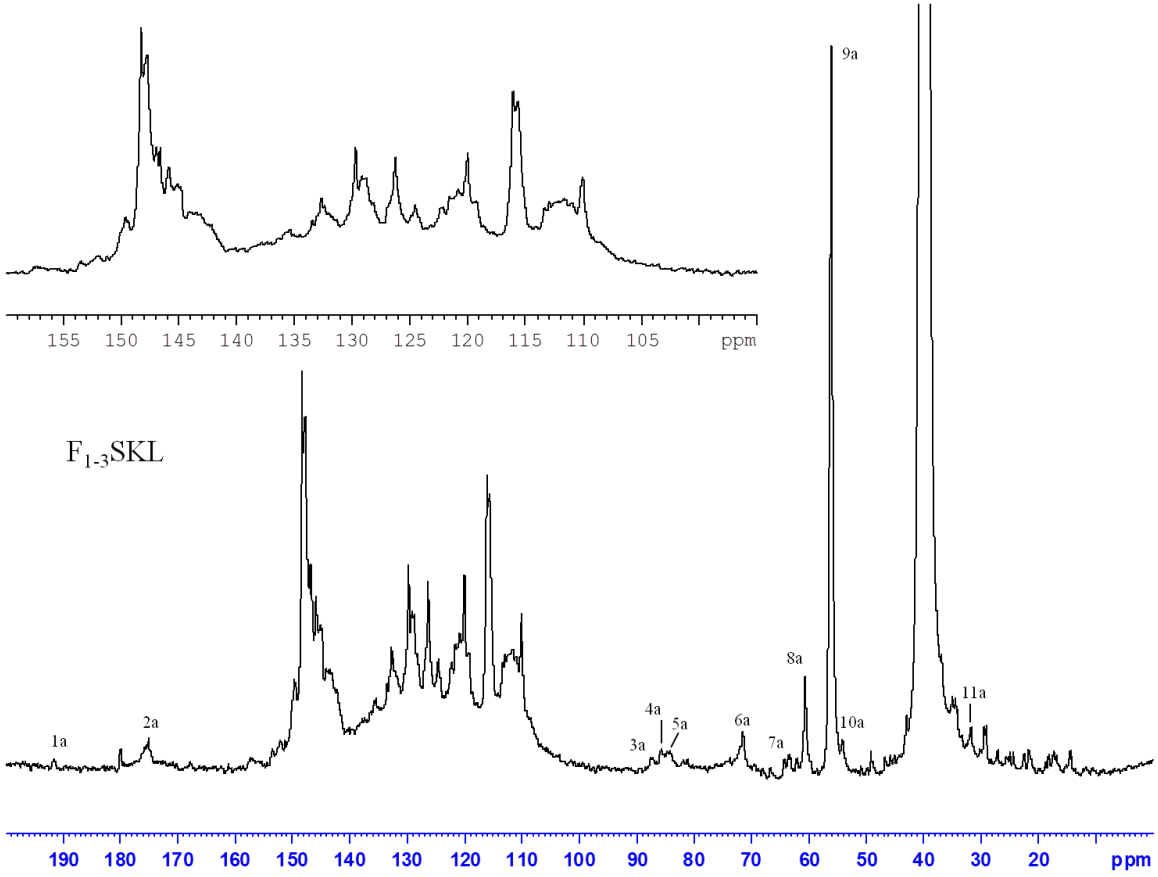
155 150 145 140 135 130 125 120 115 110 105 ppm
F1-3SKL
1a
2a
3a
4a
5a
6a
7a
8a
9a
10a
11a
190 180 170 160 150 140 130 120 110 100 90 80 70 60 50 40 30 20 ppm

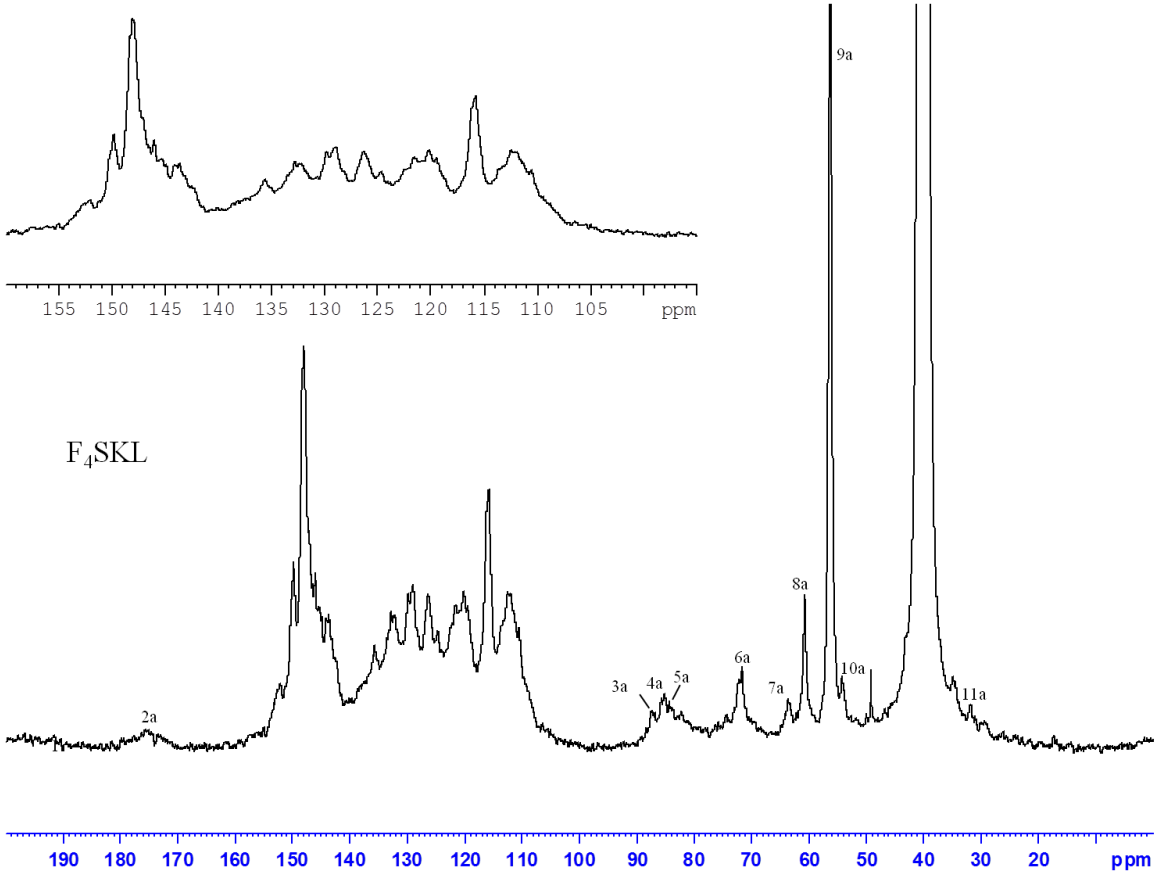
155 150 145 140 135 130 125 120 115 110 105 ppm
F4SKL
2a
3a
4a
5a
6a
7a
8a
9a
10a
11a
190 180 170 160 150 140 130 120 110 100 90 80 70 60 50 40 30 20 ppm

HSQC spectra of non-acetylated SKL, F_1SKL, F_2SKL, F_3SKL, $F_{1\text{-}3}$SKL, and F_4SKL

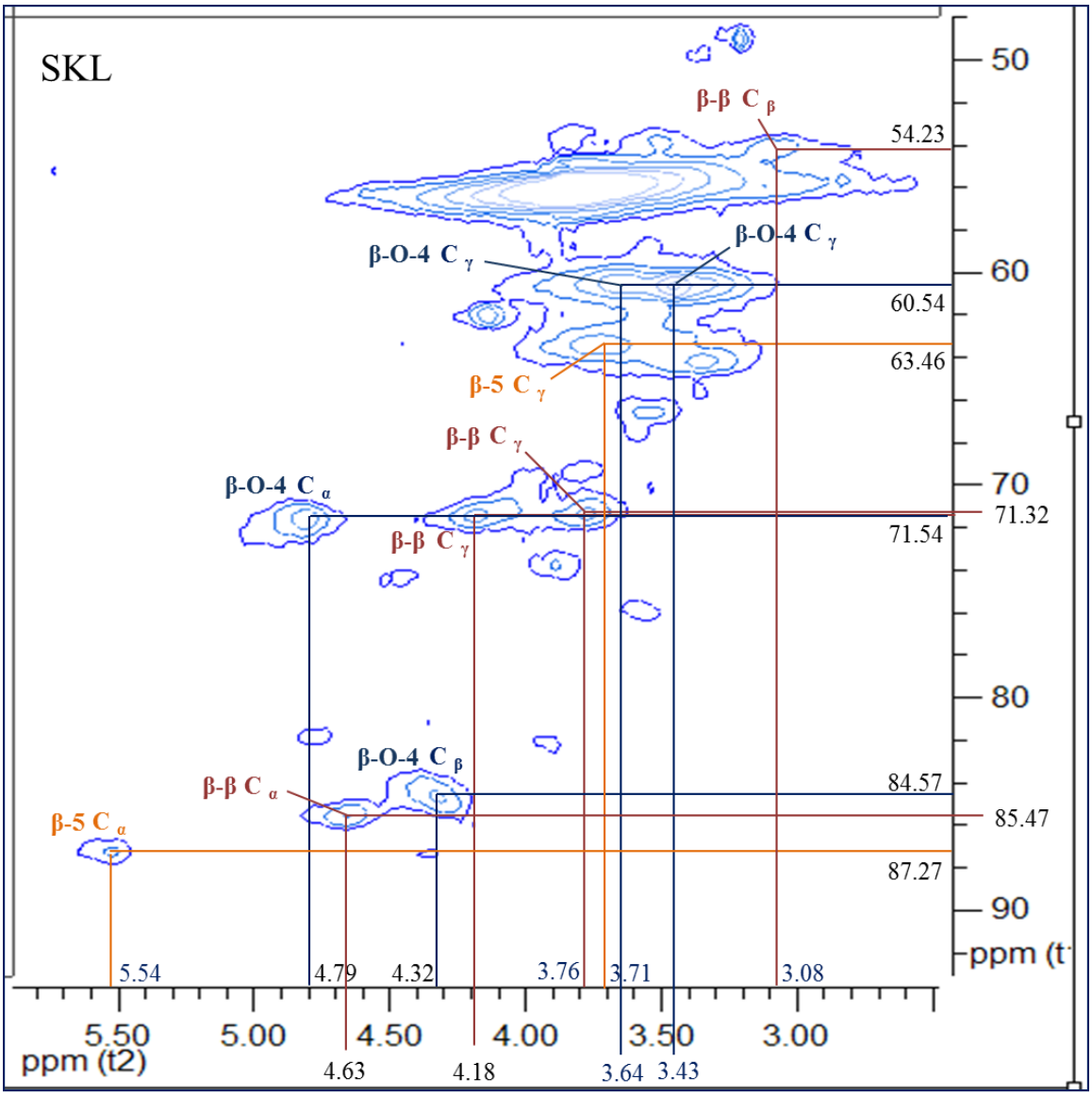

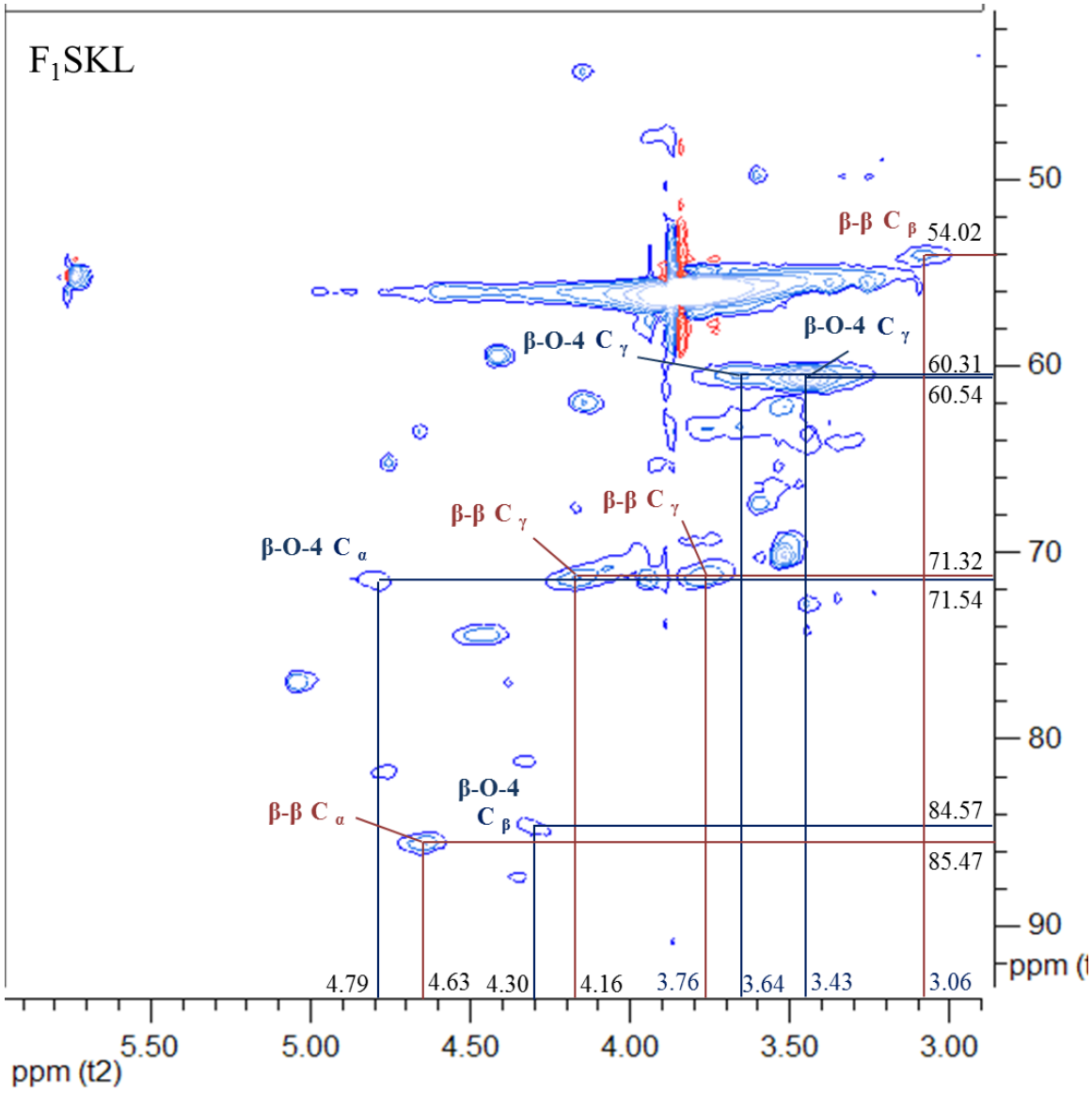
F1SKL
β-β Cβ 54.02
β-O-4 Cγ
β-O-4 Cγ
60.31
60.54
β-β Cγ
β-β Cγ
β-O-4 Cα
71.32
71.54
β-O-4
Cβ
β-β Cα
84.57
85.47
4.79
4.63
4.30
4.16
3.76
3.64
3.43
3.06
50
60
70
80
90
ppm (t
5.50
5.00
4.50
4.00
3.50
3.00
ppm (t2)

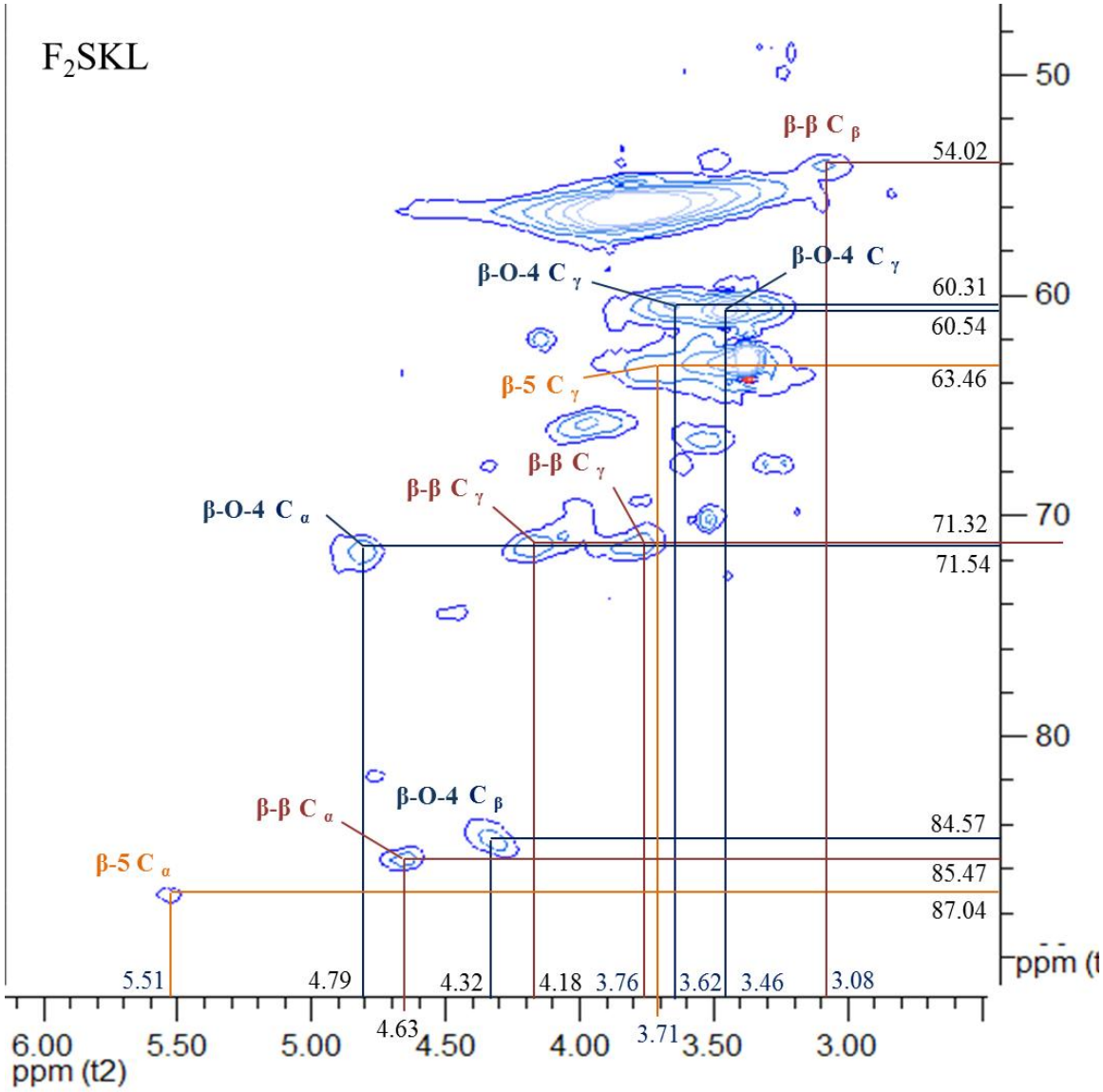
F2SKL
β-β Cβ
54.02
β-O-4 Cγ
β-O-4 Cγ
60.31
60.54
β-5 Cγ
63.46
β-β Cγ
β-β Cγ
β-O-4 Cα
71.32
71.54
β-β Cα
β-O-4 Cβ
84.57
β-5 Cα
85.47
87.04
5.51
4.79
4.32
4.18
3.76
3.62
3.46
3.08
4.63
3.71
6.00
5.50
5.00
4.50
4.00
3.50
3.00
ppm (t2)
50
60
70
80
ppm (t

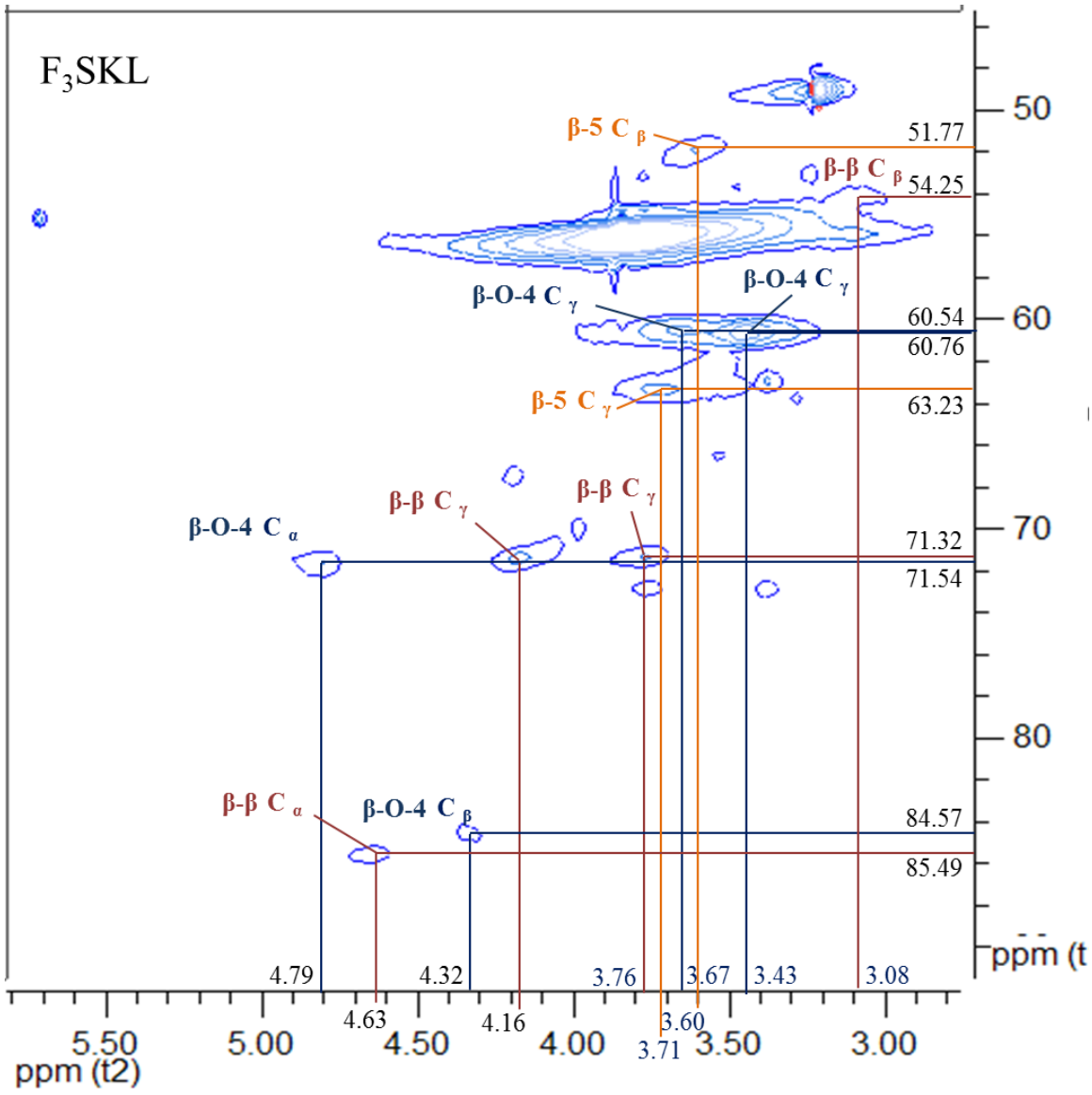
F3SKL
β-5 Cβ
β-β Cβ
β-O-4 Cγ
β-O-4 Cγ
β-5 Cγ
β-β Cγ
β-β Cγ
β-O-4 Cα
β-β Cα
β-O-4 Cβ
51.77
54.25
60.54
60.76
63.23
71.32
71.54
84.57
85.49
50
60
70
80
ppm (t
4.79
4.63
4.32
4.16
3.76
3.71
3.67
3.60
3.43
3.08
5.50
5.00
4.50
4.00
3.50
3.00
ppm (t2)

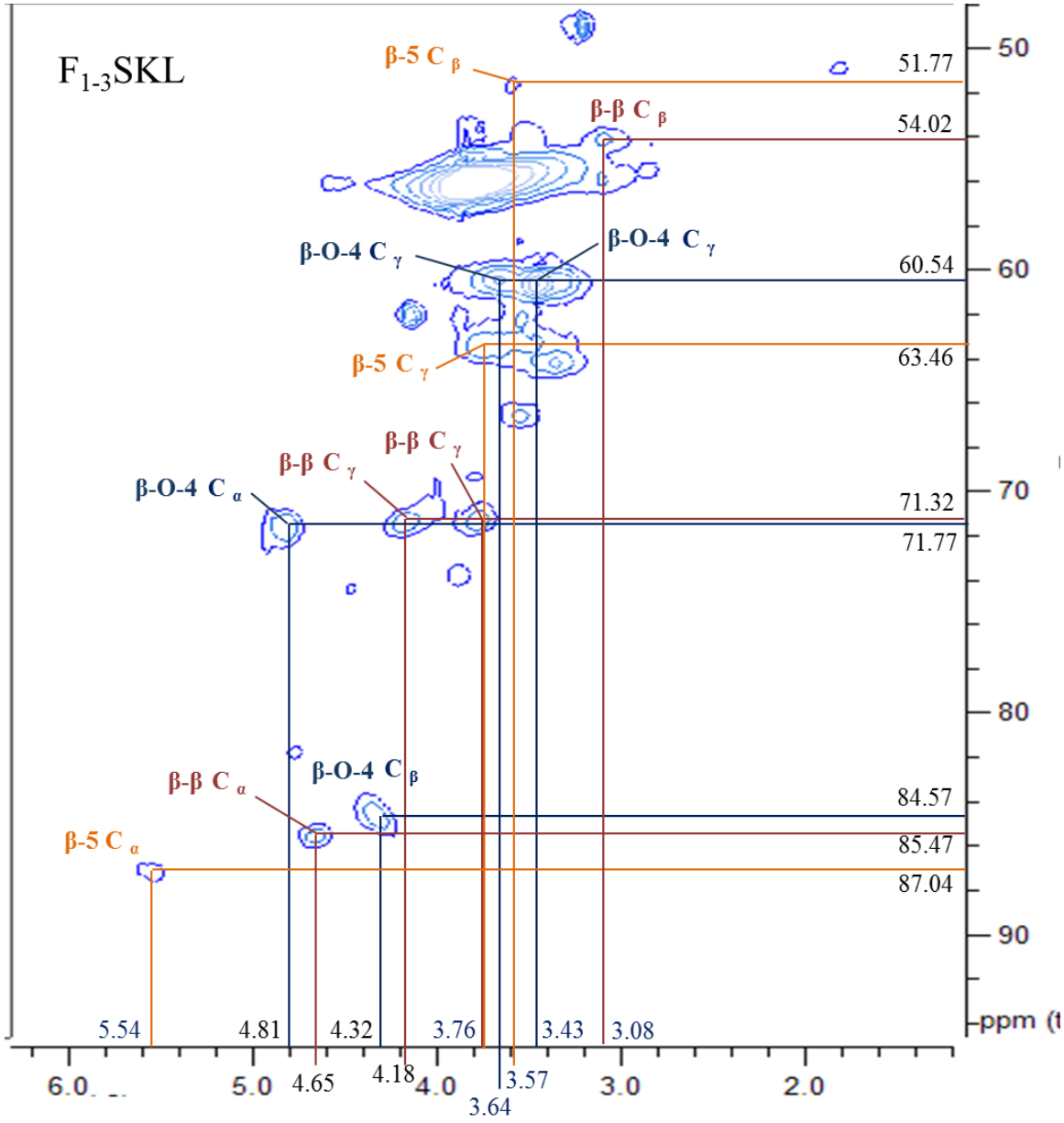
F1-3SKL
β-5 Cβ
β-β Cβ
β-O-4 Cγ
β-O-4 Cγ
β-5 Cγ
β-β Cγ
β-β Cγ
β-O-4 Cα
β-β Cα
β-O-4 Cβ
β-5 Cα
51.77
54.02
60.54
63.46
71.32
71.77
84.57
85.47
87.04
50
60
70
80
90
ppm (t
5.54
4.81
4.32
3.76
3.43
3.08
6.0
5.0
4.65
4.18
4.0
3.64
3.57
3.0
2.0

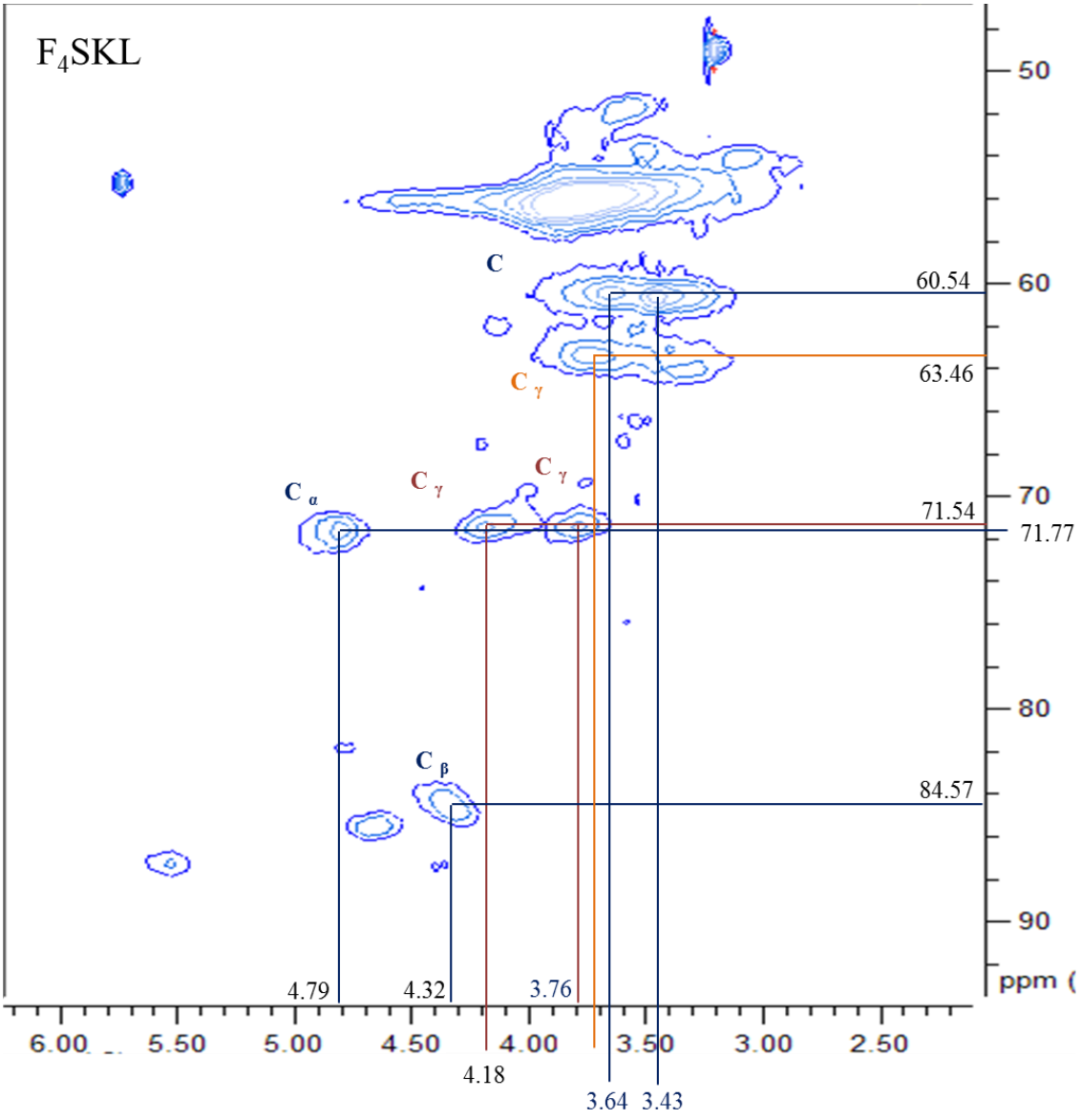
F4SKL
C
C γ
C γ
C γ
C α
C β
60.54
63.46
71.54
71.77
84.57
4.79
4.32
3.76
4.18
3.64
3.43
50
60
70
80
90
ppm
6.00
5.50
5.00
4.50
4.00
3.50
3.00
2.50

Raman spectrum of 1 mg F_4SKL sonicated with 3.1 mg MWNTs in 1 mL DMF with Gaussian peak fitting

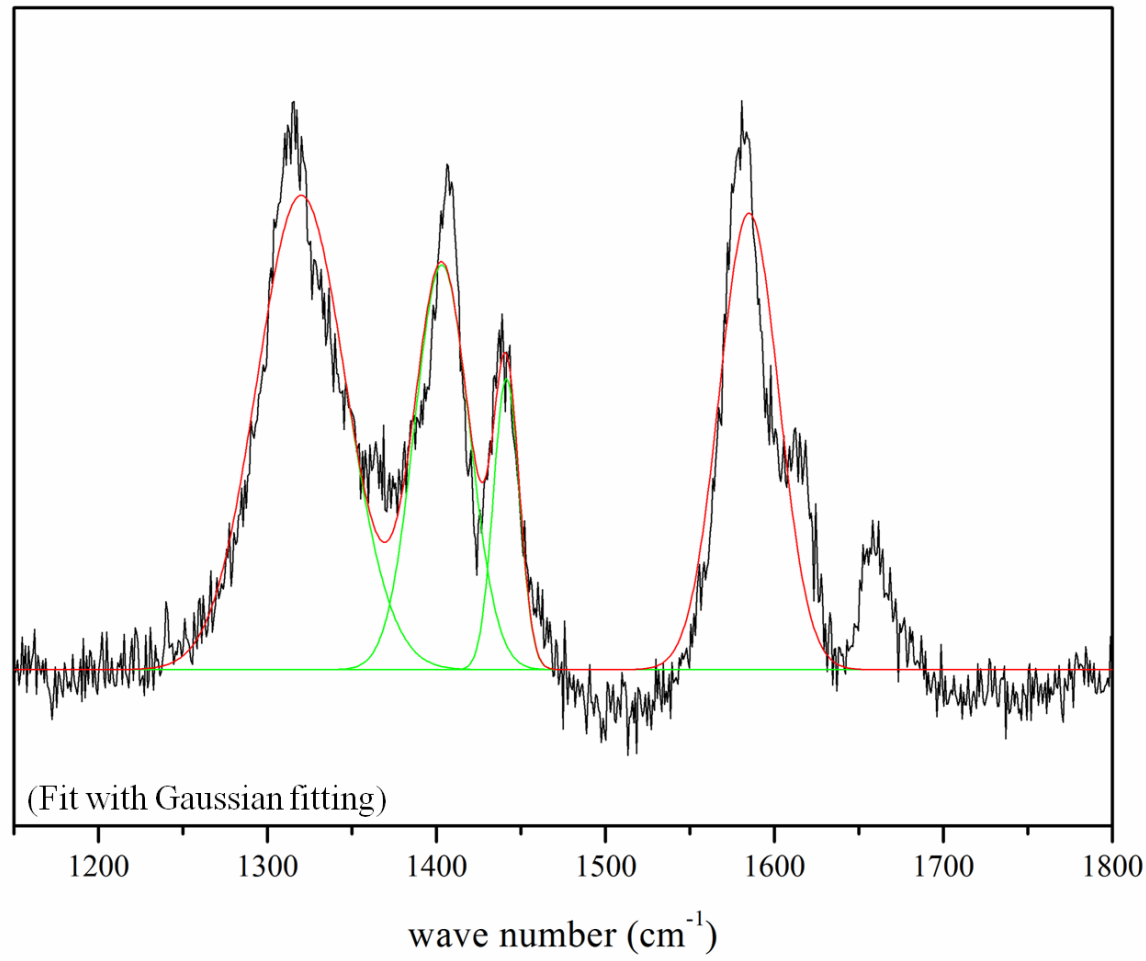

Appendix B: Equations, Tables and figures

B.1 Signal assignment in the ^{13}C-NMR of F_{1-3}SKL and F_4SKL

no.	SKL	F_1 SKL	Assignment (G = Guaiacyl)	amount (per Ar) (SKL/F_1SKL)
1a	192.3-191.0	192.3-191.0	G-CHO	0.01/0.06
2a	177.5-172.7	176.4-174.3	Aliphatic COOH	0.06/0.07
3a	87.4	-	C-α phenylcoumaran, etherified	0.05/N/A
4a	85.8	85.7	C-α pinoresinol (β-β)	0.02/0.05
5a	84.6	-	C-β (β-O-4)	0.04/N/A
6a	71.5	71.5	C-α (pinoresinol) and C-γ (β-O-4)	0.12/0.05
7a	63.6	-	C-γ phenylcoumaran (β-5)	0.05/N/A
8a	60.7	60.7	C-γ (β-O-4)	0.17/0.11
9a	56.1	56.1	-OCH_3	0.81/0.63
10a	54.1	54.2	C-β pinoresinol (β-β)	0.09/0.05
11a	31.7	31.8	C-α dihydroconiferyl alcohol	0.06/0.12
		Clusters		
	162-142	C_{Ar-O}	1.84/1.80	
	142-125	C_{Ar-C}	1.81/1.75	
	125-102	C_{Ar-H}	2.34/2.28	
	90-58	Alk-O	0.95/1.37	
	90-77	Alk-O-Ar, α-O-Alk	0.30/0.51	
	77-65	γ-O-Alk, OH_{sec}	0.34/0.54	
	65-58	OH_{prim}	0.31/0.34	

no.	F_2 SKL	F_3 SKL	Assignment (G = Guaiacyl)	amount (per Ar) (F_2 SKL /F_3SKL)
1a	192.3-191.0	192.3-190.3	G-CHO	0.06/0.10
2a	177.1-172.7	176.2-174.7	Aliphatic COOH	0.21/0.07
3a	87.4	87.5	C-α phenylcoumaran, etherified	0.09/0.08
4a	85.7	85.7	C-α pinoresinol (β-β)	0.06/0.07
5a	84.8	84.7	C-β (β-O-4)	0.06/0.05
6a	71.5	71.5	C-α (pinoresinol) and C-γ (β-O-4)	0.11/0.12
7a	63.0	63.2	C-γ phenylcoumaran (β-5)	0.29/0.04
8a	60.7	60.7	C-γ (β-O-4)	0.14/0.13
9a	56.1	56.1	-OCH_3	0.55/0.56
10a	54.2	54.1	C-β pinoresinol (β-β)	0.07/0.06
11a	31.7	31.8	C-α dihydroconiferyl alcohol	0.11/0.09
		Clusters		
	162-142	C_{Ar-O}	1.76/1.70	
	142-125	C_{Ar-C}	1.69/1.62	
	125-102	C_{Ar-H}	2.36/2.41	
	90-58	Alk-O	1.56/1.50	
	90-77	Alk-O-Ar, α-O-Alk	0.54/0.62	
	77-65	γ-O-Alk, OH_{sec}	0.53/0.56	
	65-58	OH_{prim}	0.49/0.33	

no.	F_{1-3}SKL	F_4SKL	Assignment (G = Guaiacyl)	amount (per Ar) (F_{1-3}SKL/F_4SKL)
1a	192.30-190.94	N/A	G-CHO	0.00/ N/A
2a	177.51-172.70	177.45-172.79	Aliphatic COOH	0.02/0.04
3a	87.61	87.38	C-α phenylcoumaran, etherified	0.01/0.02
4a	86.86-84.90	86.50-84.71	C-α pinoresinol (β-β)	0.02/0.02
5a	84.71	84.34	C-β (β-O-4)	0.01/0/01
6a	71.51	71.67	C-α (pinoresinol) and C-γ (β-O-4)	0.03/0.03
7a	63.15	63.69	C-γ phenylcoumaran (β-5)	0.01/0.02
8a	60.73	60.76	C-γ (β-O-4)	0.03/0.04
9a	56.10	56.28	-OCH_3	0.12/0.10
10a	54.14	54.21	C-β pinoresinol (β-β)	0.01/0.02
11a	31.751	31.73	C-α dihydroconiferyl alcohol	0.02/0.02
		Clusters		
	162-142	C_{Ar-O}	1.67/1.86	
	142-125	C_{Ar-C}	1.69/1.67	
	125-102	C_{Ar-H}	2.33/2.23	
	90-58	Alk-O	1.44/1.96	
	90-77	Alk-O-Ar, α-O-Alk	0.58/0.76	
	77-65	γ-O-Alk, OH_{sec}	0.53/0.72	
	65-58	OH_{prim}	0.33/0.49	

B.2 Equations

The region between 95-160 ppm is defined as aromatic region. Peak assignments of acetylated SKL fractions are based on the study aforementioned (*153*). All integrals of peaks and amount of β-O-4 linkage are presented by amount per aromatic ring (Ar) and calculated based on elsewhere (*8*).

structure	calculation	value (per Ar; $AceF_{1\text{-}3}SKL/AceF_4SKL$)
phenylcoumaran	$I_{88\text{-}86}$	0.01/0.02
β-1	$I_{51\text{-}48}$- $I_{88\text{-}86}$	0.09/0.09
α-OH/β-O-4	$I_{77\text{-}72.5}$- $I_{51\text{-}48}$- $I_{88\text{-}86}$	0.068/0.006

B.3 Strength (MPa) of fabrics with varied MWNTs concentrations and at different heat process (n=20)

	As-spun	Thermostabilized	Carbonized
0wt%	5.13 ± 0.64^{a}	23.86 ± 2.55^{a}	45.03 ± 9.93^{a}
1wt% (1 mg F_4SKL)	4.16 ± 0.78^{b}	23.34 ± 3.46^{a}	36.85 ± 10.31^{ab}
4wt% (1 mg F_4SKL)	4.27 ± 0.95^{b}	23.18 ± 4.16^{a}	28.61 ± 6.52^{c}
4wt% (100 mg F_4SKL)	2.46 ± 0.49^{c}	21.46 ± 2.82^{ab}	28.15 ± 7.45^{c}
6wt% (100 mg F_4SKL)	3.98 ± 0.81^{b}	19.40 ± 3.60^{b}	34.25 ± 8.83^{bc}

B.4 Moduli (MPa) of fibres with varied MWNTs concentrations and at different heat process (n=20)

	As-spun	Thermostabilized	Carbonized
0wt%	514.63 ± 70.93^{bc}	918.05 ± 132.31^{c}	6238.35 ± 1307.74^{a}
1wt% (1 mg F_4SKL)	566.25 ± 69.51^{ab}	1113.68 ± 118.88^{a}	4648.21 ± 755.17^{b}
4wt% (1 mg F_4SKL)	663.73 ± 157.89^{a}	1070.43 ± 179.09^{ab}	2394.29 ± 270.20^{e}
4wt% (100 mg F_4SKL)	504.33 ± 98.79^{bc}	1078.27 ± 117.89^{ab}	2416.90 ± 796.75^{d}
6wt% (100 mg F_4SKL)	393.12 ± 132.77^{c}	1066.47 ± 127.11^{b}	3105.93 ± 467.89^{c}

B.5 Elongation (%) of fibres with varied MWNTs concentrations and at different heat process (n=20)

	As-spun	Thermostabilized	Carbonized
0wt%	1.73 ± 0.45^{a}	3.12 ± 0.61^{a}	0.76 ± 0.17^{b}
1wt% (1 mg F_4SKL)	1.21 ± 0.33^{b}	2.21 ± 0.41^{b}	0.97 ± 0.21^{b}
4wt% (1 mg F_4SKL)	1.05 ± 0.39^{b}	2.08 ± 0.54^{b}	1.42 ± 0.17^{a}
4wt% (100 mg F_4SKL)	1.07 ± 0.44^{b}	2.24 ± 0.37^{b}	1.38 ± 0.27^{a}
6wt% (100 mg F_4SKL)	1.44 ± 0.37^{a}	2.16 ± 0.41^{b}	1.33 ± 0.20^{a}

B.6 Toughness (kJ/m^3) of fibres with varied MWNTs concentrations and at each heat process (n=20)

	As-spun	Thermostabilized	Carbonized
0wt%	38.55 ± 9.86^{a}	436.59 ± 99.04^{a}	136.38 ± 65.15^{a}
1wt% (1 mg F_4SKL)	25.26 ± 12.05^{c}	251.77 ± 78.75^{b}	141.15 ± 61.51^{a}
4wt% (1 mg F_4SKL)	22.81 ± 9.92^{bc}	251.02 ± 73.06^{b}	156.76 ± 55.26^{a}
4wt% (100 mg F_4SKL)	16.78 ± 8.40^{c}	229.12 ± 71.47^{bc}	153.66 ± 61.99^{a}
6wt% (100 mg F_4SKL)	26.92 ± 10.33^{b}	181.68 ± 63.23^{c}	177.17 ± 64.32^{a}

B.7 Stress-stain curves of as-spun, thermostabilized, and carbonized fibres